Degradation Study of SOC Stacks with Impedance Spectroscopy

Yulin Yan

JÜLICH
Forschungszentrum

Mitglied der Helmholtz-Gemeinschaft

Schriften des Forschungszentrums Jülich
Reihe Energie & Umwelt / Energy & Environment   Band / Volume 441

Degradation Study of SOC Stacks with Impedance Spectroscopy

Yulin Yan

Abstract

The Solid Oxide Fuel Cell (SOFC) is a high temperature fuel cell operated at 600 °C ~ 900 °C. The SOC stack can switch between fuel cell mode (SOFC) and electrolysis mode (SOEC). The performance degradation mechanisms are different under these two modes. The Electrochemical Impedance Spectroscopy (EIS) is an in-situ characterization method and its resolution can be improved by the DRT (Distribution of Relaxation Times) technique.

The aim of this thesis is the investigation of SOC stack characterization in large test rigs with EIS and DRT. The EIS and DRT analysis can be influenced by 1) the inductance, 2) electrical noises and 3) noisy signal from the test rig. The test rig inductance and the electrical noises can affect the EIS data quality at high frequencies, while the influence of noisy signals is at low frequencies. The inductance error can be corrected by subtracting the test rig inductance from the stack impedance. The electrical noises can be excluded by physically cutting the built-in electric load and power supply off from the EIS circuit. By data processing with the HIT (Hilbert transform) correction, the noisy signal at low frequencies can be removed.

The DRT peaks identification was performed with an SOC stack through the parameter study. Up to five DRT peaks can be identified and related to corresponding electrode processes according to the experimental results and previous results obtained with single cells by KIT (Karlsruhe Institute of Technology).

A four-cell stack was assembled with JÜLICH's F10 design. The durability of the stack was investigated by a long-term stationary electrolysis operation with a constant current density of -0.5 Acm^{-2} at 800 °C. EIS and DRT were used to study the performance of the stack. The results helped give prediction to the degradation mechanisms of each cell during operation, which was supported by the post-mortem analysis results.

Kurzfassung

Die Festoxid-Brennstoffzelle (SOFC) ist eine Hochtemperatur-Brennstoffzelle, die bei 600 bis 900 °C betrieben wird. Der SOC-Stack kann zwischen dem Brennstoffzellenmodus (SOFC) und dem Elektrolysemodus (SOEC) wechseln. Die Leistungsminderungsmechanismen unterscheiden sich in diesen beiden Modi. Die Elektrochemische Impedanzspektroskopie (EIS) ist eine in-situ Charakterisierungsmethode, wobei die Aussagekraft der EIS durch die DRT-Technik (Distribution of Relaxation Times) verbessert werden kann.

Ziel dieser Arbeit ist die Anwendung von EIS und DRT zur Charakterisierung von SOC-Stacks, die in Testständen betrieben werden. Die EIS- und DRT-Analyse kann beeinflusst werden durch 1) die Induktivität, 2) elektrische Störungen und 3) verrauschte Signale vom Prüfstand. Die Prüfstandsinduktivität und die elektrischen Störungen können die EIS-Datenqualität bei hohen Frequenzen beeinflussen, während der Einfluss von Störsignalen bei niedrigen Frequenzen liegt. Der durch Induktivitäten verursachte Fehler kann korrigiert werden, indem die Prüfstandsinduktivität von der Stackimpedanz abgezogen wird. Die elektrischen Störungen können beseitigt werden, indem die eingebaute elektrische Last und die Stromversorgung vom EIS-Stromkreis getrennt werden. Durch die Datenverarbeitung mit der HIT-Korrektur (Hilbert-Transformation) kann das Rauschsignal bei niedrigen Frequenzen eliminiert werden.

Die Identifizierung der DRT-Peaks wurde mit einem SOC-Stack mittels einer Parameterstudie durchgeführt. Es können bis zu fünf DRT-Peaks identifiziert werden, die mit Hilfe der Ergebnisse der durchgeführten Experimente und früherer Analysen an Einzelzellen, die vom KIT (Karlsruher Institut für Technologie) durchgeführt wurden, mit entsprechenden Elektrodenprozessen in Beziehung gesetzt werden.

Ein Vier-Zellen-Stack wurde entsprechend dem JÜLICH F10-Design aufgebaut. Die Haltbarkeit des Stapels wurde durch einen stationären Langzeittest im Elektrolysemodus bei einer konstanten Stromdichte von -0,5 Acm^{-2} bei 800 °C untersucht. EIS und DRT wurden verwendet, um die Leistung des Stacks zu analysieren. Hiermit konnten die Alterungsmechanismen jeder Zelle während des Betriebs identifiziert werden, was durch die Ergebnisse der Post-Mortem-Analyse bestätigt wurde.

List of Abbreviations

ADIS	Analysis of Differences in Impedance Spectra
AFC	Alkaline Fuel Cell
AFL	Anode Function Layer
ASC	Anode-Supported Cell
ASR	Area Specific Resistance
BSD	Backscattered Electron Detector
CNLS	Complex Nonlinear Least Squares
CPE	Constant Phase Element
CTE	Coefficient of Thermal Expansion
DRT	Distribution of Relaxation Times
ECM	Equivalent Circuit Model
EDX	Energy Dispersive X-ray Spectroscopy
EIS	Electrochemical Impedance Spectroscopy
GDC	Gadolinium-doped Ceria
HIT	Hilbert Transform
IT-SOFC	Intermediate Temperature-Solid Oxide Fuel Cell
IV-Curve	Current Voltage-Curve
LCC10	$La_{1-x}Ca_xCrO_3$
LSC	$La_{0.6}Sr_{0.4}CoO_{3-\delta}$
LSCF	$La_{0.6}Sr_{0.4}Co_{0.2}Fe_{0.8}O_{3-\delta}$
LSF	$La_{0.8}Sr_{0.2}FeO_{3-\delta}$
LSM	$(La,Sr)MnO_3$
MCF	$MnCo_{1.9}Fe_{0.1}O_4$
MCFC	Molten Carbonate Fuel Cell
MIEC	Mixed Ionic and Electronic Conductor
OCV	Open Circuit Voltage
ORR	Oxygen Reduction Reaction
PAFC	Phosphoric Acid Fuel Cell
PEMFC	Polymer Electrolyte Membrane Fuel Cell

PVD	Physical Vapor Deposition
ScSZ	Sc_2O_3 stabilized zirconia
SDC	Samarium doped Ceria
SEM	Scanning Electron Microscopy
SOC	Solid Oxide Cell
SOEC	Solid Oxide Electrolyzer Cell
SOFC	Solid Oxide Fuel Cell
TPB	Triple Phase Boundary
WPS	Wet Powder Spraying
YSZ	Yttria-stabilized Zirconia

Contents

1. Introduction

The relationship between the combustion of fossil fuels and the climate issues has been widely discussed in recent years. The investigation of renewable energy such as solar energy, wind energy, etc. has attracted much interest. Among them, hydrogen energy is considered to have the potential to be the next generation environmentally-friendly fuel [1]. Meanwhile, the rapidly increased demand of renewable energy has stimulated the investigation on the conversion between renewable energy and electric energy. Fuel cell is a kind of energy conversion device which converts chemical energy directly into electric power. Compared with traditional combustion engine, the efficiency of fuel cell is not limited by the Carnot cycle, thus it could reach higher energy conversion efficiency.

According to the working temperature, the fuel cell could be divided into 1) low temperature fuel cell (60 °C ~ 120 °C): Alkaline Fuel Cell (AFC) and Polymer Electrolyte Membrane Fuel Cell (PEMFC); 2) mean temperature fuel cell (~ 200 °C): Phosphoric Acid Fuel Cell (PAFC); and 3) high temperature fuel cell (> 650 °C): Molten Carbonate Fuel Cell (MCFC) and Solid Oxide Fuel Cell (SOFC). The SOFC shows advantages in many aspects such as fuel flexibility (H_2, CO, CH_4…), high plan efficiency (70% with combined cycle) and good reversibility (simply switch between fuel cell mode and electrolysis mode). Therefore, SOFC has become the most promising choice for the power unit especially in the stationary power plant.

Although the application of renewable energy such as solar and wind power has already been commercialized, the integration of them into the electric grid still faces problems. Due to the unpredictable nature of the primary source of power (sun, wind…), the power generation of the wind/solar power plant is unstable. In order to maintain the stability of the grid, a lot of the generated power is "wasted" because of the unbalance between power generation and demand. The investigation of utilizing the "wasted" energy has become an issue in recent years.

One way is to convert the electric power into chemical energy for storage. Hydrogen is one good choice because of the high energy density, no greenhouse gases emission

and abundant resources. Water electrolysis is one of the most common methods for producing it [2]. The idea of combining electrolyzers with energy systems, e.g., fuel cells, is considered particularly promising [3]. Currently, low temperature alkaline and proton exchange membrane (PEM) electrolyzers are the most advanced technologies in this area [4]. Recently, however, high temperature electrolysis using Solid Oxide Electrolysis Cells (SOECs) with a reversible SOFC has shown particular promise. Due to its high working temperature, the SOEC system allows: (i) a high reaction rate; (ii) no need for an expensive catalyst (i.e., made from platinum); (iii) high electrical efficiency [5].

However, high working temperatures would impact the material stability, which will further result in the performance degradation of the SOC stacks. In order to achieve the lifetime required by the commercialization of SOC technology [6], the degradation behavior of SOC stacks needs further investigation. Although different degradation mechanisms have been reported for SOC cells in recent years [7-14], literatures related to the degradation study of SOEC stacks are still quite limited.

The electrochemical performance and degradation of SOC stacks can be characterized by DC and AC techniques. One of the most commonly used DC techniques is the IV-curve (Current-Voltage curve) measurement. Through IV-curve measurements, the total polarization could be obtained. However, it is not possible to distinguish the contribution of individual stack components. Electrochemical impedance spectroscopy (EIS) is a powerful AC technique, which has been widely applied to the investigation of degradation mechanisms of SOCs [5, 8, 9, 15]. A general EIS analysis procedure includes a Complex Nonlinear Least Squares (CNLS) fitting algorithm, with which the frequency dispersion data of electrochemical systems can be analyzed in terms of an equivalent circuit model (ECM) [16]. One disadvantage of this approach is the severe ambiguity inherent to the adopted ECM, since the same impedance spectrum can be mathematically (but not physically) fitted using many different models. One way to overcome this limitation is to first calculate and analyze the distribution function of relaxation times (DRT) of the impedance response, through which the electrochemical processes with different characterization times can be separated. However, due to the difficulties in performing EIS measurements with SOC stacks in large-scale test rigs (e.g. high inductance and noisy signals), the data quality of the obtained EIS results is

4

relatively poor. The reliability of the DRT results is very sensitive to the EIS data quality, which has limited the application of DRT to the study of SOC stack, but mostly still in cell level [17-19].

Goal of this work:

The major goal of this thesis is to investigate the application of EIS and DRT technique as in-situ diagnoses method to the degradation study of SOC stacks. Since the SOC stack can operate under SOFC and SOEC modes, a comprehensive understanding of the degradation mechanisms of the SOC stack under both modes is required.

Considering the difficulties and uncertainties of the EIS measurement with real SOC stacks (e.g. influence from the inductance and noisy signals), the optimization of the impedance set-up, as well as the EIS data post-processing methods were throughout the complete study.

Furthermore, based on the results about identifying the physical meaning of the DRT peaks conducted with single cells by other groups [18, 20], the DRT peak identification should be extended to SOC stacks before applying DRT to the SOC stack degradation study.

The deduced degradation phenomena and mechanisms with the help of EIS/DRT technique during the stack operation will be further proven and confirmed by post-mortem analysis.

Outline:

In **Chapter 2**, a general introduction about the SOC stacks will be given, including a brief review of the individual stack components. The degradation mechanisms of SOC stacks operated under SOFC and SOEC mode will be presented. Moreover, the theoretical background of the EIS and DRT technique is given and the difficulties in performing EIS measurements with SOC stacks are also discussed in this chapter.

In the **Experiment Chapter**, the SOC stack construction and the test rigs used for this work will be described. The EIS set up as well as the DRT calculation approach is also presented in this chapter.

In **Chapter 4**, the major experimental results and related discussions are concluded. In the first part, methods to improve the EIS data quality as well as the reliability of the calculated DRT results are discussed, including the EIS set-up optimization and the results of EIS data post-processing. In the second part, based on the previous results from KIT (Karlsruhe Institute of Technology) about the DRT peak identification with single cells, the DRT peak identification experiment is extended to SOC stacks through a parameter study. In the third part, the reliability and feasibility of EIS&DRT as a diagnosis technology with SOC stacks is proved during real stack tests.

In **Chapter 5**, a brief summary of the findings during the PhD work is given.

2. Fundamentals and literature overview

2.1 SOFC and SOEC

2.1.1 Working principle

The SOFC is an electrochemical device which could convert chemical energy into electric energy at high working temperatures (600 °C ~ 900 °C). The SOFC has a "Sandwich" structure with all-solid-state cell components. The electrodes of the cell are supplied separately with fuel gas and oxidant gas. The electrodes are separated by the electrolyte, avoiding the direct combustion of fuel gas. The electrolyte can be either proton conducting or oxygen-ion conducting. Since all stacks tested during this study have the oxygen-ion conducting electrolyte, the proton conducting electrolyte will not be discussed in this thesis. As **Figure 2.1(a)** shows, with the oxygen-ion conducting electrolyte, the following half reactions would take place in respective electrodes:

Air electrode: $\frac{1}{2}O_2 + 2e^- = O^{2-}$;

Fuel electrode: $H_2 + O^{2-} = H_2O + 2e^-$;

Overall reaction: $\frac{1}{2}O_2 + H_2 = H_2O$
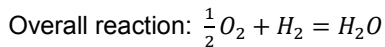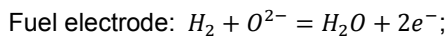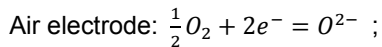
For cells with oxygen-ion conducting electrolyte, the oxygen is reduced into oxygen ion (O^{2-}) under the catalysis effect of air electrode material. Due to the higher oxygen partial pressure at the air electrode side, the O^{2-} ions will transport through the electrolyte and reach the fuel electrode, once the external circuit is closed. At the fuel electrode, O^{2-} will react with the fuel gas forming water and releasing electrons to the external circuit.
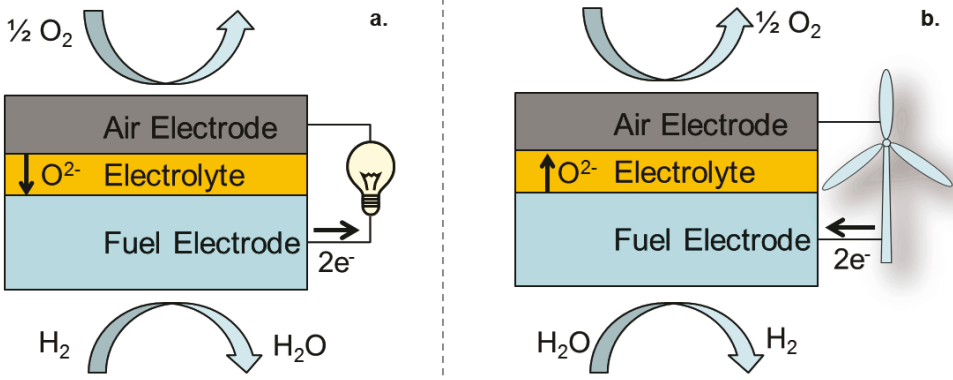
Figure 2.1: Working principles of (a) SOFC and (b) SOEC.

Figure 2.1(b) shows the working principle of an SOEC, which could be regarded as the reverse process of SOFC. During SOEC operation, the fuel electrode is supplied with steam and produces hydrogen. O^{2-} will transport through the electrolyte and be oxidized into O_2 at the air electrode. The reactions in electrodes are as follows:

Air electrode: $O^{2-} = \frac{1}{2}O_2 + 2e^-$;

Fuel electrode: $H_2O + 2e^- = H_2 + O^{2-}$;

Overall reaction: $H_2O = H_2 + \frac{1}{2}O_2$
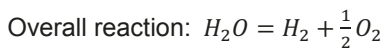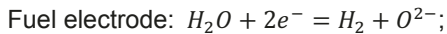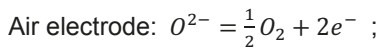
2.1.2 Thermodynamics

Essentially, SOCs are concentration cells in which the transform between electric energy and thermal energy obeys the basic thermodynamic equation:

$$\Delta H = \Delta G + T\Delta S$$

For an SOFC, the Gibbs energy difference ΔG is the maximum electric energy the system can deliver. When the SOFC is in the currentless equilibrium status (I= 0 A) at standard condition, the theoretical cell voltage can be calculated according to the following equation:

$$U_{th} = E^0 = -\frac{\Delta G_0}{zF}$$

E^0 is the electromotive force (also called reversible electrochemical voltage) of the cell; F is the Faraday constant and z is the number of moles of electrons transferred in the reaction.

In the real situation, the cell voltage varies with operation conditions (e.g. temperature, gas pressure and concentration). The cell voltage at current-less condition can be determined based on the Nernst equation:

$$U_N(T) = -\frac{\Delta G_0(T)}{zF} - \frac{R \times T}{z \times F} \times \sum ln \frac{p_i^{v_i - products}}{p_i^{v_i - educts}}$$

R is the gas constant (8.3144 Jmol^{-1}K^{-1}); T is the Kelvin degree, p_i is the partial pressure of reactants and v_i is the number of moles of reactants.

For cells using hydrogen (fuel cell mode) or steam (electrolysis mode) as fed gas, the Nernst equations are as follows:

SOFC: $U_N(T) = -\frac{\Delta G_0(T)}{2F} - \frac{R \times T}{2F} \times ln \frac{p_{H_2O}}{(p_{O_2})^{0.5} \times p_{H_2}}$

SOEC: $U_N(T) = \frac{\Delta G_0(T)}{2F} + \frac{R \times T}{2F} \times ln \frac{p_{H_2O}(p_{O_2})^{0.5} \times p_{H_2}}{p_{H_2O}}$

2.1.3 Polarization behavior

The Nernst voltage can only be reached when no current flows through the circuit. The cell voltage will decrease when current is delivered (SOFC) or increased when current is applied (SOEC). The deviation between the real cell voltage and the Nernst voltage is due to the polarization loss of the fuel cell. **Figure 2.2** shows the typical polarization curves of PEFC and SOFC.
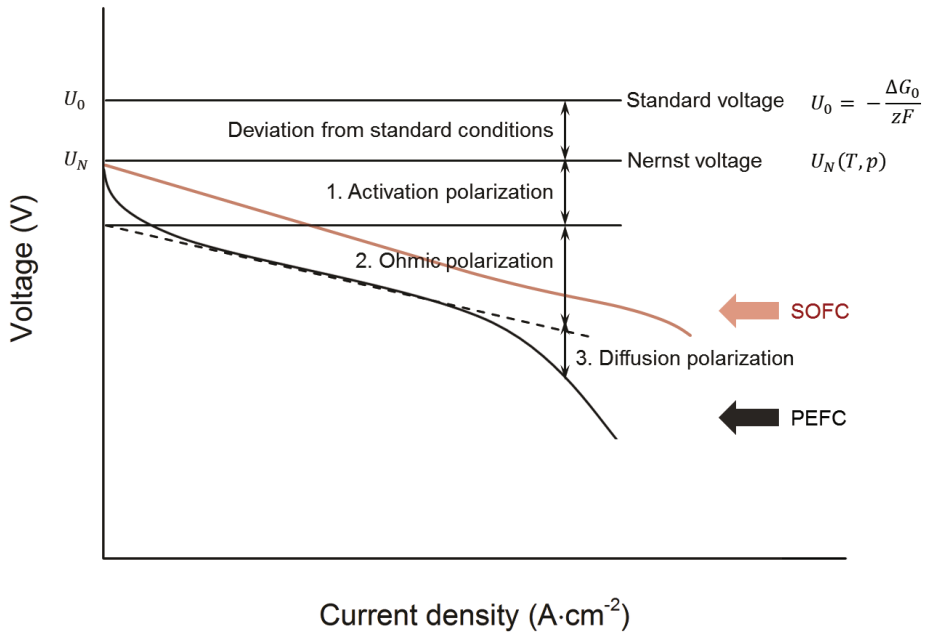
Figure 2.2: Polarization curves of fuel cells

The polarization curve records the cell voltage (U/V) versus current density (j/Acm^{-2}). For the polarization curve of PEFC, three zones could be identified in **Figure 2.2**. The initial non-linear curve appeared at low current density is the activation polarization η_{act}. This describes the activation energy required to overcome the energy barrier so that electrochemical reactions can take place. For each single electrode, the influence of

activation overpotential on current density can be described with the Butler-Volmer equation:

$$j = j_0 \cdot \left[exp\left(\frac{\alpha_a zF\eta}{RT}\right) - exp\left(-\frac{\alpha_c zF\eta}{RT}\right) \right]$$

In which j_0 is the electrode exchange current density; α_a is the anodic charge transfer coefficient; α_c is the cathodic charge transfer coefficient; z is the number of electrons involved in the electrode reaction; η is the activation overpotential.

The polarization curve appears linear at medium current density after the activation zone. The linear potential drop in this zone obeys Ohm's law, so that the polarization in the zone is also called the ohmic polarization (η_{ohm}). The ohmic polarization is the result of electronic and ionic transport in the electrodes and the electrolyte, and it could be expressed as follows:

$$\eta_{ohm} = j \cdot \sum_i R_i = j \cdot R_{tot}$$

The third zone at high current density is characterized by an increased voltage drop, and the diffusion polarization (η_{diff}) takes place in this zone. During the fuel cell operation with constant gas supply, the fuel utilization rate increases with increasing current density. The gas diffusion will be enhanced at high current density, which may result in gas depletion in reaction sites. Meanwhile, the produced water cannot be timely transported out.

The operation temperature of SOFC is much higher than that of PEFC, leading to improved exchange current density and decreased activation polarization. Therefore, as **Figure 2.2** shows, no obvious activation polarization zone can be observed in the polarization curve of SOFC.

2.1.4 Cell and stack components

Since the working temperature for the SOC stack is normally between 600 °C and 900 °C, thus materials used in the stack should have very good thermal and chemical stability at high temperatures. **Figure 2.3** shows the main stack components in a planar SOC stack with the Anode Supported Cell (ASC). The electrolyte should have good gas tightness to ensure complete separation of gases on both sides. Meanwhile, it should also have high ionic conductivity as well as small thickness, so that the ohmic resistance can be reduced. The material for both electrodes should show good structural/thermal/chemical stability in a strong oxidizing (air electrode) or reducing (fuel electrode) atmosphere. Additionally, the electrodes should have the porous structure to ensure the gas diffusion, reaction and transmission in the Triple Phase Boundaries (TPBs). Moreover, the thermal expansion compatibility and chemical compatibility between electrolyte and electrode materials are required, so that the chemical reaction or inter-diffusion between them can be avoided or minimized.
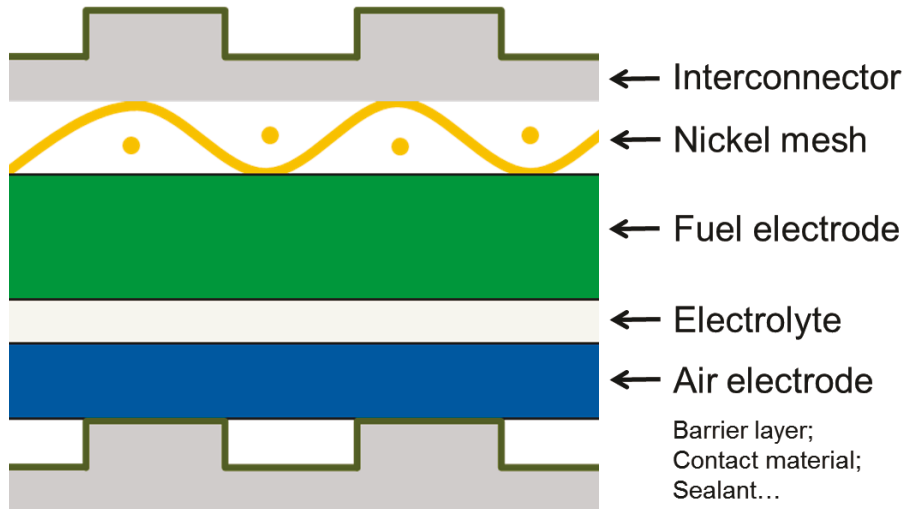
Figure 2.3: Major stack components in a planar SOC stack

– **Electrolyte:** The electrolyte conducts oxygen ions between separated electrodes which enables the overall reactions to take place. The conduction of the oxygen ion occurs via the oxygen vacancy hopping mechanism. The ionic conductivity of the electrolyte is an important factor which can determine the working temperature of the SOC stack. In order to achieve a high ionic conductivity, the crystal structure of the electrolyte material should 1) allow high level of point defect disorder and 2) low migration enthalpy [21]. Some metal oxides meet these requirements such as ZrO_2, CeO_2 with the fluorite structure, $LaGaO_3$ with perovskites structure and its derivatives [22]. The main requirements for the electrolyte in SOCs are as follows:

1) High oxygen ion conductivity (~ 0.1 Scm^{-1} at operating temperature);
2) Low electronic transference number ($< 10^{-3}$);
3) Reliable mechanical properties;
4) Thermal and chemical stability from room temperature to ~ 1000 °C at variable activities of oxygen ($1 - 10^{-22}$ atm);
5) Chemical inertness with electrode materials;
6) Compatibility of coefficient of thermal expansion (CTE) with cell components;

Currently the most widely used electrolyte material is Y_2O_3-stabilized ZrO_2, also known as YSZ. The substitution of the Zr^{4+} by Y^{3+} increases the amount of oxygen vacancies which enables the doped material to exhibit high oxygen ion conductivity. Among all the doped ZrO_2, the 8 mol.% Y_2O_3-ZrO_2 (8YSZ) exhibits the highest ionic conductivity of about 0.13 Scm^{-1} at 1000 °C [23]. Although the oxygen ion conductivity is significantly lower, the 3 mol.% Y_2O_3-ZrO_2 (3YSZ) is still of great interest because of its outstanding mechanical property. The doping mechanism for the Y_2O_3-stabilized ZrO_2 can be represented by the Kröger-Vink notation as below:

$$Y_2O_3 \xrightarrow{ZrO_2} 2Y'_{Zr} + 3O_o^x + V_o^{\cdot\cdot}$$
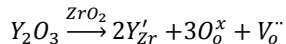
Apart from the Y_2O_3 doped ZrO_2, the Sc_2O_3 doped ZrO_2 (ScSZ) is also of great interest to the SOFC researchers. The 9 mol.% Sc_2O_3 doped ZrO_2 shows very high ionic conductivity of about 0.35 Scm^{-1} at 1000 °C [24], which makes it an ideal

electrolyte material for the intermediate temperature SOFCs (IT-SOFC). However, the ScSZ material shows phase transition and conductivity aging at high temperatures. Considering the poor accessibility and the high market price, the commercial application of ScSZ in SOFCs still needs further investigation [25].

As the superstructure of the fluorite structure, the pyrochlores based material such as $Gd_2Zr_2O_7$ exhibits comparable ionic conductivity (~0.05 Scm^{-1}) to YSZ. By substituting Zr^{4+} by Ti^{4+}, the ionic conductivity can be enhanced by two orders of magnitude [26].The pyrochlore compositions: $Gd_{2-x}Ca_xTi_2O_{7-\delta}$ (x = 0.2) with Gd^{3+} substituted by Ca^{2+}, is reported to exhibits the highest ionic conductivity [27]. However, pyrochlores based material possesses higher electron transference number but lower ionic transference number than YSZ. This material is often applied as protective film on $LaGaO_3$ or CeO_2 based electrolytes [22].

The perovskite type oxides (ABO_3) and the doped system exhibit higher ionic conductivity than most of the other oxide ion conductors [21]. However, the application of this material is limited due to 1) poor sinterability; 2) relatively high grain boundary resistance and 3) high level of p-type electronic conduction [28].

The currently used electrolyte materials in SOC stacks are listed in **Table 2.1**. The standard ASCs in Jülich have 8YSZ electrolyte.

Table 2.1: Commonly used electrolyte materials for SOC stacks [21-27].

Electrolyte materials	Conductivity (Scm^{-1})	Temperature (°C)
3YSZ	0.06	1000
8YSZ	0.13	1000
9 mol.% Sc_2O_3-ZrO_2	0.34	1000
2 mol.% Bi_2O_3-ScSZ	0.18	600
$Ce_{0.8}Gd_{0.2}O_{2-\delta}$	0.09	800
$Ce_{0.8}Sm_{0.2}O_{2-\delta}$	0.088	800
$La_{0.8}Sr_{0.2}Ga_{0.8}Mg_{0.2}O_3$	0.45	1000
$Gd_{1.86}Ca_{0.14}Ti_2O_{7-\delta}$	10.44	500 - 820
$La_{0.9}Sr_{0.1}Ga_{0.8}\,Mg_{0.2}O_{3-\delta}$	10.2	800

– **Air electrode:** During the SOFC operation, the oxygen is first adsorbed into the porous air electrode (cathode), and the oxygen reduction reaction (ORR) can occur by accepting the electrons from the external circuit. Depending on the nature of the air electrode material, the ORR can take place either on the electrode/electrolyte/gas interface or on the electrode/gas interface. The oxygen ions are then transported through the electrolyte to the fuel electrode side (anode), where the fuel gas is oxidized. In order to enable these processes to take place, the air electrode material should be an electronic conductor or mixed ionic and electronic conductor (MIEC). The general requirements for the air electrode material for SOCs are as follows [29-31]:

1) High electronic conductivity (> 100 Scm^{-1} under oxidizing atmosphere);
2) High oxygen ion conductivity;
3) High catalytic activity for the ORR;
4) Sufficient porosity;
5) Minor mismatch between the CTE values and good chemical compatibility with other cell components;

6) Good stability under oxidizing atmosphere;

Considering the requirements listed above, the metal oxides have become the most ideal material for air electrodes in SOCs. Among them, the perovskite based oxides of the general formula ABO_3 is of particular importance. The A-sites are occupied by lower valence cations (La, Sr, Ca, Ba, etc.), while the B-sites are occupied by higher valence reducible transition metal (Ti, Cr, Ni, Co, Fe, etc.). Before doping, most of the perovskite materials show poor oxygen ion conductivity in air. By partially substituting the A-site (or B-site) cation with Sr^{2+}, Ca^{2+}, and Ba^{2+}, or the reduction of Mn^{3+} (Co^{3+}) to Mn^{2+} (Co^{2+}), the oxygen defects will form and the oxygen ion conductivity increases.

For a long time, (La,Sr)MnO$_3$ (LSM) was the most common used material for the air electrode in SOFCs with YSZ electrolyte. The LaMnO$_3$ base material possess poor electronic conductivity, which can be enhanced by substituting La^{3+} with Sr^{2+}. By doping, the Mn cation will be oxidized, which increases the electron-hole concentration and the electronic conductivity. The generation of oxygen defects can be given as:

$$Mn^x_{Mn} + SrO \xrightarrow{LaMnO_3} Sr'_{La} + Mn^{\cdot}_{Mn} + O^x_o$$
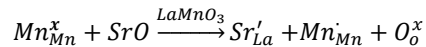
The Sr doping level can highly influence the chemical stability and the chemical compatibility of LSM with the YSZ electrolyte. At high temperatures, the pure LaMnO$_3$ will react with YSZ and form the poorly conducting La$_2$Zr$_2$O$_7$ at the air electrode/electrolyte interface. However, with high level of Sr doping (> 30 mol. %), a poorly conducting SrZrO$_3$ insulation layer will form at the air electrode/electrolyte interface. Therefore, LSM with 30 mol. % doping level possess the optimal composition for air electrode material especially in SOCs using YSZ electrolyte.

The application of LSM as air electrode material for IT-SOFCs operated under 600 °C ~ 800 °C is limited due to the poor oxygen ion conductivity during this temperature range. The materials with mixed ionic and electronic conductivity (MIEC) have been found promising for intermediate-temperature operations.

The Sr doped LaCoO$_3$-based materials (La$_{1-x}$Sr$_x$CoO$_3$ or LSC) show high mixed conductivities within a wide temperature range, which makes it an alternatives to the conventional LSM air electrode in IT-SOFCs [32]. The LSC material shows good chemical compatibility as well as similar CTE value with the GDC electrolyte. However, the application of LSC in cells with YSZ electrolyte is limited because 1) the CTE value of LSC is much larger than that of YSZ and 2) the formation of the poorly conducting La$_2$Zr$_2$O$_7$ or SrZrO$_3$ phase at the air electrode/electrolyte interface. Therefore, a barrier layer (usually GDC) must be applied at the air electrode/electrolyte interface when LSC is used with the YSZ electrolyte.

It has been found that the CTE value of LSC can be reduced with partially substituting Co with Fe (La$_{1-x}$Sr$_x$Co$_{1-y}$Fe$_y$O$_3$ or LSCF). However, the ionic conductivity is reduced due to the Fe doping [33]. While the LaCoO$_3$-based air electrode materials (e.g. LSC and LSCF) are used with YSZ electrolyte, a barrier layer is required at the air electrode/electrolyte interface to prevent the formation of poor-conductive zirconates interlayer from the interfacial reactions.

– **Fuel electrode:** The electrochemical oxidation of fuel gas takes place at the fuel electrode when the cell is operated under SOFC mode. The oxygen ion generated from the ORR process at the air electrode is transported through the electrolyte to the fuel electrode, where hydrogen is oxidized and forms water. As this reaction proceeds, electrons are released to the external circuit. The desired properties of the fuel electrode are as following [21, 34]:
   1) High electronic and ionic conductivity;
   2) High electrocatalytic activity towards the fuel gas oxidation;
   3) Chemical stability at high temperatures;
   4) Chemical stability under reducing atmosphere;
   5) Minor mismatch between the CTE values and good chemical compatibility with other cell components;
   6) Stable porous structure with sufficient mechanical strength;

Due to its good chemical stability, excellent catalytic activity towards hydrogen oxidation and low cost, Nickel was used as the earliest fuel electrode material [21]. However, the CTE mismatch between pure Ni and the commonly used YSZ electrolyte would weaken the attachment with electrolyte.

Developed in the 1970s, the Ni-YSZ cermet (usually with 40–60 wt% Ni) has become the most commonly used fuel electrode material in SOCs due to its high electronic conductivity, good ionic conductivity and good catalytic activity towards hydrogen oxidation [35]. The introduced YSZ phase can effectively reduce the CTE of the Ni fuel electrode to match that of the electrolyte material. Moreover, the YSZ phase is a good oxygen ion conductor, which can extend the active areas for the electrochemical oxidation reactions at fuel electrode [36]. The stability of Ni/YSZ as fuel electrode has been proven up to more than eighty thousand hours operation by Forschungszentrum Jülich [37-40]. However, when the cell is operated with too high fuel utilization rate, sealant leakage or the fuel supply is cut-off, the redox instability occurs with the Ni/YSZ cermet, in which the Ni is oxidized to NiO resulting in volume expansion by the anodic re-oxidation [41-43]. The coarsening or agglomeration of nickel particles occurs during the long-term operation at high temperatures (600 °C – 1000 °C) [44]. The Ni/YSZ fuel electrode is also susceptible to carbon deposition or coking when using hydrocarbons as fuel gases [45]. The presence of impurities in the fuel gas especially sulfur (e.g. H_2S) can lead to a serious impact on the performance of the Ni/YSZ fuel electrode [46].

The standard Anode-Supported Cells (ASCs) in Forschungszentrum Jülich currently use Ni/YSZ as fuel electrodes, which have shown excellent stability during the long-term stack tests [40, 47-50]. Alternative fuel electrode materials have been developed with improved tolerance to carbon deposition or poisoning. The Cu/YSZ cermet is considered as an alternative to the Ni/YSZ cermet since Cu has been proved inactive to carbon deposition during the reformation of hydrocarbon fuel gases [51]. The Cu phase functions as an excellent electronic conductor. However, the relatively lower melting point of Cu (1083 °C) than Ni (1453 °C) limits the application of Cu/YSZ fuel electrodes to low temperature operation [52].

The Ni-free conductive metal oxide based perovskites were developed, which exhibit electronic/ionic conductivity and good sulfur tolerance [53, 54]. However, $SrTiO_3$ shows poor electrocatalytic activity towards the electrochemical oxidation of hydrogen, but remarkable activity for the CH_4 oxidation at high temperatures [55, 56]. The $(LaSr)(FeCr)O_3$ based materials are proved to be active towards the methane oxidation at high temperatures [57]. With proper doping in the $La_{0.7}Sr_{0.3}Cr_{1-x}Fe_xO_{3-\delta}$ series materials (x = 0.2, 0.3, 0.4 and 0.5), appreciable sulfur tolerance can be expected (up to 50 ppm H_2S) [58].

– **Inter-diffusion barrier layer:** When using LSC or LSCF as air electrode with the traditional 8YSZ electrolyte, there will be formation of low conductive zirconates between the air electrode and electrolyte during the sintering process [59]. In order to prevent the interdiffusion, a barrier layer is usually applied in between. Gadolinia doped ceria (GDC) is one of the most commonly used materials for the barrier layer in SOCs as it has high oxygen ion conductivity and chemical stability during cell operation [60].

The GDC layer can be produced by physical vapor deposition (PVD) and screen printing. The PVD-GDC barrier layer exhibits very high densification, which is considered as the major factor determining the functionality of the barrier layer [61, 62]. However, the rather thin PVD-GDC layer can lead to additional pathways for the Sr and Zr diffusion along grain boundaries [63]. Additionally, the application of the PVD technique for the scale-up process is limited due to the intensive cost.

The fabrication of the GDC barrier layer in the standard ASCs in Forschungszentrum Jülich is achieved through screen printing. The screen printing process is widely used due to its cost-effectiveness especially for the large-scale fabrication. The GDC sintering temperature is the key parameter which can determine the functionality of the GDC barrier layer as well as the post-sintering process of the air electrode. For the GDC layer sintered at low temperatures of ~1100 °C, after the LSCF post-sintering on GDC, continuous $SrZrO_3$ formation can be observed at the GDC/electrolyte interface. Moreover, the GDC barrier layer suffered from the redistribution of Gd, leading to the formation of CoO and $FeGdO_3$ as a result of the

diffusion of Gd into YSZ and LSCF. In contrast, the high-temperature sintered GDC layer (~1400 °C) experienced no post-sinter effect during the LSCF sintering and the SrZrO$_3$ formation was suppressed [64, 65].

– **Interconnector and protective coating:** The interconnector provides connection between adjacent cells in an SOC stack, through which the current as well as heat is conducted. Moreover, the interconnector also functions as a barrier between the reducing (fuel electrode) and oxidizing (air electrode) atmospheres. Therefore, the interconnector materials should possess the following properties [66, 67]:

   1) High electronic and low ionic conductivity;
   2) Excellent gas tightness;
   3) Structural and chemical stability in reducing and oxidizing atmospheres at high temperatures;
   4) CTE values matching with adjacent cell components;
   5) Moderate mechanical strength;
   6) Cost-effectiveness;

Two classes of materials have been used for interconnectors, including ceramics and metallic alloys. The LaCrO$_3$ based ceramics exhibit high electronic conductivity (~ 1 Scm^{-1} at 1000 °C), which can be further enhanced by doping La with Ca or Sr [68, 69]. The CTE mismatch between the LaCrO$_3$ based ceramics and YSZ is very low (~ 1%) and the compatibility with other cell components is quite good [70]. However, the application of the doped LaCrO$_3$ as interconnector material in SOC stack is limited by its poor sinterability in air, high cost of raw materials and reduced conductivity at intermediate temperatures (< 800 °C) [71].

The metallic materials have become alternatives for the interconnectors in the SOC stacks operating at intermediate temperatures (650 °C ~ 850 °C). Currently, several kinds of metallic materials such as Ni-based alloys, ferritic stainless steel and Cr-based alloys have been developed for metallic interconnectors in SOC stack [72]. Among them, the ferritic stainless steel shows similar CTE as other SOC stack components, and the manufacturing process is quite simple [73]. Therefore, the

ferritic stainless steel has become the most commonly used interconnector material in SOC stack. Developed by the Research Center Juelich (Germany) and commercialized by the ThyssenKrupp VDM (Germany), the Crofer22 series ferritic stainless steel has become the most commonly used metallic interconnector material due to the strong antioxidant properties and good conductivity at high temperatures [74].

Along with the development of metallic interconnector material, the protective coatings which protect the interconnector materials from degradation (e.g. oxidation, Cr evaporation and oxide spallation) have been developed in recent years. The protective coatings should meet the following requirements [67]:

1) High electronic conductivity;
2) Low diffusion coefficients of Cr and O;
3) Structural and chemical stability in reducing and oxidizing atmospheres at high temperatures;
4) Chemical stability with adjacent stack components;
5) CTE values matching with interconnector material;

Three classes of protective coatings have been developed, including the nitride coating (e.g. CrN, Cr-Al-ON), the perovskite coating (e.g. $LaCrO_3$, LSM and LSCF) and the spinel coating (e.g. $CoCrO_4$, $(Mn,Co)_3O_4$ and $MnCo_2O_4$) [75-77]. Among them, the thermally-grown $(Mn,Co)_3O_4$ is proved to have improved stability and functions as barrier layer to the inward oxygen diffusion and the out ward chromium diffusion [78]. For the Jülich stacks, manganese cobalt ferrite (MCF or $(Mn,Co,Fe)_3O_4$) is used as the standard protective coating on the Crofer 22 APU interconnector [79, 80]. The MCF layer applied by atmospherically plasma spray (APS) has been proved to function as an efficient Cr barrier which can reduce Cr evaporation and prevent the Cr-poisoning of the air electrode during operation [81].

– **Sealants:** In SOC stack, the key function of the sealant material is to seal the fuel gas or air in their respective chambers and prevent the mixing of the fuel gas and air. For the tubular design SOC stack, the stack is self-sealing so that the sealant is not

necessary. However, for the planar design SOC stack, the performance of the stack is highly related to the sealing condition. The sealant material needs to fulfill the following requirements [82-85]:

1) No gas leakage;
2) CTE values matching with other stack components;
3) Tolerance to thermal cycling and thermal shock;
4) Long-term structural and chemical stability in reducing and oxidizing atmospheres at high temperatures;
5) Chemical compatibility with adjacent stack components;
6) Resistance to hydrogen cracking;
7) Intrinsic insulating;
8) Cost-effectiveness;

Currently various types of sealant materials are used for SOC stacks such as metal, brazes, mica based composites and glass ceramics. Depending on the sealing methods, the sealing in SOC stacks can be divided into compressive sealing and rigid sealing [86].

In the compressive sealing, the sealant material is fitted in-between the two sealing surfaces, and the gas-tight sealing is achieved through applying external compressive load to the sealing surfaces. The sealant material is not bonded to the adjacent stack components, thus the CTE matching is not required for the sealant material. The sealant material should exhibit the flexibility to deformation and render compression. Metals and mica based materials are the two types of materials which fulfill these requirements.

Among the metallic materials, the noble metals (e.g. Pt, Au, Ag) are the most appropriate sealant materials due to the high melting points and strong resistance to oxidation. After taking the cost-effectiveness into account, only Ag can be used as sealant material. However, several problematic issues relating to using Ag as sealant material have been reported. The yield strength of sterling silver is too high, resulting in the insufficient deformability of the sealant to render the compression [87]. Since the solubility of hydrogen and oxygen in silver is high, the formation of water in the

sealant is observed after exposing to the atmosphere of both fuel and air electrodes, which result in the failure of the sealant. Moreover, high porosity will develop in the silver due to the high vapor pressure when exposing to humidified hydrogen.

The mica-based material is another type of the compressive sealing material. Muscovite ($KAl_2(AlSi_3O_{10})(F, OH)_2$) and phlogopite ($KMg_3(AlSi_3O_{10})(OH)_2$) are the two main types of mica used as sealants [88, 89]. However, the pure mica sealant shows high gas leakage rate. The hermeticity can be improved by improving the mica-layer thickness. Additionally, after combined with other materials (e.g. glass or silver), the hermeticity of pure mica can be further improved to an acceptable level [86].

For the rigid sealing, the sealants are bonded with the sealing surfaces, making the rigid sealing a relatively simpler and effective sealing method than the compressive sealing [86]. Different from the compressive sealing, the CTE matching between the sealant material and adjacent stack components is required to avoid high thermal stress during the thermal cycling. The sealant materials used for the rigid sealing include glass, glass-ceramic and alloy based braze materials.

The glass possesses relatively higher CTE value but lower strength than the ceramic material. After soaking the amorphous glass at high temperature (between the crystallization temperature and the liquid temperature) for about 2 – 10 hours, the crystallization of glass occurs and the glass-ceramic forms possessing much higher strength than the traditional glass [90]. The commonly used glass-ceramic sealant materials for SOCs are the borosilicate glass-ceramics, boron-free alkaline earth silicates, and phospho-silicate glass-ceramics [91-93].

The addition of alkaline earth metals into the glass can 1) control the crystallization kinetics; 2) improve the chemical compatibility between the glass-ceramic and the YSZ electrolyte and 3) improve the adherence to the surface and stabilizes the interface with YSZ [91, 94]. The presence of boron in glass can react with H_2O to form gaseous $B_2(OH)_2$ or $B(OH)_3$. Additionally, boron also shows high reactivity with other stack components. Therefore, glass-ceramics with low boron content such as the MgO-SiO_2-Al_2O_3-B_2O_3 system with boron content < 5 wt.% are preferred [95, 96]. The boron-free glass-ceramic sealant based on the SiO_2-Al_2O_3-CaO-Na_2O system successfully joint the Crofer22 APU interconnector and

the YSZ electrolyte through a pressureless process at 900 °C [83]. The application of phospho-silicate glass-ceramics is limited due to the relatively lower CTE values as well as the chemical instability at high temperatures [97].

The standard sealant used in the Jülich stack is the glass matrix of the BaO-CaO-SiO$_2$ system with additions of Al$_2$O$_3$, B$_2$O$_3$, ZnO and V$_2$O$_5$ (Glass H). The glass matrix is usually filled with YSZ fibers or Ag particles [98, 99]. Currently, the joining process of the SOC stack is performed at 850 °C for 100 hours to ensure that the sealant obtains a partially crystallization microstructure with sufficient mechanical stability [100].

– **Contact materials**: In the planar-design SOC stacks, the electrical contact layers are applied between the interconnector and electrodes to increase the contact area and reduce the contact resistance by providing stable electrical conduction paths between the interconnector and the electrodes [101]. For the fuel electrode, the most commonly used contact material is the Nickel mesh. However, for the air electrode, since the contact layer is applied on the interface between the ceramic electrode and metallic interconnector under oxidizing atmosphere, strict requirements are listed for the air electrode side contact materials [102-104]:

  1) Sufficiently high electrical conductivity;
  2) Adequate chemical stability and compatibility with adjacent stack components;
  3) CTE values matching with other stack components;
  4) Appropriate porosity and mechanical bonding;
  5) Cost-effectiveness;

The noble metals and electrically-conductive oxides are the materials fulfilling these requirements. The noble metals such as Pt, Au and Ag possess high melting points and sufficiently high electrical conductivity at high temperatures. Moreover, the CTEs of noble metals can be effectively modified through alloying. The application of noble metals as contact materials in SOC stacks is limited by the cost-effectiveness, which makes Ag or Ag-based alloys the only economically-viable choice as the contact material. However, the tendency of evaporation at high temperatures has

become the major drawback of Ag as contact material. The application of pure Ag is limited to SOCs operated during 600 – 750 °C. Additionally, the excessively sintering of Ag particles is observed at high temperatures, which can destroy the porous structure and thus hinder the transport of oxygen at air electrode [105, 106].

Similar as the air electrode materials, some oxides with sufficient electrical conductivity can also be used as air electrode contact materials. Two categories of ceramics have been commonly used for air electrode contact materials, including perovskites and spinels.

As discussed in the air electrode materials part, the perovskite-type oxides with the general formula ABO_3 will show acceptable electrical and ionic conductivity by proper doping. When the A-site is occupied by La or Y and the B-site is occupied by Mn, Co, Fe or Ni, the doped perovskites exhibit the p-type electronic conduction under oxidizing atmosphere, which can be used as air electrode materials, interconnector coating and air electrode side contact materials [72, 74, 107].

Among them, the $La_{1-x}Sr_xMnO_{3-\delta}$ - $La_{1-x}Sr_xCoO_{3-\delta}$ - $La_{1-x}Sr_xFeO_{3-\delta}$ quasi-ternary system was well studied and the $La_{0.8}Sr_{0.2}(Co,Fe)O_{3-\delta}$, $La_{0.8}Sr_{0.2}(Co,Mn)O_{3-\delta}$ and $La_{0.8}Sr_{0.2}(Fe,Mn)O_{3-\delta}$ series were considered as most promising air electrode side contact materials [108, 109]. An electrical conductivity > 100 Scm^{-1} as well as similar appropriate CTEs can be achieved at 800 °C for all the three series [109]. Other perovskite-type ceramics have also been investigated, including the Cu-containing $La(Mn_{0.5}Co_{0.5})_{1-x}Cu_xO_{3-\delta}$ and $(La,Sr,Ca)(Fe,Co,Mn,Cu)O_{3-\delta}$, La-based perovskites without A-site doping (LNF: $LaNi_{0.6}Fe_{0.4}O_3$ and LCN: $LaCo_{0.6}Ni_{0.4}O_3$) and Y-based perovskites ($Y_{1-x}CoO_{3-\delta}$, $Y_{1-x}Co_{1-y}Mn_yO_{3-\delta}$ and $Y_{1-x}Ca_{1-y}Mn_yO_3$) [110-114].

During the SOC operation at high temperatures, a thermally grown double-layer oxide scale (Outer layer: $(Mn,Cr)_3O_4$ spinel; Inner layer: Cr_2O_3) on the commonly used Crofer 22 APU interconnector can be observed. The outer spinel layer was found to hinder the Cr migration from the interconnector to the air electrode [115]. In order to prevent the Cr poisoning of the air electrode and reduce the contact resistance, Cr-free spinel have been developed as air electrode contact materials, including Co_3O_4, $(Mn,Co)_3O_4$, $(Cu,Mn)_3O_4$ and $(Ni,Co,Fe)_3O_4$, etc. [116-118]. By incorporating

rare earth elements such as Y and Ce into these spinels, the electrical performance and the surface stability of the metallic interconnector can be improved [119].

For the Jülich stack, the perovskite type LCC10 ($La_{1-x}Ca_xCrO_3$) layer is applied as the standard contact coating at air electrode side. It has been proved that the LCC10 contact layer can act as the Cr getter which reduces the amount of gaseous Cr species reacting with the air electrode material, thus the strong degradation of the stack can be avoided [79].

2.2 Degradation mechanisms of SOC stacks

The durability of SOC stacks is the main factor influencing the commercialization of SOC techniques. The degradation of SOC stacks are dependent on the materials used for stack components, stack processing and operating conditions. The degradation mechanisms of SOC stacks operated under SOFC/SOEC modes have been widely investigated. Due to the differences in the gas composition and polarization current under these two operation modes, the mechanisms for the performance degradation can be different. In the following part, the common degradation mechanisms observed for individual stack components under both SOFC and SOEC operation modes will be presented in the first place. The degradation mechanisms observed only under SOEC operation modes are presented afterwards.

2.2.1 Degradation under SOFC mode

– **Fuel electrode:** As discussed above, the Ni/YSZ cermet is the most commonly used material for fuel electrodes in SOCs, thus the durability of this material is one of the most important factors influencing the lifetime of SOCs.

During the long-term SOC operation, the grain growth of Ni particles was observed by researchers [38, 120, 121]. It has been proven that the Ni particle coarsening and the Ni particle size distribution (PSD) broadening would result in the decreasing of electrical conductivity [122]. The difference between Ni particle size was considered to be the driving force for the growth of larger Ni particle, and the Ni atom surface diffusion was the dominant diffusion mechanism [123]. The structure of the YSZ skeleton was assumed to have influence on the Ni particle growth. Studies have shown that with finer initial YSZ structure, the Ni coarsening will be more intensive [124].

The Ni growth will result in the decrease of TPB length, which further increases the polarization resistance. According to the results from the experiments combining

TPB determination with Ni/YSZ degradation, significant stack degradation has been observed with the decrease in TPB length [125, 126].

The Ni content and the Ni-Ni connection in the Ni/YSZ cermet also showed great impact on the durability of the fuel electrode. The degradation of Ni/YSZ fuel electrode was proved to be extremely sensitive to the Ni content [120]. Besides the Ni grain growth, the Ni evaporation in the form of volatile species is the mechanism of Ni loss. It has been concluded that the Ni would evaporate mainly as volatile $Ni(OH)_2$ during the operation [37, 126, 127]. With higher operation temperature and higher water partial pressure, the Ni evaporation rate will be increased.

The loss of Ni-Ni connection or Ni contact was characterized by the formation of insulating rims of impurities around Ni particles [128]. The loss of Ni contact will reduce the density of active TPBs, which increases the polarization resistance. Additionally, the ohmic resistance may also be influenced with severe loss of Ni contact [129].

The high working temperature makes it possible for using non-hydrogen gases such as hydrocarbon, carbon monoxide and ammonia as fuels. The carbon deposition has become a degradation mechanism for the Ni/YSZ fuel electrode. The deposited carbon will not only block active TPBs, but also destroys the electrode structure and forms carbon nanotubes [130].

Trace impurities in the fuel gas such as sulphur, chlorine and phosphorous could be introduced to the fuel electrode and lead to the stack degradation. Even very low amount of the impurities in the fuel gas will lead to significant fuel electrode degradation [131-133]. The trace elements will poison the fuel electrode by decreasing the active Ni sites, which increases the polarization resistance and leads to an instant voltage drop (SOFC mode) [134-136].

– **Air electrode:** Different kinds of material featured with different types of conductivity have been developed for the oxygen electrodes in SOCs. For a long time, (La, Sr)MnO_3 (LSM) was the most common material for the air electrode in SOFCs, as it has excellent chemical and thermal compatibility with the yttria-stabilized zirconia (YSZ) electrolyte. The single phase (La,Sr)MnO_3 (LSM) is a kind of electronic

conductors with low ionic conductivity [137]. While the cell operates at low temperature, the high overpotential on the LSM air electrode and the low oxygen activity at the LSM/YSZ interface will lead to the formation of zirconate at the interface and the air electrode delamination [138]. At high temperature, the interface densification, monoclinic zirconia formation and Mn oxide exsolution are observed after operation [139, 140].

When using Cr_2O_3 forming alloys (e.g. Crofer 22 series stainless steels) as interconnector materials, the formation of Cr^{6+} gaseous species such as CrO_3 or $Cr_2(OH)_2$ (in the presence of H_2O) at the SOC operation temperatures can be significant [141]. These volatile species can react with the $LaMnO_3$ based air electrodes, resulting in the change in the composition from $(La,Sr)MnO_3$ to $(La,Sr)(Mn,Cr)O_3$. Moreover, these species can participate in the ORR process at TPBs in the air electrode according to the following equations:

$$2CrO_3(g) + 6e^- = Cr_2O_3 + 3O^{2-}$$

or

$$2Cr(OH)_2O_2(g) + 6e^- = Cr_2O_3 + 2H_2O + 3O^{2-}$$
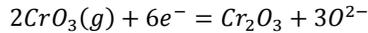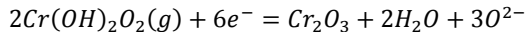
These reactions will lead to the deposition of Cr_2O_3 at the air electrode/electrolyte interface, which can seriously degrade the air electrode performance by reducing the TPB sites and blocking the ORR process [141, 142].

The mixed conducting $LaCoO_3$-based materials, such as $La_{0.6}Sr_{0.4}CoO_{3-\delta}$ (LSC) and $La_{0.6}Sr_{0.4}Co_{0.2}Fe_{0.8}O_{3-\delta}$ (LSCF), which show high electronic conductivity as well as high oxygen ion conductivity, have been considered alternatives to the conventional LSM air electrode [32]. The Sr surface segregation and Co segregation have been reported as the degradation mechanisms of LSCF air electrode. However, the Sr and Co surface enrichment was only observed after high cathodic polarization of LSCF [143]. The Sr segregation was also observed in LSC air electrodes [144, 145]. Through the SIMS test on the long-term degraded LSCF air electrodes, the Sr-rich deposits were observed on the surface of barrier layer preferentially in the gas flow

direction [146]. The observation indicates that the Sr is most likely transported as the volatile $Sr(OH)_2$.

It has been reported that the cobalt and iron rich air electrodes (e.g. LSC, LSF, and LSCF) can react with the zirconia based electrolyte (e.g. 8YSZ) at high temperatures, forming La- or Sr-zirconates (e.g. $La_2Zr_2O_7$ or $SrZrO_3$) with poor ionic conductivity at the air electrode/electrolyte interface [147, 148]. Even with a dense barrier layer (GDC) at the interface, the Sr diffusion from the air electrode to the electrolyte cannot be prevented [149]. The formation of the zirconates with poor ionic conductivity at the air electrode/electrolyte interface will hinder the transport of oxygen ions and increase the overall resistance.

– **Electrolyte:** Due to the high ionic conductivity in a wide range of p_{O_2} at high temperatures, The 8 mol.% Y_2O_3 stabilized ZrO_2 (8YSZ) has become the most commonly used electrolyte material for SOCs. However, since the 8YSZ is located in the two phase field at the SOC operation temperatures, the phase separation can occur which will result in the conductivity degradation of the electrolyte [150]. Other mechanisms leading to the conductivity degradation of the electrolyte include the coherent growth of precipitates, local ordering or micro-domain formation and formation of inhomogeneous composition phase boundaries [151].

The ceria based electrolytes (e.g. SDC or GDC) exhibit high ionic conductivity at intermediate temperatures (500 – 700 °C). However, the reduction of Ce^{4+} to Ce^{3+} can occur under reductive atmosphere, resulting in high electronic conductivity, volume expansion and inferior mechanical properties. Therefore, a protective coating of a stable electrolyte (e.g. doped zirconia) should be applied to the ceria based electrolyte at the fuel electrode side. It must be noted that the sintering temperature of this bilayer electrolyte should stay below 1200 °C to avoid the formation of solid solutions with poor ionic conductivity [152, 153].

– **Interconnector:** For the IT-SOC stacks, metallic materials are always used as interconnectors. Among them, the Crofer22 series ferritic stainless steels are the most commonly used material due to the strong antioxidant properties and good

conductivity at high temperatures. The oxidation resistance of the Crofer22 series ferritic stainless steels is achieved through the formation of a protective surface scale e.g. Cr_2O_3, which can retard the oxidation of the substrate material. At the high operation temperatures of SOCs, the Cr_2O_3 will be further oxidized to volatile CrO_3 or $Cr_2(OH)_2$. The Cr^{6+} is reactive to Mn forming the spinel $(Mn,Cr)_3O_4$. Therefore, when using LSM as air electrode, an outer spinel layer containing $(Mn,Cr)_3O_4$ will form on the surface of the Cr_2O_3 scale.

The growth of the double-layer oxide scale under high temperature can be described with the following equation [67]:

$$X^2 = K_p t + C$$

where X is the thickness of the oxide scale, t is time. K_p and C are constants.

The growth of the poor conductive oxide layer will decrease the conductivity of the interconnector as well as increase the contact resistance. Moreover, the mismatch of the CTE values between the oxide scale and the substrate material will result in the cracking and spalling with the scale. As discussed in **Chapter 2.1.4**, the application of the air electrode contact material can efficiently decrease the overall interfacial resistance. However, with the oxide scale growing, spallation will occur due to the thermal stress between the coating and the substrate material, which can result in the increasing of contact resistance or even the loss of hermeticity of the interconnector [154].

Due to the different CTE values between the metallic interconnector and the adjacent ceramic components, thermal stress will generate during the thermal cycling, which can result in the high temperature creep deformation of the interconnector. The creep deformation, especially with thin metallic interconnector, is an important issue in stacks since it can affect the contact condition and the gas tightness. By adding Ni and Si to Crofer 22 APU, Laves phase will precipitate at the grain boundaries and within grains, thus the creep resistance of Crofer 22 APU can be enhanced by the precipitation strengthening [155].

2.2.2 Degradation under SOEC mode

– **Fuel electrode:** As the steam/H_2 ratio increases under electrolysis mode, the oxygen partial pressure p_{O_2} also increases at the fuel electrode side. This would accelerate the nickel hydroxide formation and the nickel surface transport, which can lead to more significant nickel agglomeration and nickel evaporation than that under fuel cell mode [156, 157].

During the long-term steam electrolysis at high current density of 1 Acm^{-2}, nickel depletion was observed in the first 10 μm region of the Ni-YSZ fuel electrode near the electrolyte (AFL: Anode Function Layer). After the SOEC operation, a porous YSZ layer with much poorer conductivity than the dense electrolyte formed instead of the dense AFL, which can lead to significant increasing of the ohmic resistance. Moreover, small pores formation was observed at the fuel electrode/electrolyte interface [12].

Due to the higher steam concentration under electrolysis mode, the fuel electrode degradation with Si-contaminant from the glass sealant is promoted due to the high partial pressure of $Si(OH)_4$ over silicates. The deposition of SiO_2 and the formation of glassy phase silicate at the TPBs in the Ni-YSZ electrode have been considered as the major degradation mechanisms for the initial performance loss [127, 158].

The risk of carbon deposition at the fuel electrode is increased due to the fact that the oxygen is carried away from the fuel electrode to the air electrode. However, the deposition mainly occurs at the fuel electrode/electrolyte interface rather than on the electrode surface observed during fuel cell operation [159, 160].

– **Air electrode:** Under the SOEC operation conditions, the most common degradation of LSM air electrodes is the air electrode delamination at the air electrode/electrolyte interface, which can lead to sharp increase of the ohmic/polarization resistance and the stack voltage under galvanostatic electrolysis operation [8]. The delamination mechanism is the buildup of high internal oxygen pressure at the electrode/electrolyte interface due to the local high oxygen chemical potential under the anodic overpotential under SOEC mode[161, 162].

The formation of $La_2Zr_2O_7$ is observed at the LSM/YSZ interface under both fuel cell and electrolysis operation [15]. The formation of this poor conductive zirconate will weaken the contact between the air electrode and electrolyte, as well as increasing the overall ohmic resistance. However, it has been observed that the amount of $La_2Zr_2O_7$ increases with increased electrolysis current density. The mechanism of this phenomenon is the high oxygen partial pressure at the air electrode side with anodic polarization current, which makes the formation of $La_2Zr_2O_7$ thermodynamically favorable [15].

The MIEC air electrodes (e.g. LSC and LSCF) exhibit better structural and chemical stability than LSM under SOEC operation mode [163, 164]. The application of the GDC barrier layer is required when using the cobaltite-based air electrodes due to the high activity to the YSZ electrolyte, resulting in the formation of $SrZrO_3$ at the air electrode/electrolyte interface. Without the GDC barrier layer, the delamination of LSCF air electrode can also be observed under electrolysis operation mode [165].

With the anodic polarization under electrolysis mode, the SrO segregation is accelerated, which can result in the formation of SrO on the air electrode surface and the Sr/Co depletion inside the electrode [166, 167]:

$$La_{0.8}Sr_{0.2}MnO_3 \xrightarrow{Anodic\ polarization} xSrO + La_{0.8}Sr_{0.2-x}MnO_3$$
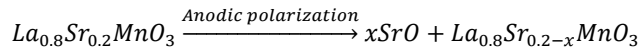
For the cobaltite-based air electrodes, the Sr-depletion is proved to be charge compensated by the reduction of Co^{4+} to Co^{3+} through the XANES analysis, which may degrade the electrical conductivity as well as the electrocatalytic activity of the LSCF air electrode [10].

Additionally, the accelerated SrO segregation at the air electrode under SOEC operation modes can promote the air electrode degradation by contaminants, especially with the volatile Cr-species (e.g. CrO_3 and $CrO_2(OH)_2$) from the stainless steel alloy used as the interconnector. For the LSM air electrode, the formation of $SrCrO_4$ instead of the $(Cr,Mn)_3O_4$ spinels is observed at the electrode/electrolyte interface under electrolysis mode, due to the fact that the generation of Mn^{2+} is suppressed under the anodic polarization conditions at the air electrode [168, 169].

For the cobaltite-based air electrodes, the Cr deposition is observed mainly on the air electrode surface in the form of $SrCrO_4$, $CrO_{2.5}$ and Cr_2O_3 [170]. The formation of $SrCrO_4$ will in turn accelerate the SrO segregation, resulting in Sr-depletion inside the air electrode and the electrocatalytic activity degradation of the air electrode.

– **Electrolyte:** When the SOC is operated in electrolysis mode, the oxygen activity at the fuel electrode/electrolyte interface decreases, but increases at the air electrode/electrolyte interface. Therefore, the oxygen activity at the two interfaces is divergent and the oxygen activity gradient across the cell is increased. In the electrolyte/air electrode interface the oxygen activity in the electrolyte can exceed the standard free energy of oxygen formation and therefore allows the formation of oxygen. Based on this mechanism, the oxygen ions from the hydrogen electrode can form oxygen bubbles in the YSZ grain boundaries close to the air electrode [14]. As a consequence, it will lead to the damage and internal fracture formation in the electrolyte near the air electrode, which can result in the increase of ohmic resistance [171].

2.3 Electrochemical Impedance Spectroscopy

Electrochemical impedance spectroscopy (EIS) is a powerful diagnostic technique that can enhance the understanding of the degradation mechanisms dominating in operating stacks since the technique may provide information on individual losses, including oxygen reduction reaction kinetics, mass transport processes, and electrolyte resistance loss.

2.3.1 Theoretical basis

While testing, the system is applied with a sinusoidal voltage which can be expressed as:

$$E_t = E_0 \sin \omega t\,; \ \ \omega = 2\pi f$$

E_0 is the amplitude of the AC voltage, ωt is the phase of the voltage and f is the frequency. **Figure 2.4(a)** shows the relationship between the input voltage (E) and time (t).

The output current generated with the input voltage is recorded by the instrument. Since the electrochemical reaction can be regarded as a Pseudo-linear system, the output current signal would have the same frequency and shape as the input voltage. But the current signal shows a phase shift as **Figure 2.4(b)**. The output current can be expressed as:

$$I_t = I_0 \sin(\omega t + \phi)\,; \ \omega = 2\pi f$$

I_0 is the amplitude of the AC current and $(\omega t + \phi)$ is the phase of the current.
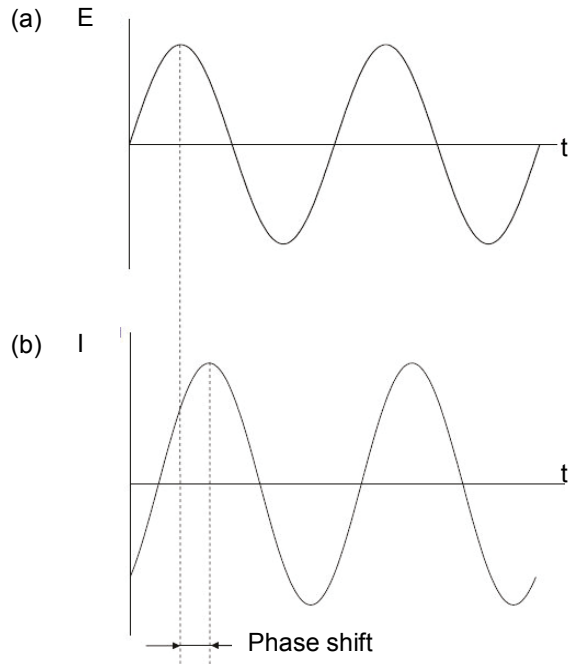
Figure 2.4: Phase shift of the current

Therefore, the impedance of the system can be written as,

$$Z = \frac{E_t}{I_t} = \frac{E_0}{I_0}\exp(-j\phi) = Z_{Re} + jZ_{Im}$$

with

$$Z_{Re} = Z' = |Z| \cdot cos\phi$$

$$Z_{Im} = Z'' = |Z| \cdot sin\phi$$

$$j = \sqrt{-1} = \exp(j\pi/2)$$

The obtained impedance data are usually plotted as Nyquist plot or Bode plot for preliminary analysis. **Figure 2.5** shows the typical Nyquist and Bode plot recorded on an anode supported cell in a SOFC short stack.
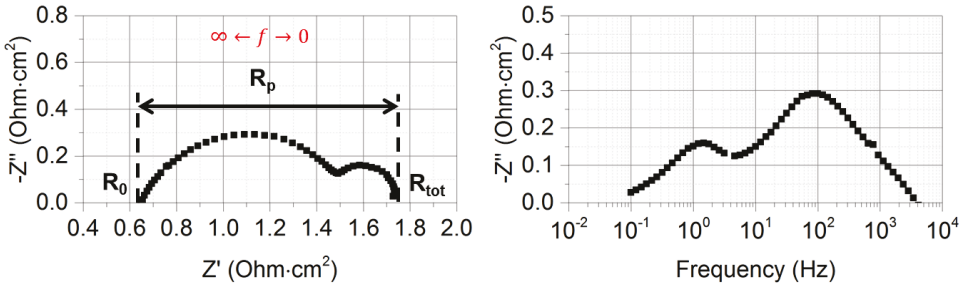
Figure 2.5: Nyquist and Bode plot of an anode supported cell.

The Nyquist plot uses Cartesian coordinates in two dimensions in which the abscissa is the real axis and the ordinate is the imaginary axis. The Nyquist curve intersects with the real axis at high and low frequencies.   The high frequency intersection between the Nyquist curve and the real axis corresponds to ohmic resistance of the system (R_0) while the intersection in the real axis at low frequency is the total impedance of the system at a certain operation point (R_{tot}). The difference between the total impedance and the ohmic resistance is the polarization impedance (R_p), which describes the polarization behavior of the system.

The Bode plot uses frequency as the abscissa, while the ordinate normally uses the imaginary impedance Z", the impedance magnitude $|Z|$ or the phase angle ϕ. The peak shown in the Bode plot functions similar as the arc in the Nyquist plot, which also describes the polarization behavior of the system under test.

2.3.2 Equivalent circuit modeling

To describe the behavior of the impedance measured, different impedance elements can be used for equivalent circuit modeling. In this section only a few simple impedance elements are described such as resistance, inductance, capacitance and the constant phase element. For equivalent circuit modeling, other frequency dependent elements are used as well. Frequency-dependent elements consist among others of the Warburg element describing mass transport losses and the constant-phase element describing the double layer capacitance at the electrodes and the Gerischer element.

The simplest impedance element is the resistor. Resistors are used to describe ohmic resistance in terms of electron conduction and ion conduction. The impedance of a resistor is the resistance as given in the following equation.

$$Z_R = R = Z'_R;$$
$$Z''_R = 0$$

As the equation shows, the impedance of a resistor only has the positive real part which is not frequency dependent. **Figure 2.6** shows the Nyquist and Bode plot of a pure resistor (R = 100 Ohm). In the Nyquist plot, a pure resistor is shown as one point in the real axis. The impedance ($|Z| = 100\ Ohm$) and phase angle ($\phi = 0°$) are independent of the frequency.
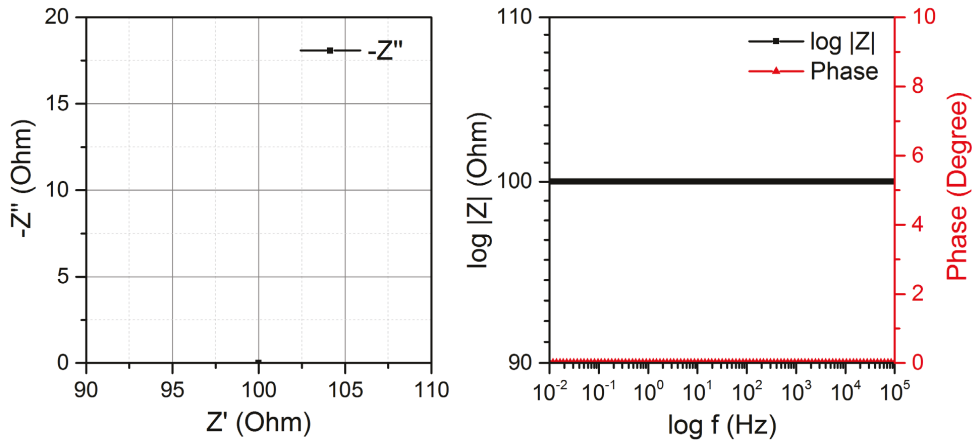
Figure 2.6: Nyquist plot and Bode plot of a pure resistor.

The inductance is used to describe the high frequency inductance. The high frequency inductance is often caused by self-inductance in the device under test, and may also be caused by inductance originating from the leads used to connect to the test object. The impedance of an inductor is given by the following equation:

$$Z_L = j\omega L$$

As **Figure 2.7** shows, the Nyquist plot of an inductance shows a straight line coinciding with the $-Z''$ axis in the fourth quadrant. In the Bode plot, the $log|Z|$ against $logf$ is represented by a line with the slope of +1. The phase angle of an inductance is 90 ° independent of the frequency.
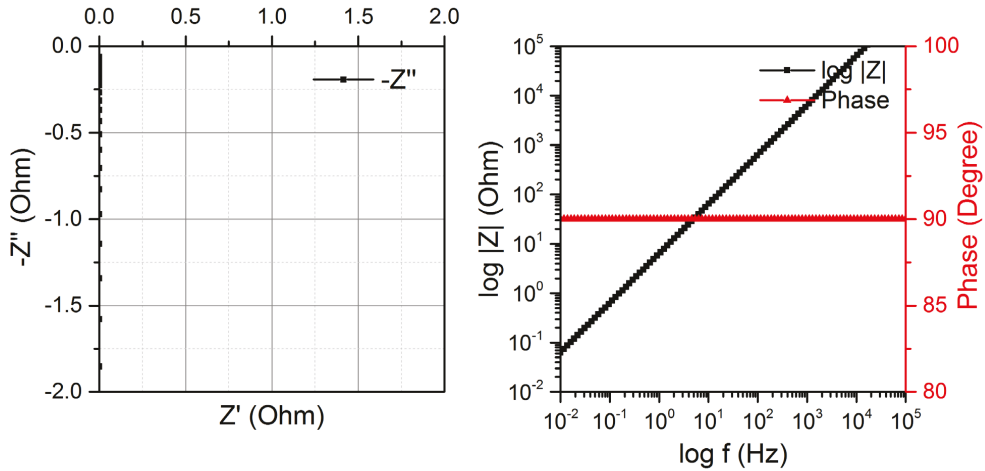
Figure 2.7: Nyquist plot and Bode plot of an inductance.

The capacitor is used to describe the double layer capacitance at the anode-electrolyte and the cathode-electrolyte interfaces and the chemical capacitance associated with concentration impedances. The impedance of a capacitor is imaginary and is described by the following equation:

$$Z_C = \frac{1}{j\omega C}$$

The Nyquist and Bode plot of a capacitor are shown in **Figure 2.8**. The Nyquist curve of the capacitor is a straight line in coincide with the $-Z''$ axis in the first quadrant without real part. The Bode curve showing the relation between $log|Z|$ and $log f$ is a straight line with the slope of -1, and the phase angle is -90 ° independent of the frequency.
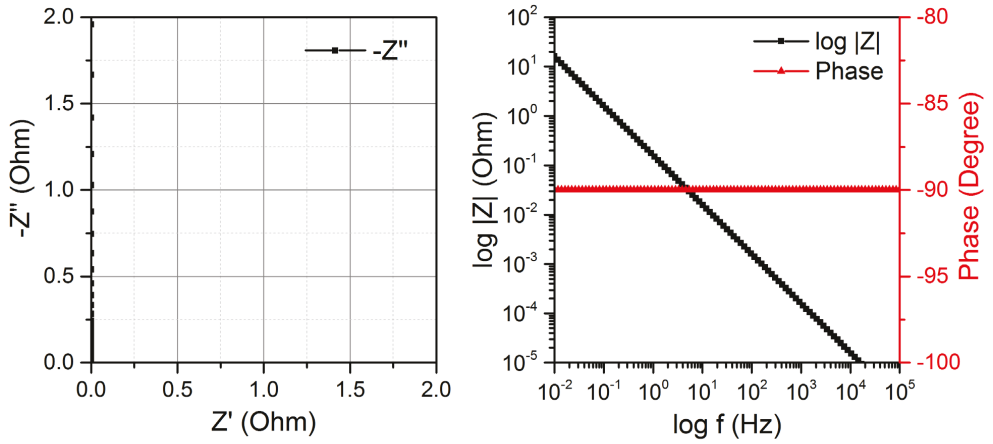
Figure 2.7: Nyquist plot and Bode plot of a capacitor.

However, the interfacial behavior in the real electrochemical system can't be simulated with a perfect capacitor. Deviation was observed between the frequency response characteristics of the perfect capacitor and that from the double layer capacitor of the solid electrode. This deviation is also called "Dispersion phenomenon", which is widely considered to be related to the porosity and the dimensional effect of the solid electrode. Thus the interfacial impedance differs from a 2D ideal capacitor plate and a CPE (Constant Phase Element) element is used instead.

$$Z_{CPE} = Z_0 \cdot (j\omega)^{-n},$$

$$Z'_{CPE} = Z_0 \cdot \omega^{-n} \cos\left(\frac{n\pi}{2}\right), \quad 0 < n < 1$$

$$Z''_{CPE} = Z_0 \cdot \omega^{-n} \sin\left(\frac{n\pi}{2}\right),$$

The tangent value of the phase angle of the CPE element could be obtained through $-Z''_{CPE}/Z'_{CPE}$:

$$\tan \phi = \tan \left(\frac{n\pi}{2} \right), \phi = \frac{n\pi}{2}$$

The phase angle is constant and independent from frequency, so that this equivalent element is named "Constant Phase angle Element". When plot $log|Z_{CPE}|$ against $log|f|$, a straight line with the slop equals to $-n$ will be obtained. A CPE elements becomes a pure resistor when $n = 0$, while it becomes a pure capacitor when $n = 1$. **Figure 2.9** shows the data from a CPE element (n=0.5).
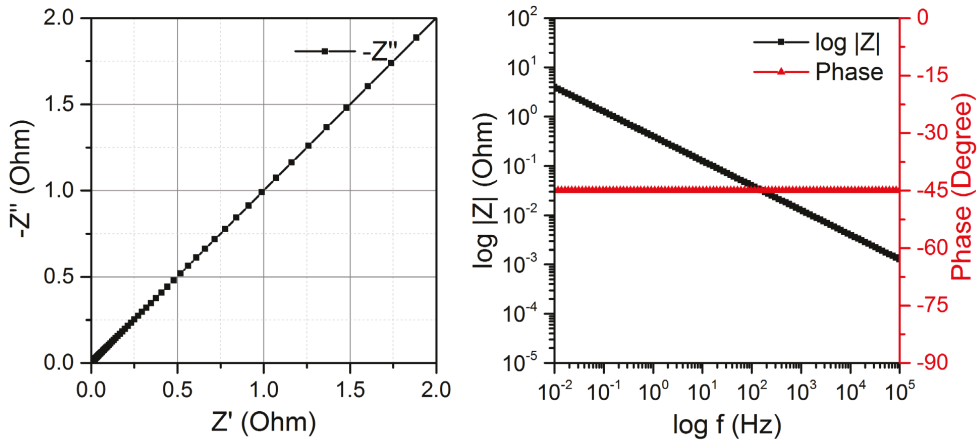
Figure 2.9: Nyquist plot and Bode plot of a CPE (n=0.5).

A parallel connection between a resistor and a capacitor is known as a RC element. The parallel RC circuit is a fundamental combination which can describe interfacial processes at electrochemical systems. The capacitor is usually replaced by a CPE as a RQ element to simulate the interfacial electrochemical process under non-ideal situation. Its complex impedance is given by the following equation:

$$Z_{RQ} = \frac{R}{1 + RQ^{-1}}$$

Figure 2.10 shows the Nyquist and Bode plots of RQ elements with different n values. When $n = 1$, the CPE equals to a pure capacitor and shows a perfect semicircle in the Nyquist plot. With decreasing the n value, a compressed semicircle is observed.
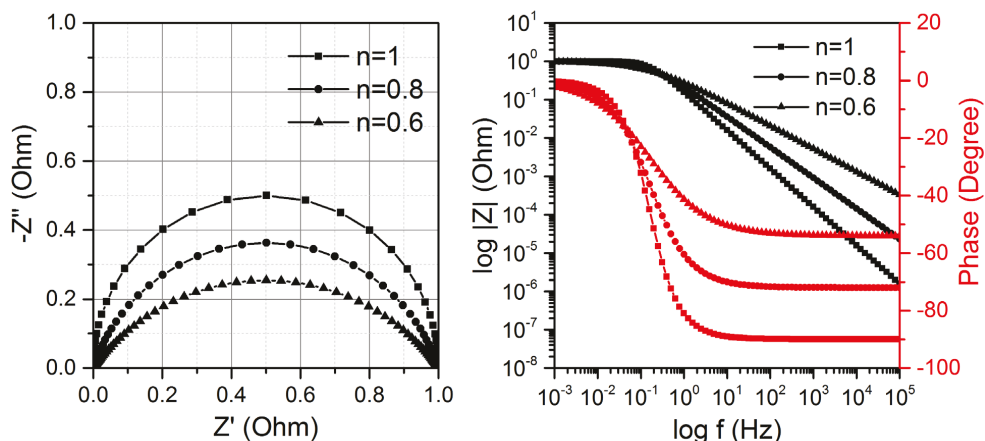
Figure 2.10: Nyquist plot and Bode plot of a parallel RQ element.

2.3.3 Distribution of Relaxation Times

The EIS technique has shown the ability of distinguishing individual impedances of the related electrochemical processes from the overall impedance, which is not possible by the DC techniques such as the IV-curve measurement. However, the overlapping of arcs can always be observed in the Nyquist plot and the resolution of the raw impedance spectrum is still not high enough. Therefore, various analysis methods of the raw impedance spectrum have been developed on the purpose of further separating and distinguishing individual impedances.

As discussed in the introduction chapter, the ECM is one of the most widely used analysis methods for EIS, but the reliability of ECM is affected due to the fact that the same impedance spectrum can be mathematically (but not physically) fitted using many different models.

The Analysis of Differences in Impedance Spectra (ADIS) is a multi-spectra analysis method developed by the Technical University of Denmark (DTU) [133, 172]. The ADIS method identifies electrochemical processes by analyzing the difference between the impedance spectra obtained under different parameters (e.g. fuel composition and temperature), so that one ADIS can be generated from two impedance spectra and not able to show all the electrochemical processes. Therefore, a large amount of experiments is required during the ADIS analysis. Moreover, the ADIS method is too sensitive to the changes in the impedance spectra, which is easily affected by even very small noise signals.

The distribution of relaxation times (DRT) was first introduced by Karlsruhe Institute of Technology (KIT) and applied to the impedance analysis of SOFCs in 1999 [17, 18, 173, 174]. The DRT method is based on the idea that every individual electrochemical process can be regarded as an RC-element which has a relaxation time (characteristic frequency). Electrochemical processes with similar characteristic frequencies cannot be distinguished in the impedance spectra and will result in the overlapped arcs observed in the Nyquist plots. With the DRT calculation, it is possible to separate the electrochemical processes with different characteristic frequencies from the impedance data.

As illustrated in **Figure 2.11**, an electrochemical system contains processes with different time constants. Each process can be represented by an RC element, thus the system is considered as a serial connection of RC elements.
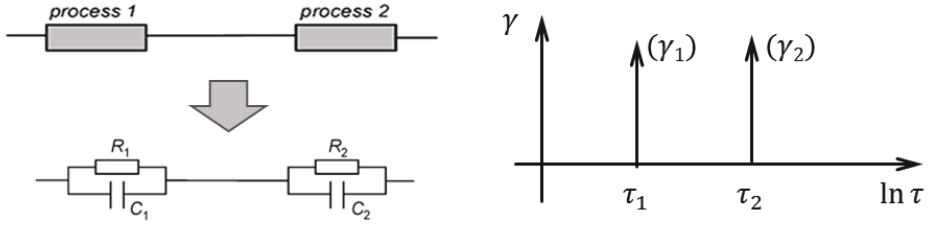
Figure 2.11: RC elements

Each RC element is characterized by its time constant τ:

$$\tau_n = R_n C_n = \frac{1}{2\pi f_n} = \frac{1}{\omega_n}; \qquad Z(\omega)_i = \frac{R_n}{1 + j\omega\tau_n}$$

So that the total impedance of an *N*-series connection of RC elements would be:

$$Z(\omega) = \sum_{n=1}^{N} Z(\omega)_i = \sum_{n=1}^{N} \frac{R_n}{1 + j\omega\tau_n}$$

With $\gamma_n = \frac{R_n}{R_{sum}}$, γ_n weights the contribution of the *n*-th process to the total impedance (γ_n :distribution function). The total impedance could be written as:

$$Z(\omega) = \sum_{n=1}^{N} \frac{R_n}{1 + j\omega\tau_n} \quad \Rightarrow \quad Z(\omega) = R_{sum} \sum_{n=1}^{N} \frac{\gamma_n}{1 + j\omega\tau_n}$$

A plot of γ_n against time/frequency can be obtained with discrete lines (shown in **Figure 2.11**) indicating the relaxation times and the weight of all the electrochemical processes within this electrochemical system.

However, physically distinct processes will merge in the real situation. Impedance data that obey the Kramers-Kronig relations can be expressed with a differential sum of infinitesimal small RC elements as shown in **Figure 2.12**.
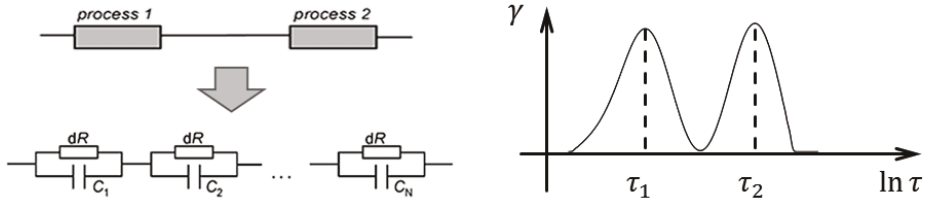
Figure 2.12: RC elements_2

The total impedance can then be written as:

$$Z(\omega) = R_{sum} \sum_{n=1}^{N} \frac{\gamma_n}{1 + j\omega\tau_n} \quad \Rightarrow \quad Z(\omega) = R_{sum} \int_0^{\infty} \frac{\gamma(\tau)}{1 + j\omega\tau} d\tau$$

Where $\frac{\gamma(\tau)}{1+j\omega\tau} d\tau$ represents the fraction of the overall impedance with relaxation time between τ and $\tau + d\tau$. As **Figure 2.12** shows, real processes exhibit γ-peaks distributed around a main relaxation time.

The equation can be regarded as the Fredholm integral equation of the first kind:

$$Z(\omega) = R_{sum} \int_0^{\infty} \frac{\gamma(\tau)}{1 + j\omega\tau} d\tau \quad \Rightarrow \quad g(t) = \int_{S_{min}}^{S_{max}} K(t,s)f(s)ds$$

- $f(s)$: the real-valued function, which in our case describes the distribution of time constants - $\gamma(\tau)$;
- $g(t)$: the experimental data, which in this work represents the experimentally measured impedance data - $Z(\omega)$;
- $K(t,s)$: the kernal.

In order to obtain $f(s)$ with known $K(t,s)$ and $g(t)$, the Tikhonov-regularization was applied to solve the Fredholm integral equation [175]. With this regularization

method, an estimate for the function $f(s)$ is obtained by minimizing the following equation:

$$V(\lambda) = \sum_{i=1}^{n} \frac{1}{\sigma_i^2} \left(g_i^{\sigma} - \left(\int_{s_{min}}^{s_{max}} K(t_i, s) f(s) ds + \sum_{j=1}^{m} a_j b_j(t_i) \right) \right)^2 + \lambda \|Lf\|^2$$

Compared with the Nyquist and Bode plots, the DRT plot shows significantly higher resolution of the merged electrochemical processes, which could help determine the number of impedance elements used for the further equivalent circuit modeling. **Figure 2.13** shows the typical Bode plot and the calculated DRT plot from a SOFC stack. Two peaks with the characteristic frequencies of ~2 kHz and 3 Hz could be identified from the Bode plot. For the DRT plot, two more peaks could be identified at the middle frequency range (10 – 1 kHz).
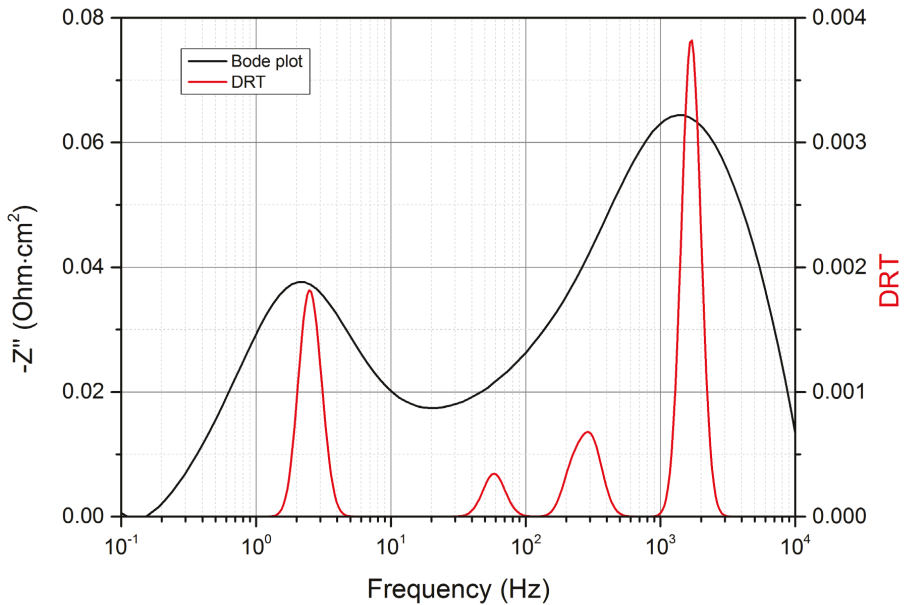
Figure 2.13: Comparison between the Bode plot and DRT plot

Figure 2.14 shows the DRT plot of the RQ elements with different n values in **Figure 2.10**. The RQ element equals to a perfect RC element when $n = 1$, and its DRT plot exhibits a straight line at the respective characteristic frequency f_c. For RQ elements with decreasing n values, the DRT plots shows broaden peaks located at the identical f_c.
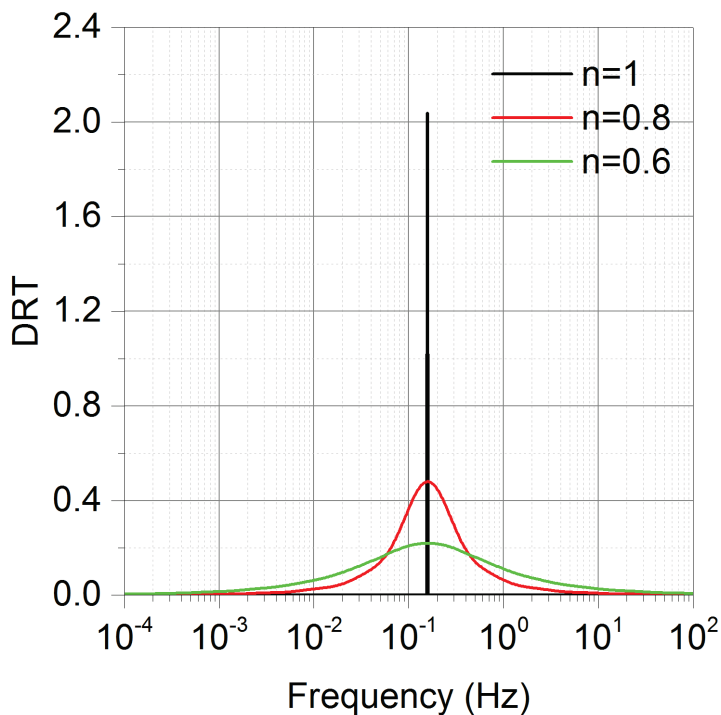
Figure 2.14: DRT of RQ element with different n values.

In 1999, DRT was first applied to the development of a comprehensive model describing SOFC single cell operation by KIT [174]. Different from the theoretical modelling based on physical laws, an alternative approach named system identification

was proposed. The cell was regarded as a technical process in a "black box" with input and output data (e.g. EIS, IV and long-term measurements) of SOFC operation. By calculating the impedance data using DRT, the physical processes occurring during SOFC operation can be distinguished according to their different time constants. With the obtained model, the relationship between the cell performance and cell parameters (e.g. material characteristics, production parameters and cell operation conditions) can be estimated, so that the cell performance can be predicted once the cell parameter is changed.

Series of EIS measurements were conducted in which one cell operation parameter (e.g. gas composition, cell temperature, current density, etc.) was varied. The EIS data were calculated with DRT and up to five processes in the SOFC cell operation were identified and related to corresponding electrodes [18]. Based on this information, the DRT can thus be applied to the degradation study of SOFCs.

As discussed in **Chapter 2.2.1**, sulfur poisoning is one of the major degradation mechanisms for the fuel electrode in SOCs. Enhanced voltage degradation could be observed once the H_2S was added to the fuel gas. The degradation rate increased with time till the poisoning was completed. By analyzing the impedance data obtained during the SOFC operation with H_2S-containing reformates via DRT, obvious development of two main DRT peaks related to 1) H_2-electrooxidation at TPBs couples with gas diffusion in AFL and 2) gas diffusion in anode substrate were observed. Therefore, the degradation of cell performance during sulfur poisoning was related to the decreased reaction rate of the electrochemical hydrogen oxidation in the anode functional layer as well as the deactivation of the fuel electrode substrate [176].

Kornely et al. investigated the effect of Cr-poisoning on an ASC with LSM air electrode at OCV condition [177]. The introducing of Cr was achieved by passing air through a Crofer22APU powder bed. After the Cr-source was switched on, the cell degradation rate was increased from 0.08 $mOhm \cdot cm^2/h^{-1}$ to 0.202 $mOhm \cdot cm^2/h^{-1.}$ With the help of DRT, the continuously evolution of the DRT peak related to the air electrode process was observed, indicating that in addition to the reduction of Cr-species at the TPB under load, the chemical reaction between LSM and Cr at OCV was also a serious degradation mechanism for LSM air electrode.

The DRT technique has also been applied to the study of SOEC single cells and stacks. Hoerlein et al, performed long-term degradation experiments (~ 1000 hours) with four SOCs at different current densities (from OCV to 1.5 Acm^{-2}) operated under SOEC mode [178]. With DRT, four processes were separated and their development was tracked during the experiments. The degradation rate was observed hardly influenced by the humidity degree of fuel gas. The evolution of the DRT peaks indicated that the faster initial degradation rate which slowed down over the operation period was mainly due to the degradation of the air electrode showing drastic initial degradation rate and then stabilized after about 500 hours. The DRT and post-mortem analysis results showed that the degradation observed at the electrolyte-fuel electrode interface should contribute to the increased degradation rate with increased current density.

As a powerful in-situ diagnosis tool, the combination of EIS and DRT has already been used for the SOEC stack characterization. Fang et al. performed a long-term test with a two layer SOEC stack for more than 20000 hours. The stack was operated at 700 °C, 750 °C and 800 °C with a electrolysis current density of 0.5 Acm^{-2} and steam conversion rate of 50%, with 50% humidified hydrogen. The voltage and area specific resistance degradation (ASR) rates were about 0.6% /kh and 8.2%/ kh after ~18460 hours operation [50]. The EIS and DRT results indicated that the main degradation mechanism was the continuously increased ohmic resistance, which was confirmed by the post-mortem analysis to be attributed to the depletion of nickel in the AFL. Moreover, a continuous slight increasing of the polarization impedance at the air electrode side was observed during the stationary operation via EIS and DRT. During the post-mortem analysis, the degradation at air electrode was observed, including the formation of $SrZrO_3$ at the electrolyte-GDC interface and the formation of SrO as well as $SrCrO_4$ on top of the cells [179].

2.3.4 Impedance measurements on SOC stacks

EIS is a very powerful AC technique for the diagnosis of electrochemical system. However, it is also a very sensitive technique which must be used with great care.

According to the Ohm's law: $R = \rho l / A$ (ρ: resistivity; l: length of the conductor; A: cell area), the cell resistance decreases when going from the button SOCs to large area SOC stacks. The AC response signal decrease respectively, which will result in lower signal-to-noise ratio of the EIS data from the SOC stack. **Figure 2.15** shows the influence of noise on high and low impedance system. With the same AC excitation current and noise, the voltage response of the high impedance system shows significantly higher signal-to-noise ratio. In order to obtain EIS data of high quality, measurements can be carried out either under noise reduced situation or with higher impedance system (e.g. at low cell temperature for SOCs).
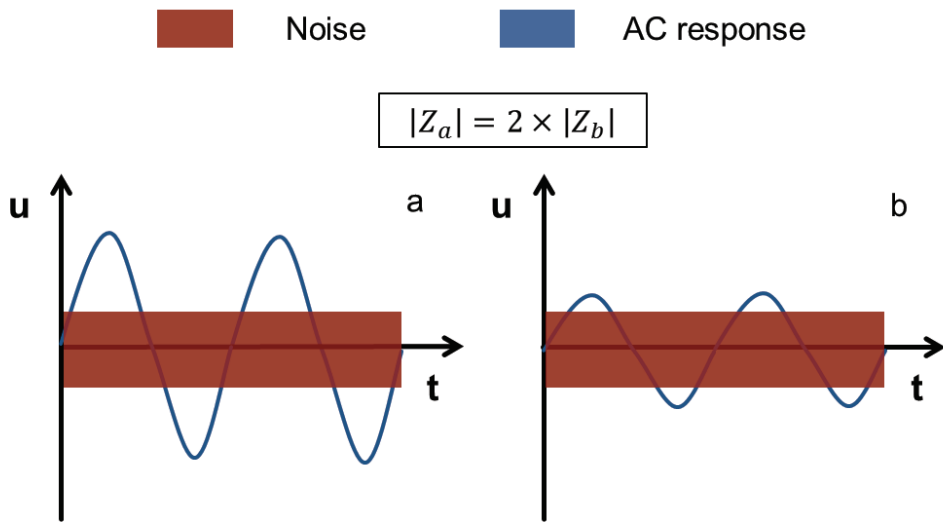
Figure 2.15: Influence of noise on a) high and b) low impedance system.

It is relatively easy to obtain good precision of measurements for impedances between 1 and 10^5 Ohm at frequencies below 5×10^4 Hz. However, it is highly possible to observe distortions for lower and higher impedances. For high impedance system, the errors mainly originate from the finite potentiostat input impedance. If this resistance is below 100 times larger than the measured impedance, a calibration procedure is necessary.

For low impedance systems like the SOC stack, the observed errors normally correspond to the inductance in series with the electrode impedance. The inductive effect becomes significant at high frequencies and leads to large positive imaginary impedances. The inductance mainly comes from that of the leads. Such effects may be often minimized by shortening or shielding the cables.

Unlike the simple and better optimized cable configuration in the button cell test, the SOC stacks are usually tested with a large testing system including built-in electric devices like power supply and electric load. Additionally, the optimization of cable configuration for EIS measurement in the large stack testing system is very difficult due to the complex design. Therefore, the influence from the electrical noise and stray impedances becomes more significant in the EIS tests with SOC stacks.

The influence of inductance on the EIS analysis has been studied by some groups. In order to demonstrate the effect of rig inductance on the EIS data of SOCs, Thompson et al. performed EIS measurements on electrolyte supported button SOCs with an active electrode area of 1.227 cm^2 [180]. Large inductive tails at high frequency were observed with the measured EIS data, which was mainly due to the inductance of the test rig. The EIS data were corrected by subtracting a variety purely simulated inductance values from the raw data and the corrected data were further analyzed with ADIS and DRT. The results indicated that due to the nature of the subtraction method, the ADIS results were less affected by the change of the inductance value. However, a small variation in the inductance value gave a large variation in the DRT spectra and could affect both the number and position of DRT peaks observed. Therefore, DRT was proved to be very sensitive to the inductive part in the EIS data.

In order to improve the reliability of DRT results, methods have been developed to exclude the influence of inductance from EIS data analysis. In the work from Raikova et al. [181], they first studied the influence of inductance on the impedance diagram through the equivalent circuit models with different inductance values. The results indicated that for the low impedance systems, the Faradaic processes at high frequencies could be affected by inductance. A multi-step procedure was used for the calibration and correction of inductance errors. The inductance value of the system was first measured via the short circuit test in which the electrodes of the cell were connected in a short

circuit. The impedance of the cell was measured afterwards with normal cabling. The inductance correction was fulfilled through subtracting the inductive part obtained in the short circuit test from the measured impedance of the cell. After correction, the process at high frequencies which was hidden due to inductance could be discovered.

Similar inductance correction was presented in the work of Munoz et al. [182]. The inductance of the system was obtained through performing EIS measurements on a piece of gold. By subtracting the measured inductance from the impedance data of the electrochemical cell, the inductance-free EIS data could be obtained.

It has to be noted that although the importance of inductance correction has been realized and some approaches for the correction have been developed, the reported works are all carried out with button cells. In literature reporting about the EIS measurements with SOC stacks, the improvement of EIS data quality is achieved via optimization of cabling, which is difficult for commercial test rigs since the design varies with different suppliers [183, 184]. As discussed in the beginning of this chapter as well as in literature, the inductance error will become more significant when performing EIS measurement with stacks [181, 182]. Additionally, the signals from the built-in instruments in the large SOC test rigs (e.g. electric load and power supply) will also introduce electrical noise into the measured EIS data, which can further affect the DRT analysis. Therefore, the EIS data post-processing and the subsequent DRT calculation will be discussed in this work.

3. Experimental setup

3.1 Stack construction

The SOC stacks tested in this work were assembled in accordance with the JÜLICH F10 design. The overall area of each cell was 10 cm x 10 cm and the active area was about 80 cm^2. The stacks were constructed using Crofer 22 APU as the interconnector.

All cells were of the ASC (Anode-Supported Cell, in SOFC mode) type, which uses Ni-YSZ cermet as the fuel electrode substrate. 8YSZ (8 mol-% yttria-stabilized zirconia) was used as the electrolyte and two kinds of air electrode materials were used as the air electrode material: LSC and LSCF.

In order to reduce the Cr evaporation from the interconnector, an MCF (MnCo$_{1.9}$Fe$_{0.1}$O$_4$) protective layer was coated on the air side of the Crofer22 APU interconnectors. Between the air electrode and the interconnector, a perovskite powder (LCC10, manufactured by Jülich) was wet powder-sprayed (WPS) on the interconnector as a contact layer. A GDC (Ce$_{0.8}$Gd$_{0.2}$O$_{1.9}$) barrier layer was deposited between 8YSZ electrolyte and air electrode either by PVD or screen printing. On the fuel side of the interconnector, a Nickel-mesh was welded as the electrical contact and gas distributor. The schematic drawing of the stack construction could be seen in **Figure 2.3** and more detailed information about the ASC technology and the JÜLICH F10 stack design can be found elsewhere in the literatures [185-188].

3.2 Stack test rig

Most of the stack tests were performed with the SOFC/SOEC combination test bench (MP30) from the EBZ GmbH. **Figure 3.1** shows one of the tested SOC stacks mounted in the EBZ test bench.
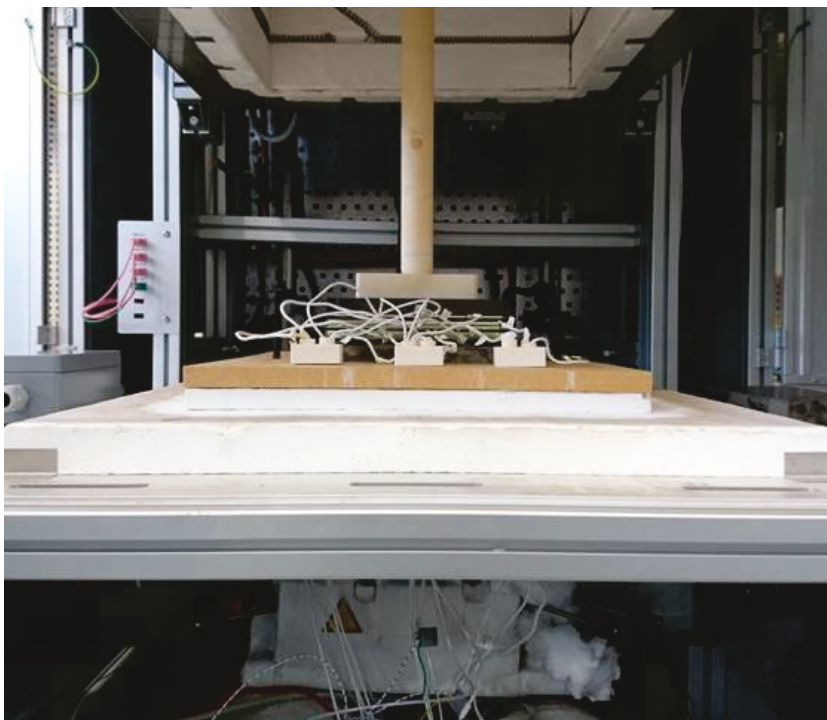
Figure 3.1: SOC stack F1004-87 mounted in MP30.

The test bench can be controlled through the graphical user interface (GUI) of the EBZ software. The flow diagram of the GUI is shown in **Figure 3.2**.
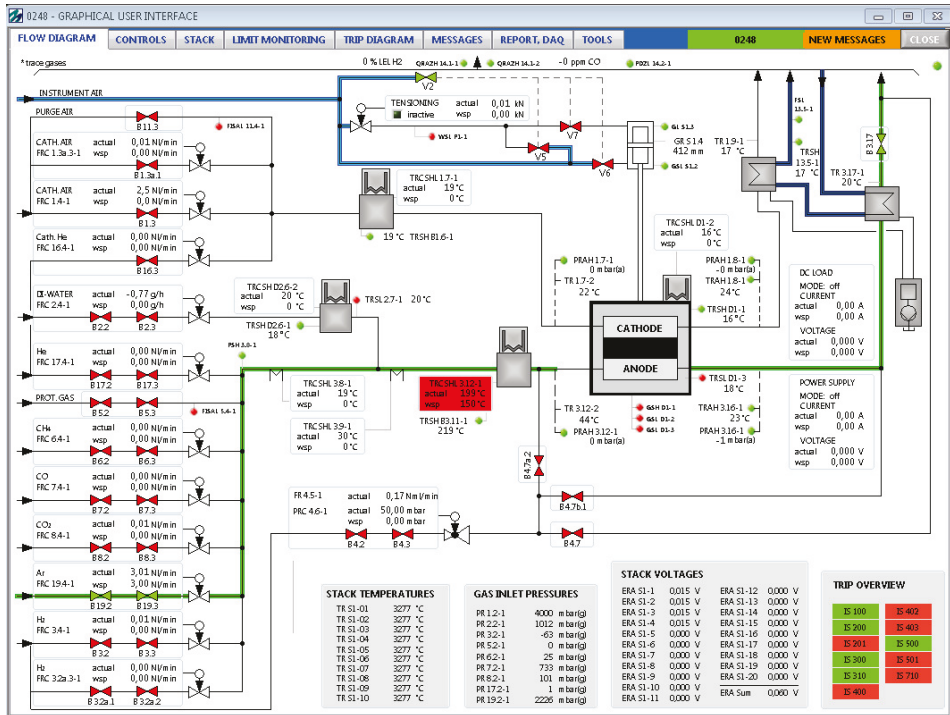
Figure 3.2: The flow diagram of MP30.

As the flow diagram shows, the gas supply in MP30 is controlled by individual mass flow controls (MFCs). The parameters of some MFCs are listed in **Table 3.1**.

Table 3.1: Technic parameters of the MFCs in MP30.

Gas	Calibration pressure	Flow rate
Cathode air	2.0 bar	0.5 – 250 Nl/min
Deionized water	2.0 bar	24 – 1200 g/h
Hydrogen	2.0 bar	0.06 – 25 Nl/min
Protective gas (4 % H_2 + 96 % Ar)	2.0 bar	4 – 20 Nl/min
Argon	2.0 bar	2 – 20 Nl/min

With MP30, it's possible to operate the stack under SOFC and SOEC modes. For the SOFC operation, an electronic load from the EA Elektro-Automatik GmbH with the model number EA-EL9080-200HP was pre-installed in the test bench, and a power supply unit also from EA with the model number EA-PSI-8040-170-3U was installed for the SOEC operation. The major technical parameters of the electronic load and the power supply unit can be found in **Table 3.2**.

Table 3.2: Technic parameters of electronic load and the power supply unit in MP30.

Parameters	Electronic load	Power supply
Working temperature	0 – 50 °C	0 – 50 °C
Operating modes	Current, Voltage	Current, Voltage
Electrical connection	230 V / 50 Hz	400 V / 50 Hz
Voltage setting range	0 – 80 V (DC)	0 – 40 V (DC)
Control Accuracy	≤ 0.1 % of nominal value	≤ 0.2 % of nominal value
Power setting range	0 – 2400 W	0 – 3300 W
Control Accuracy	≤ 2 % of nominal value	≤ 2 % of nominal value
Current setting range	0 – 200 A (DC)	0 – 170 A (DC)
Control Accuracy	≤ 0.2 % of nominal value	≤ 0.2 % of nominal value

3.3 EIS set-up and DRT calculation

The EIS measurements were carried out using the Zahner IM6 electrochemical workstation with an external potentiostat PP211. Four PAD4 add-on cards were installed with IM6, which enables the parallel EIS tests up to sixteen channels.

Figure 3.3: The Zahner EIS system (From up to down: PP211, IM6 and EL1000).

The whole system was controlled by the Zahner Thales software. EIS measurements were performed over the frequency range from 100 kHz to 0.1 Hz, with 12 points per decade. Galvanostatic mode was used for the measurements with a DC offset of ±5 A (SOFC: +5 A; SOEC: -5 A), and an AC current of 2 A. The major technic parameters of PP211 and IM6 are listed in **Table 3.3**.

Table 3.3: Technic parameters of PP211 and IM6

Parameters	PP211	IM6 / (with U-buffer)
Potential range	±20 V	±4 V / (±10 V)
Potential accuracy	±2 mV	±250 µV / (±1 mV)
Current range	±10 A	±3 A
Current accuracy	±0.25 %	0.1 %: ⩾ 2 µA to 100 mA 1.0 %: < 2 µA or > 100 mA
Frequency range	10 µHz ~ 200 kHz	10 µHz ~ 8 MHz
Impedance range	1µ Ω ~ 1 kΩ	1 mΩ to 1 GΩ / 2% 100 mΩ to 10 MΩ / 0.2%

The DRT results were calculated from the impedance data with the DRTTOOLS, a Matlab toolbox developed by the Hong Kong University of Science and Technology. The DRT is estimated based on RBFs (Radial Basis Functions) discretization in DRTTOOLS and the detailed information about DRTTOOLS can be found in the literatures [189-191].

4. Results and discussion

4.1 The influence from the test rig during EIS measurements

As discussed in **Chapter 2.3.4**, the EIS measurement is very sensitive and the data quality is easily influenced by the electronic noise. The complex stack test rig is one of the main sources of the noises. The un-optimized cable for EIS measurement may result in very high inductance in the obtained EIS data which can influence the further analysis such as DRT. Moreover, the noise from the external electric devices in the test rig may also make it difficult to obtain EIS data of high quality.

4.1.1 Inductance of the test rig

The inductive signal is unavoidable during the EIS measurements and it is mainly introduced from the EIS setup itself such as the cable inductance and mutual inductance. Therefore, the inductive part in the EIS data provides no information about the stack. More importantly, the inductive element affects the analysis of the EIS data. **Figure 4.1** shows an artificial equivalent circuit simulated in ZView, which contains an inductive element L_0, a pure resistor R_0 and five RC elements in series connection. L_0 varies from 0 H to 1E-9 H, and the respective Nyquist and Bode plots are shown below.
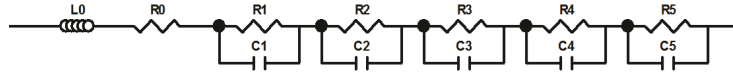
L0	R0	R1 ~ R5	C1	C2	C3	C4	C5
0 ~ 1E-9 H	1E-3 Ohm	1E-4 Ohm	0.03185 F	0.3185 F	3.185 F	31.85 F	318.5 F
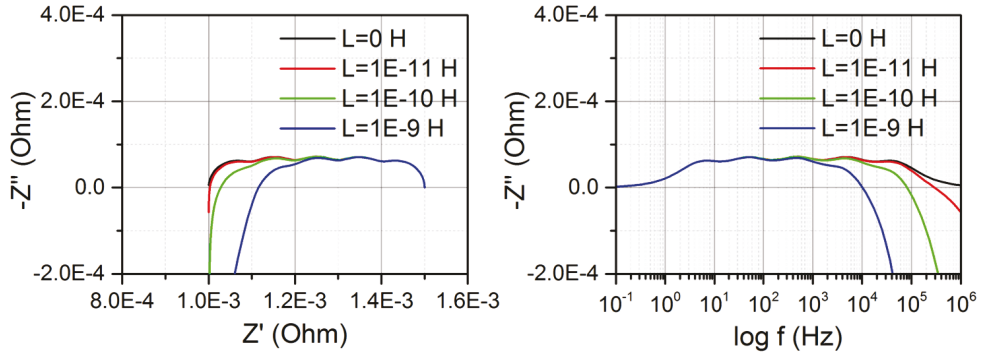
Figure 4.1: The Nyquist and Bode plot of the L_0+R_0+5RC equivalent circuit with different inductance values.

The ohmic resistance R_0 of the equivalent circuit should be identical to the impedance value of intersection between the real axis and the Nyquist curve at the high frequency side. For the equivalent circuit in **Figure 4.1**, R_0 was set constant as 1E-3 ohm and the Nyquist curve with no inductance (L = 0 H) shows the same value. With increasing inductance, the Nyquist curves show increasing length of the high frequency 'tail' in the negative Z'' part. Meanwhile, the "ohmic resistance" is observed increasing.

In the Bode plot, five peaks are observed when L = 0 H. With increasing inductance, the high frequency 'tail' becomes more significant and the high frequency peaks shifts towards low frequency. When L_0 increases to 1E-9 H, the peak at the highest frequency side disappears and the Bode plot shows only four peaks.

As discussed above, the inductive signal affects the determination of the real ohmic resistance R_0 in the equivalent circuit. Additionally, the number of peaks in the Bode plot can help to determine the number of RC elements used in the equivalent circuit. With increasing inductance, the high frequency Bode peak shifts to lower frequency side and

even disappears with large inductance. Therefore, the inductive signal will possibly mislead the building of the correct equivalent circuit in the analysis of the EIS data.

Figure 4.2 shows the DRT results calculated from the EIS data with different L_0 values from Figure 4.1. For the equivalent circuit with no inductance, five DRT peaks could be identified, which is in accordance with the number of RC elements used in the circuit. With increasing inductance, the first DRT peak at the highest frequency (~50 kHz) becomes sharp and shifts to lower frequency. This peak disappears when the inductance is increased to 1E-9 H. Meanwhile, the height of the second peak at the frequency of about 5 kHz decreases and also shifts to the lower frequency side.
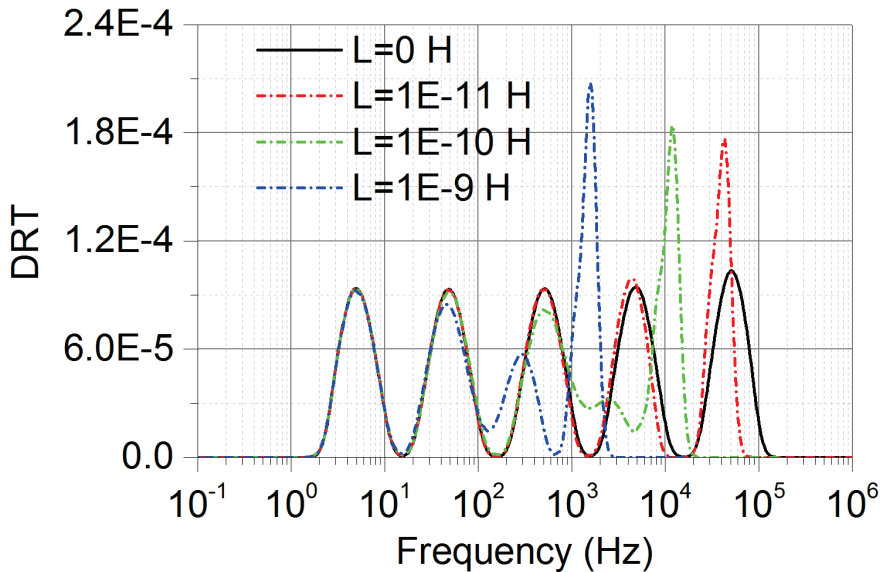
Figure 4.2: DRT results of the EIS data from Figure 4.1.

It has been proved that the "unwanted" inductance in the circuit will mislead the determination of the real ohmic resistance from the Nyquist plot. The Bode peaks and DRT peaks especially at the high frequency side are significantly affected by the inductance, which further makes it difficult to build a reliable equivalent circuit model

during the analysis of the EIS data. The correction of inductance with the raw EIS experimental data becomes necessary.

4.1.2 Influence from the electrical circuit

The test rig used here does not have integrated impedance spectrometer. The Zahner system has to be connected to the stack through extra connections for EIS measurement. **Figure 4.3** shows the schematic connections between the stack, the built-in electronic devices and EIS system.
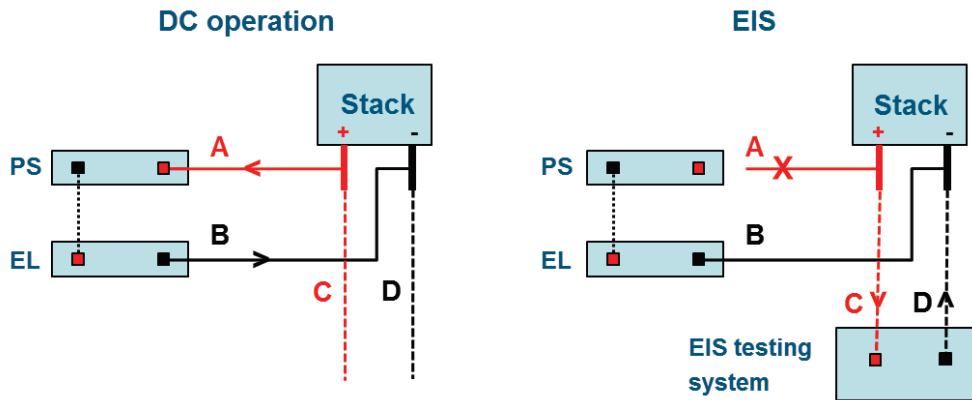
Figure 4.3: Connection between the stack, power supply, electric load and EIS system

As **Figure 4.3a** shows, the stack is in series connected with power supply (PS) and electric load (EL) of the test rig through cable A and B for standard DC characterization and operation. For conducting EIS measurements, the EIS testing system is directly connected to the stack through cable C and D. The power supply and electric load of the test rig need to be disconnected from the stack to avoid the measurement failure, even the devices generally already have high input impedance

In order to study the possible influence from the built-in Power supply and Electric load, experiments were designed during the background EIS measurements with the test bench MP28. Similar background impedance measurement for the inductance correction

has been reported, in which the EIS measurement was conducted on pure platinum in the test rig [182]. During the background EIS measurements in this work, the current collectors of the test bench were directly connected with a metallic interconnector instead of a stack, so that the background EIS signal which should only show ohmic and inductive parts can be obtained. The built-in Power supply and Electric load were set to three conditions: 1) both were connected and power on, 2) both were connected but power off and 3) both were disconnected physically from the EIS testing circuit. The respective EIS results are shown in **Figure 4.4**.
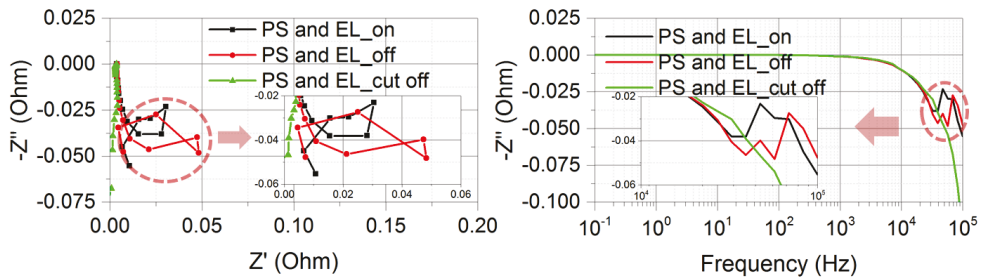
Figure 4.4: Nyquist and Bode plots when the power supply (PS) and electric load (EL) are "on", "off" and "cut off".

The Nyquist curve measured with PS and EL disconnected is a nearly straight line perpendicular to the real axis, which shows ohmic and inductive behavior as expect. However, in the Nyquist curve measured either with PS and EL on or off, a high frequency loop is observed. This high frequency noise is also shown in the Bode curves in the Bode plot. As **Figure 4.4b** shows, the noise signal is observed in the frequency range > 30 kHz.

The influence of the external Power supply and Electric load on the EIS data has been proved in the background EIS measurements. In order to remove such high frequency noise, a switch was installed in the test bench MP31, which enables the switch between the circuit for DC measurement and EIS measurements. **Figure 4.5** is the schematic showing how the switch functions.
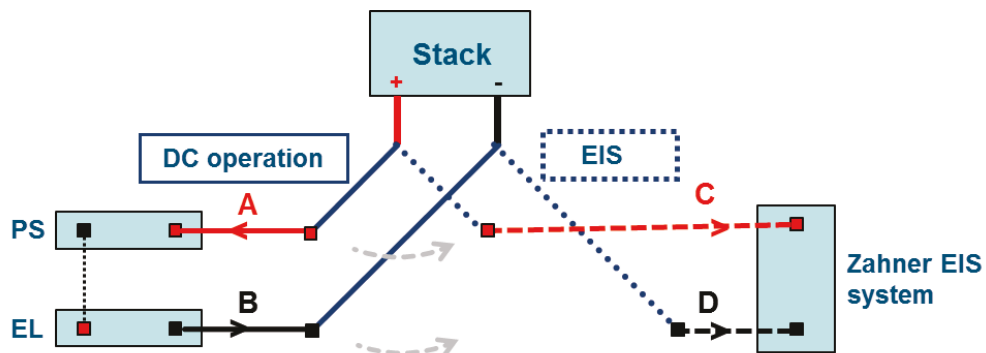
Figure 4.5: The switch between IV-curve and EIS measurements in MP28.

As **Figure 4.5** shows, the connection between the stack and the external Power supply/ Electric load can be cut off by the switch while performing EIS measurements. To prove the effect of the switch in the real stack tests, EIS measurements were performed with a SOFC short stack F1005-06 in the test bench MP31. **Figure 4.6** shows the EIS results of cell 3 obtained with and without the switch.
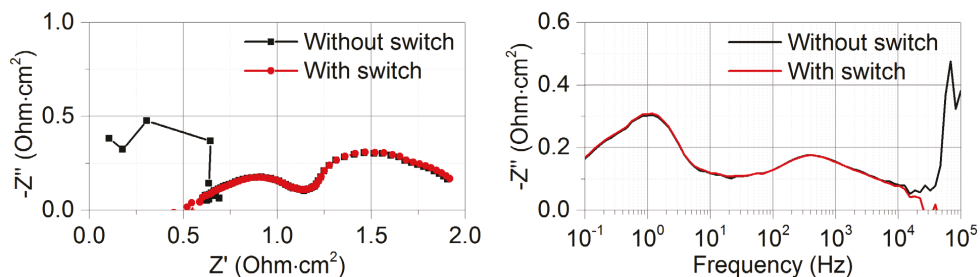
Figure 4.6: EIS results obtained with and without the switch in MP31.

Nearly no difference can be observed between the two curves in the Nyquist and Bode plot at frequencies < 20 kHz, while high frequency noise can be observed in the Nyquist curve measured without the switch and the bode plot indicates that the noise become significant in the frequency range > 20 kHz. From the Nyquist plot, the noise

signal shows capacitive behavior, which is possibly due to the capacitive elements in the built-in Power supply or the Electric load.

The effect of the switch on reducing the noise signal observed at high frequency from the EIS data has been proved. Therefore, it is highly recommended that this switch should be installed in all the SOC test rigs.

4.2 EIS data post-processing

It has been proved that the reliability of the DRT technology is highly dependent on the respective EIS data quality. The improvement of the EIS data quality can be achieved through the optimization of EIS measurements in test rigs. Moreover, the post-processing of the EIS data is also of great importance.

4.2.1 Inductance correction

During the stack tests with different test benches, it has been observed that there are significant differences about the inductance conditions between different test benches. Since stacks are usually transferred from one test bench to another during the testing, the difference of the inductance conditions between test benches will make the EIS data from different test benches not comparable. Therefore, the inductance correction is very necessary especially for the EIS data of one stack but obtained from different test benches.

The stack F1004-87 was first tested in the test bench MP06 for about 1200 hours and then transferred to the test bench MP30 for further testing. Before cooling in MP06 and after the restart in MP30, IV curve measurements were performed with this stack at the same conditions (700 °C with 20% humidified H_2). The measured IV curves at different test benches are shown in **Figure 4.7**.
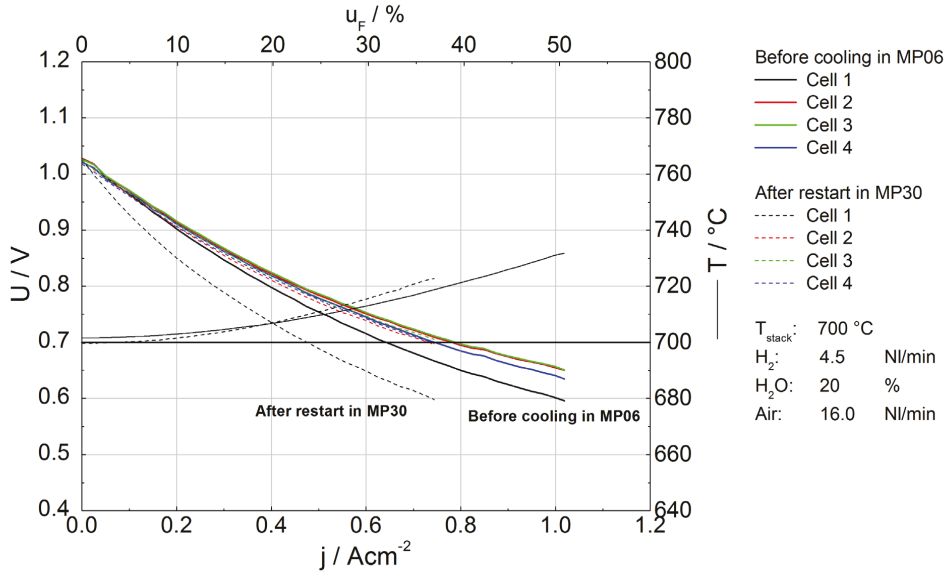
Figure 4.7: IV curves of F1004-87 before cooling in MP06 (KL40) and after changing to MP30 (KL41).

A large degradation of cell 1 can be observed after changing the test bench, most probably due to the contact loss in this layer, caused by the bended adapter plate in MP06. The performances of other three cells were kept nearly constant without obvious degradation after changing the test bench. EIS measurements were conducted after IV curve measurements. The system or background inductance signal of MP30 has been observed much stronger in previous EIS measurements. In order to investigate the influence of the background inductance signals from different test benches on the EIS and DRT analysis, the EIS data of an undegraded cell (cell 4) obtained from different test benches are of great interest. As **Figure 4.8** shows, EIS39 was conducted before cooling in MP06, while EIS41 was conducted after changing to MP30.
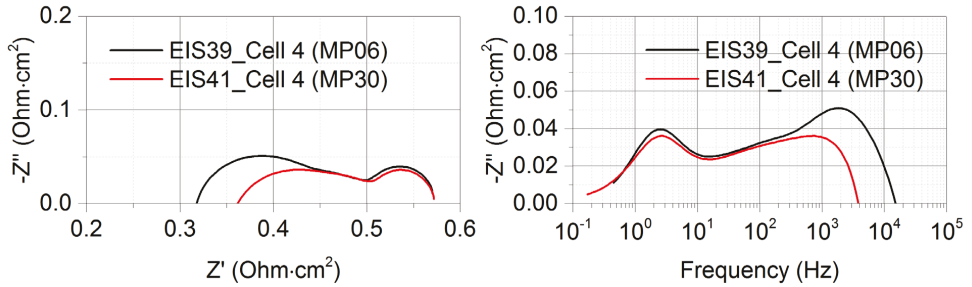
Figure 4.8: EIS results of Cell 4 from F1004-87 obtained before cooling in MP06 (EIS39) and after changing to MP30 (EIS41).

It has been proved by the IV curves in **Figure 4.7** that there was nearly no degradation of cell 4 after changing test benches. However, from the Nyquist plots, higher "ohmic" resistance but identical total impedance was observed for cell 4 after changing the test bench. Under the assumption that there was no change in the cell performance, the reasonable explanation for this phenomenon is the higher background inductance in MP30 which could shift the high frequency intersection to the right side (higher ohmic resistance) while there would be nearly no influence in the middle or low frequency (identical overall impedance). The influence of higher inductance was further investigated with DRT, which is shown in **Figure 4.9**.
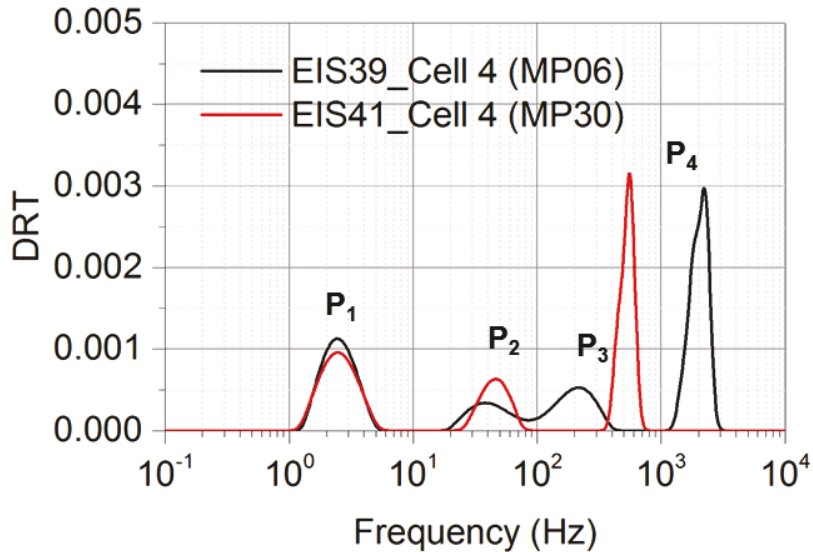
Figure 4.9: DRT plots of Cell 4 from F1004-87 before cooling in MP06 (EIS39) and after changing to MP30 (EIS41).

Four peaks could be observed in the DRT plot for cell 4 tested in MP06. In MP30, the high frequency peak P_4 showed an obvious shift to lower frequency, which fits what was observed in the Bode plots in **Figure 4.8**. Additionally, P_3 disappeared in the DRT plots in MP30, which has been proved due to the influence from the high inductance by the simulated results in **Chapter 4.1.1**.

The background impedance test has already been performed in MP30 with the current collectors connected by the Crofer22 APU connectors. Through the modelling in ZView, the inductive part in the background impedance of MP30 was determined as L = 2.6E-8 H and the inductive reactance can be calculated as the following equation:

$$X_L = 2\pi f L$$

Since the inductance only has imaginary part, the inductance correction with the measured raw impedance Z_{raw} to get the corrected impedance Z_{corr} can be done as following:

$$Z_{raw} = Z_{Re} + jZ_{Im}$$
$$Z_{corr} = Z_{raw} - jX_L = Z_{Re} + j(Z_{Im} - X_L)$$

Figure 4.10 shows the comparison between the raw EIS data measured in MP30 (EIS41) and the corrected data.
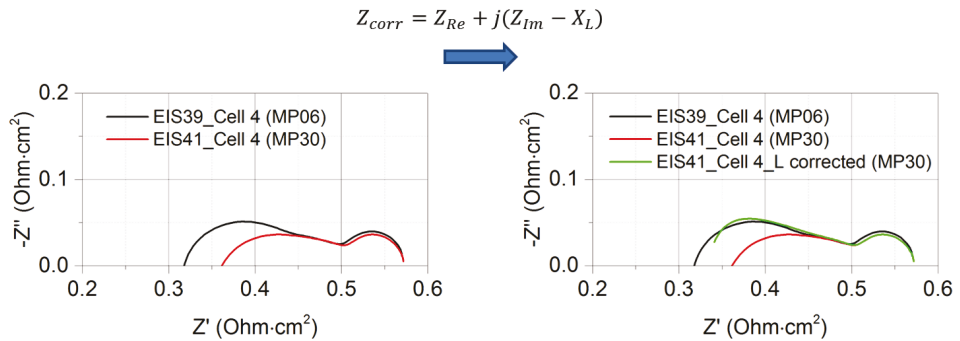
Figure 4.10: Raw and corrected EIS data (EIS41) of Cell 4 from F1004-87 in MP30.

Although the background impedance measurement hasn't been performed with MP06, the Nyquist curves of the EIS results of the stack tests in MP06 always show very short high frequency tail, indicating that the background inductance of MP06 can be neglected.

After the inductance correction, the low frequency part is not influenced but the high frequency part of the corrected Nyquist curve nearly overlaps with that from EIS39, indicating that the performance of cell 4 did not degrade after changing test benches which corresponds with the observation from the IV curves in **Figure 4.7**.

The DRT calculation was conducted with the corrected EIS data and the DRT curve is shown in **Figure 4.11**.

$$Z_{corr} = Z_{Re} + j(Z_{Im} - X_L)$$
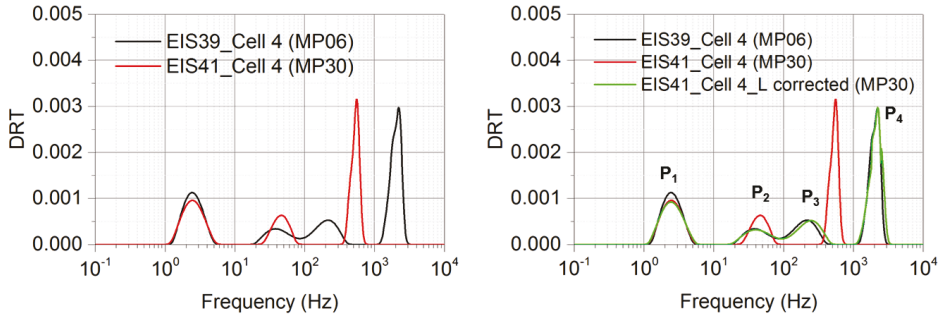
Figure 4.11: DRT plots of raw and corrected EIS data (EIS41) of Cell 4 from F1004-87 in MP30.

Four peaks can be identified from the DRT curve calculated of the corrected EIS data, which show almost the same peak and characteristic frequencies as those of EIS39. Through the inductance correction, the problems introduced by the high inductance such as the frequency shift of the high frequency peak and the loss of small peak at intermediate frequencies can be effectively solved, which makes the analysis with EIS and DRT more reliable.

4.2.2 Logarithmic Hilbert Transformation

The EIS has been proved as a very powerful tool for analyzing the electrochemical systems under steady conditions. In practice, the steady conditions are usually violated due to the time instabilities of the system such as the unstable steam supply to the stack. The EIS measurement is very sensitive to the environment. As results, it is easy to observe messy points in the EIS data in the real measurement. Since the DRT result is

calculated from the EIS data, the reliability of the DRT result is influenced by the EIS data quality.

In order to study the influence of the EIS data quality on the DRT calculation, an artificial equivalent circuit containing three RC elements in series connection was built as shown in **Figure 4.12**. Through manually changing the impedance values of the simulated EIS data points, some artefacts were randomly added into the simulated perfect EIS data in the low frequency range (< 10 Hz). The Nyquist and Bode plots of the perfect simulated EIS data and the modified one can be seen in **Figure 4.12**.

R0	R1 ~ R3	C1	C2	C3
0.01 Ohm	1 Ohm	0.1 F	0.01 F	0.001 F
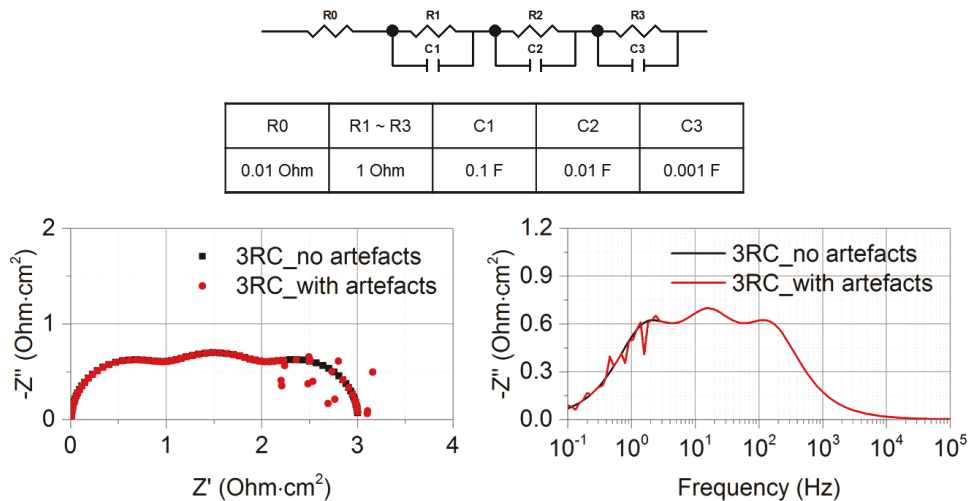
Figure 4.12: Nyquist and Bode plots of the simulated EIS data and the data with artefacts.

Three arcs can be observed in the Nyquist plot of the simulated EIS data, corresponding to the three Bode peaks in the Bode plot. The artefacts can be seen clearly in the low frequency range in the Nyquist and Bode plots. With the same parameters during the DRT calculation, **Figure 4.13** shows the DRT plots calculated from the EIS data in **Figure 4.12**.
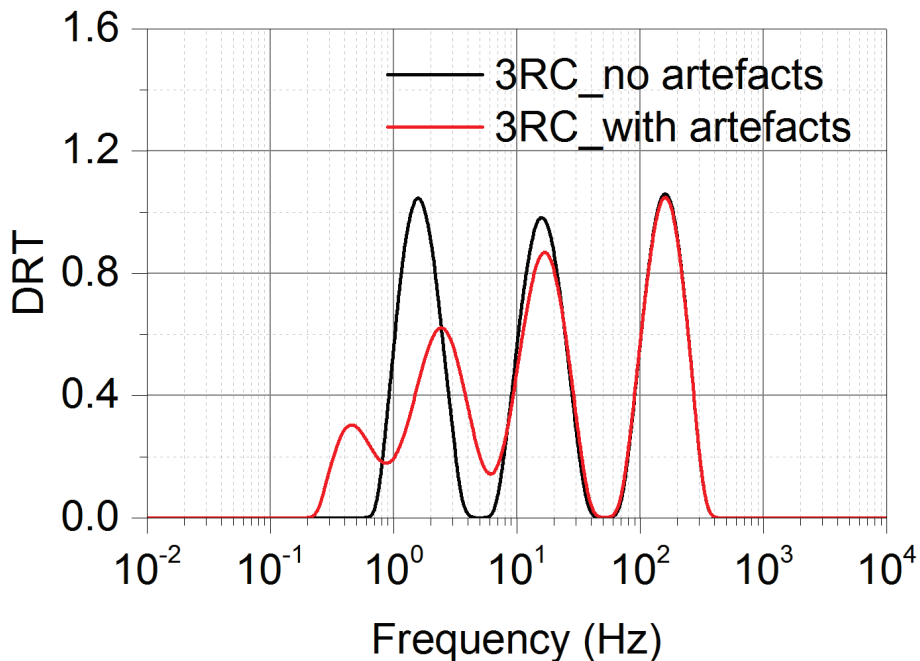
Figure 4.13: DRT plots of the EIS data from **Figure 4.12**.

Three DRT peaks can be observed from the DRT plot of the simulated EIS data with no artefacts. However, the DRT plot of the EIS data with artefacts shows two DRT peaks with smaller peak height in the low frequency range (< 10 Hz). The additional peak and the change of peak height appear in the frequency range where the artefacts are located. This result proves that the poor EIS data quality can possibly results in the artificial DRT peaks in the calculated DRT plot.

Practically, it is very often to observe that EIS data showing similar 'artefacts' in the low frequency range during the SOC stack test especially when the stack is supplied with humidified hydrogen, indicating that the problem is mainly due to the unstable steam supply from the test rig. According to the Nernst equations, the unstable steam partial pressure in the fed gas will lead to the cell voltage fluctuation during the impedance measurement, resulting in the mistakes and errors in the impedance calculating.

One possible way to solve this problem is to increase the temperature of the evaporator and the related pipelines, so that the steam condensation can be reduced and more stable steam supply to the stack can be expected. However, the water flow rate is normally set between 30 g/h and 200 g/h during the stack operation, which is almost near the lower limit in the operation range of the mass flow control (e.g. 24 g/h ~ 1200 g/h in MP30). It is difficult for the mass flow control to precisely control the water flow to the evaporator in this operation range, so that the water and steam supply to the stack will be unstable. That is why the data quality of the EIS measurement performed with higher water content is always better than that with lower water content in the same test bench.

From the perspective of performing EIS measurements, one way to increase the data quality is to increase the "measure periods" while setting the EIS parameters at the low frequency limit. This parameter defines how many sine cycles are to be averaged for one measurement point. With more sine cycles are averaged, the influence form the time instabilities of the system on the EIS data recording is reduced so that better EIS data quality can be expected. However, increasing this parameter especially at the low frequency limit would lead to significantly longer measuring time.

Another way to improve the data quality is to validate and re-calculate the measured EIS data with Hilbert transformation (HIT). The Hilbert transformation functions similar as the famous Kramers-Kronig (KK) transformation, which can be used to check the impedance results with respect to causality and stability. Compared with the KK techniques, a modified logarithmic Hilbert transformation was developed, which has overcome the "limited bandwidth problem" and can be used to re-calculate the EIS data [192]. The HIT technique functions according to the following empirical approximation:

$$\ln|H(\omega_0)| \approx const. + \frac{2}{\pi} \int_0^{\omega_0} \varphi(\omega) d\ln\omega + \gamma \frac{d\varphi(\omega)}{d\ln\omega}$$

The fundamental principles of the equation will not be discussed in this work, since my work is to prove if this transformation can effectively correct the artefacts in the measured EIS data and improve the data quality for further DRT analysis. For this purpose, a set of EIS data from a SOC stack (F1004-82) was selected for the

re-calculation with the HIT technique and the data re-calculation was conducted with a built-in function from the Zahner Thales software. The Nyquist and Bode plots of the original and re-calculated EIS data can be seen in **Figure 4.14**.
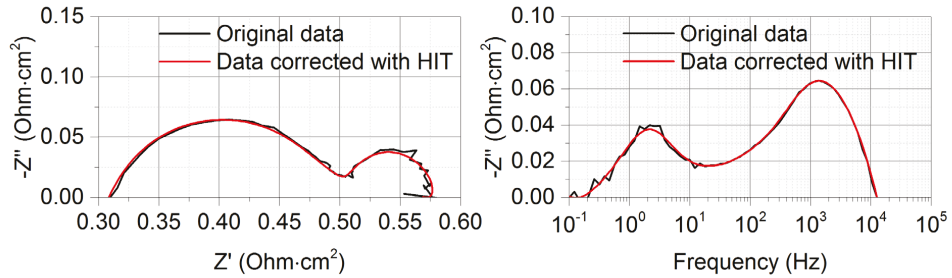
Figure 4.14: Nyquist and Bode plots of the original EIS data and the data re-calculated with HIT.

The original EIS data were measured with 20% H_2O+80% H_2 as the fuel gas. As **Figure 4.14** shows, the original data show poor quality in the low frequency range (< 10Hz) and this is the most typical phenomenon observed in the EIS data when measured with unstable steam supply. After re-calculation with the HIT technique, the low frequency noises are effectively removed. The Nyquist and Bode curves are much smoother than the curves before. The DRT results calculated from the EIS data from **Figure 4.14** are shown in **Figure 4.15**.
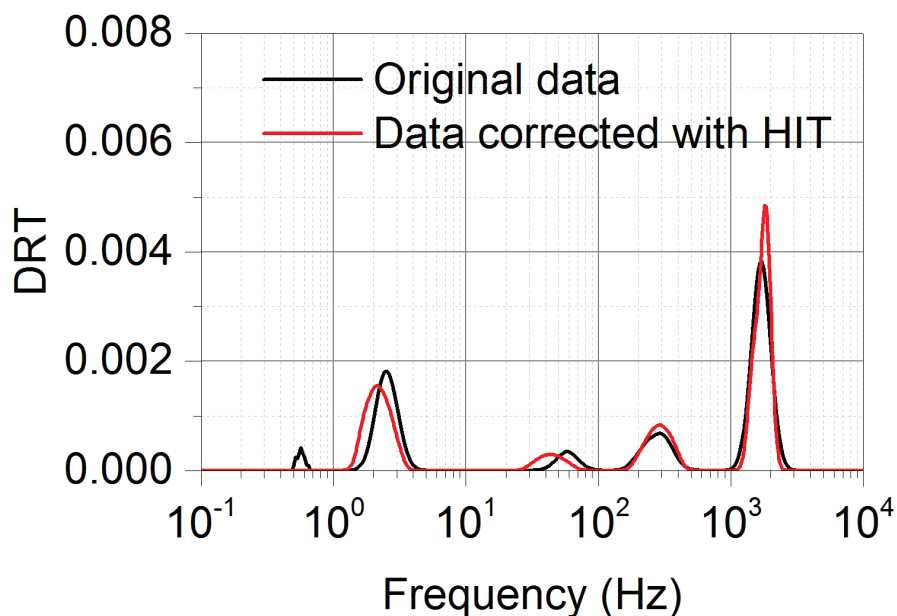
Figure 4.15: DRT plots of the EIS data from **Figure 4.14**.

Four major DRT peaks can be identified at the frequency range between 1 Hz ~ 10 kHz for both DRT curves, indicating that the HIT correction will not create artificial peaks. However, for the DRT curve of the original data without the HIT correction, one additional peak evolves at ~0.6 Hz with low peak height and narrow frequency range. The characteristic frequency of this peak matches well with the frequency in the Bode plot (**Figure 4.14**) where the noisy signal mainly locates at. Additionally, with the information from literature and our own results, it is recognized that there should be no peak in this frequency range (0.1 Hz ~ 1 Hz) under normal operation conditions (sufficient gas supply) [18, 20]. Therefore, it is reasonable to believe that the peak observed at ~0.6 Hz is generated due to the noisy signal in the original EIS data. By the HIT correction, the artificial DRT peak can be removed.

The inductance from the test bench and the noisy signals during the EIS measurements with SOC stacks have been proved to impact the DRT analysis, which can create artificial DRT peaks and result in unreliable DRT results. The EIS data post-processing, including the inductance correction and the HIT correction, can effectively remove such negative influences from the EIS data and ensure the reliability of the DRT results.

4.3 DRT peaks identification with SOC stacks

Before applying the DRT to the study of SOC stacks, it is necessary to distinguish the DRT peaks with overlapped electrochemical processes in the SOC stack. This can be achieved only through the parameter study experiments, in which a series of EIS measurements are performed with different operation parameters such as stack temperature and gas composition. Similar tests have been conducted with SOFC single cells [20]. However, systematic tests with SOFC stacks were not reported.

In this work, the parameter study test was mainly performed with a four-cell stack F1004-72 with LSC air electrode and a testing matrix with varying operation parameters was designed. Impedance measurements were performed at OCV conditions with DC offset (±5 A) and AC current of 2 A. In the following sections the parameter dependency of the DRT peaks will be discussed.

4.3.1 Air

The gas supplied at the air electrode side is dry air with constant oxygen partial pressure (0.21). In order to study the oxygen dependency of DRT, the air flow rate was adjusted as shown in **Table 4.1**.

Table 4.1: Operation parameters for the parameter study of air.

	T (°C)	H_2 (Nl/min)		Ar (Nl/min)		H_2O (Nl/min)		Air (Nl/min)	λ (7A)
Air	700	4.5	50.00%	0	0.00%	4.5	50.00%	16	34.44
	700	4.5	50.00%	0	0.00%	4.5	50.00%	1.4	3.01
	700	4.5	50.00%	0	0.00%	4.5	50.00%	0.7	1.51

The air flow rate was adjusted from 16 Nl/min to 0.7 Nl/min, which correspond to the air lambda from 34.44 to 1.51 calculated with 7 A as the EIS current. **Figure 4.16** shows the Nyquist and Bode plot of the EIS data obtained with different air flow rate.
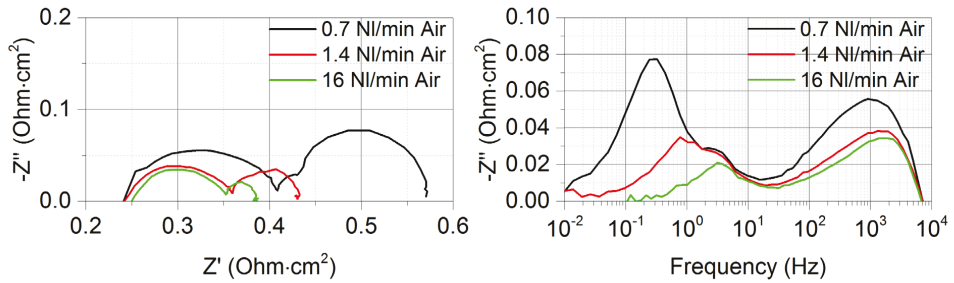
Figure 4.16: Nyquist and Bode plots obtained with different air flow rates.

It can be observed from **Figure 4.16** that a new process evolves in the frequency range below 3 Hz when the lambda is reduced below 3. Since the processes at low frequencies in SOC are mostly related to the gas diffusion, this process which is pronounced with insufficient air supply should be attributed to the oxygen diffusion at the air electrode. The minor increase of the ohmic resistance with increased air flow rate observed in the Nyquist plot can be due to the cooling effect of air.

Figure 4.17 shows the DRT results calculated with the EIS data in **Figure 4.16**, indicating the air flow rate dependence of DRT.
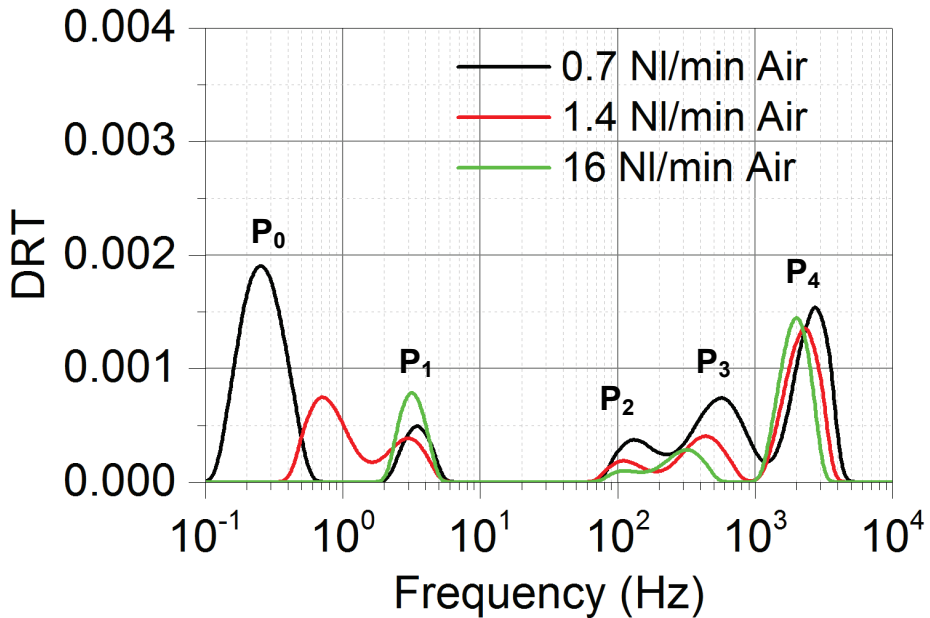
Figure 4.17: DRT plots obtained with different air flow rates.

At least four DRT peaks can be identified with sufficient air supply, while the new evolved process observed in the Nyquist and Bode plots in **Figure 4.16** should be related to the DRT peak (P_0) which is only observed at the frequency below 2 Hz when the air flow rate decreases below 1.4 Nl/min, and this peak shows larger peak height as well as shifts to low frequency side with decreased air flow rate.

When the stack is supplied with excessive oxygen supply (e.g. λ = 34.44), the resistance of the air diffusion process at the air electrode can be ignored. Only with insufficient oxygen supply, the resistance of the air diffusion process will become pronounced and contribute to the overall resistance. The frequency shift of P_0 also indicates that this peak may be overlapped with P_1 when the oxygen supply is sufficient. The gas diffusion process at the air electrode can be described with the following equation [18, 193]:

$$R_{conc,\ cat} = \left(\frac{RT}{4F}\right)^2 L_{cat} \frac{1}{D_{mol,\ O_2}} \frac{1}{\Psi_{cat} P_0} \left(\frac{1}{\boldsymbol{pO_{2,\ cat}}} - 1\right)$$

Where L_{cat} is the air electrode thickness; $D_{mol,\ O_2}$ is the effective diffusion coefficient of oxygen; Ψ_{cat} is the parameter related to the air electrode structure and P_0 is the absolute atmospheric pressure.

When all the parameters except the oxygen partial pressure at the air electrode are kept constant, the equation above can be simplified into:

$$R_{conc,\ cat} = \frac{C}{\boldsymbol{pO_{2,\ cat}}} - C$$

Figure 4.18 shows the relationship between the gas diffusion resistance and the oxygen partial pressure at air electrode plotted according to the simplified equation.
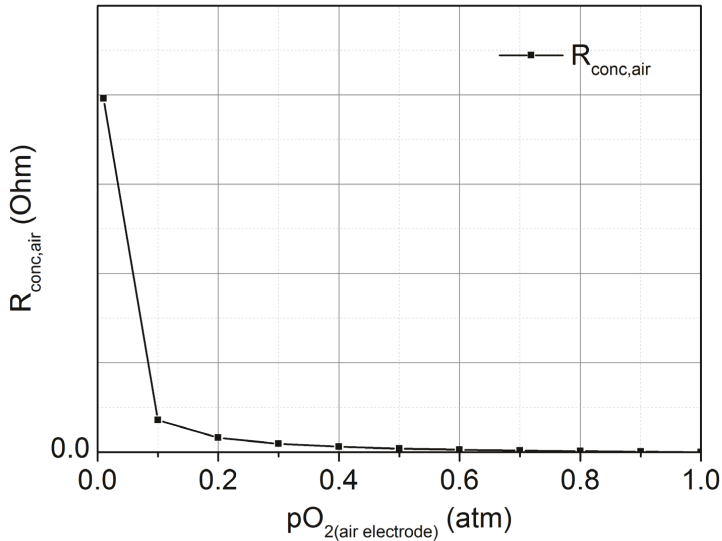
Figure 4.18: Oxygen partial pressure dependency of the gas diffusion resistance at air electrode.

The peak height increase indicates that the resistance of the related electrochemical process becomes larger, while the shift of peak position is related to the change of the characteristic frequency of the related process. It can be seen clearly from **Figure 4.18** that the gas diffusion resistance at the air electrode can be significantly high when the oxygen partial pressure drops below 0.1 atm. For the gases with oxygen partial pressure higher than 0.2 ($pO_2 = 0.21$ in air), the gas diffusion resistance can be ignored. Due to the limit of the test rig, the depletion of oxygen at air electrode side was achieved by reducing the air flow rate instead of reducing the oxygen partial pressure in air. However, the evolution of the DRT peak P_0 still matches well with the results from **Figure 4.18**.

P_4 located at the frequency range of 1 kHz ~ 5 kHz keeps nearly constant with changing air flow rates, which makes it a fuel electrode related process. Apart from P_0, P_2 and P_3 also decrease with increased air supply, indicating that these two peaks should also be related to air electrode processes. The definition of P_2 and P_3 should be combined with other parameter study tests.

4.3.2 Hydrogen

During the parameter study experiments about the hydrogen partial pressure, the fuel gas supplied at the fuel electrode side is the mixture of H_2, H_2O and Ar. As **Table 4.2** shows, the partial pressure of water was kept constant of 30% while the partial pressure of hydrogen varied from 10% to 70%. The Argon was used to balance the total flow rate. The air flow rate was kept constant of 16Nl/min and all EIS measurements were performed at 700 °C.

Table 4.2: Operation parameters for the parameter study of hydrogen.

	T (°C)	H$_2$ (Nl/min)		Ar (Nl/min)		H$_2$O (Nl/min)		Air (Nl/min)	λ (7A)
H$_2$	700	1.5	10.00%	9	60.00%	4.5	30.00%	16	34.44
	700	4.5	30.00%	6	40.00%	4.5	30.00%	16	34.44
	700	7.5	50.00%	3	20.00%	4.5	30.00%	16	34.44
	700	10.5	70.00%	0	0.00%	4.5	30.00%	16	34.44

Figure 4.19 shows the Nyquist and Bode plot of the EIS data obtained with different Hydrogen partial pressure.
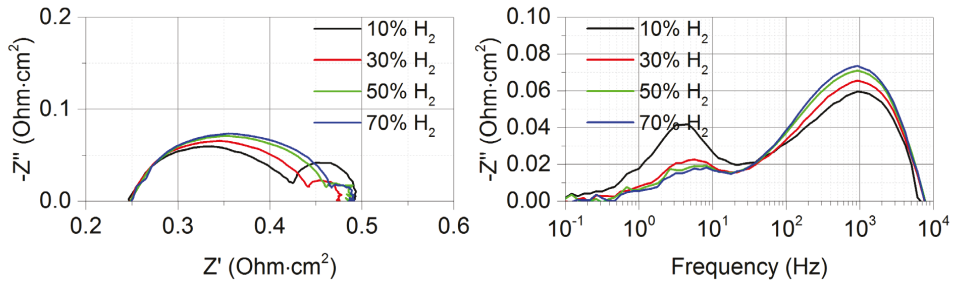
Figure 4.19: Nyquist and Bode plots obtained with different hydrogen partial pressure.

Two arcs can be identified in the Nyquist curves with different hydrogen partial pressure. With increased hydrogen partial pressure, the high frequency arc (~1 kHz from Bode plot) expands while the low frequency arc (~5 Hz from Bode plot) shrinks. Since the high frequency arc is always related to the charge transfer process and the low frequency arc is related to the gas diffusion process, the evolution of these two arcs indicates that, with increased hydrogen partial pressure, the resistance for the hydrogen diffusion process decreases while the charge transfer resistance related to hydrogen increases.

The DRT results calculated from the EIS data in **Figure 4.19** are shown in **Figure 4.20**, indicating the hydrogen partial pressure dependence of the DRT results.
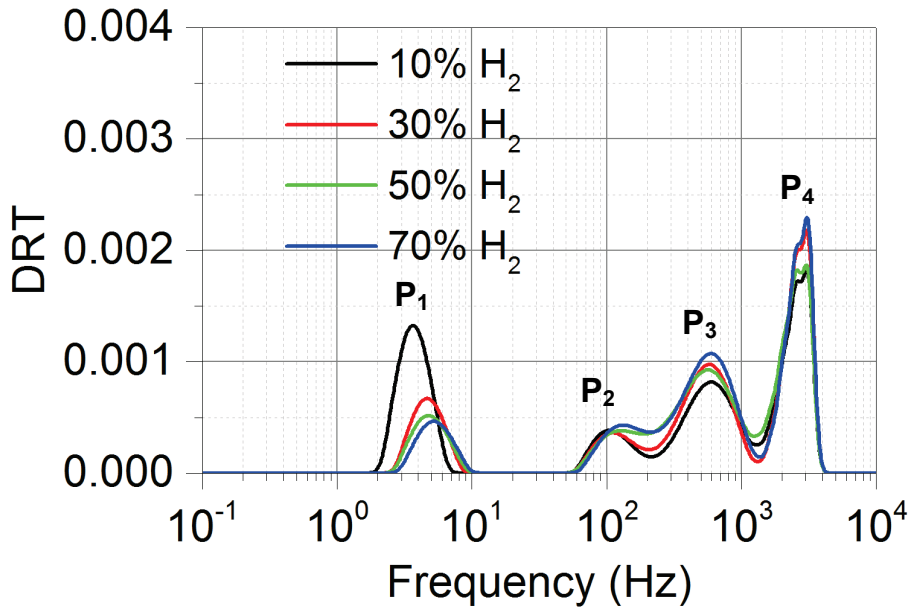
Figure 4.20: DRT plots obtained with different hydrogen partial pressure.

Four DRT peaks can be identified with changing the hydrogen partial pressure. With increasing hydrogen partial pressure, P_1 (at ~5 Hz) exhibits continuous decreasing while P_3 and P_4 show minor changes. Since P_2 is not influenced by changing the hydrogen partial pressure, this peak should be related to an air electrode process.

The hydrogen oxidation reaction at the Ni/YSZ fuel electrode can be generally divided into two steps: 1) hydrogen dissociative adsorption/diffusion at fuel electrode and 2) charge transfer and H_2O formation at electrode/electrolyte interface [194]. For the humidified hydrogen, the hydrogen dissociative adsorption/diffusion at the Ni/8YSZ fuel electrode consists of the following steps:

$$H_2O(gas) + S_M \rightleftharpoons (O - S_M) + H_2$$
$$H_2(gas) + 2S_M \rightleftharpoons 2(H_{ads} - S_M)$$
$$(H_{ads} - S_M) + (O - S_M) \rightarrow (H_{ads} - O - S_M) + S_M$$
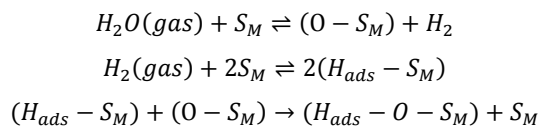
$$(H_{ads} - O - S_M) \rightarrow (H_{ads} - O - S_M)(TPB)$$

where $(O - S_M)$ is the active metal surface site adjacent to an O_{ads} or a suboxide generated by the interaction of H_2O and Ni at elevated temperatures [195].

When hydrogen partial pressure is increased with the H_2O partial pressure kept constant, the processing of the hydrogen dissociative adsorption/diffusion will be easier (lower resistance) considering hydrogen is the reactant in the reaction in step 2. Since the hydrogen dissociative adsorption/diffusion process occurs during the low frequency range, which should be related to the DRT peak P_1 in **Figure 4.20**.

The increased charge transfer resistance observed with increased hydrogen partial pressure in the Nyquist curves should be related to the increasing DRT peak P_3 in **Figure 4.20**. This could be possibly due to the decreased electrode interface conductivity with the decreased pH_2O/pH_2 in the gas mixture [194, 196].

4.3.3 H_2O

As **Table 4.3** shows, a mixed gas was supplied to the fuel electrode side with constant hydrogen partial pressure of 25% and varied H_2O partial pressure between 0% and 75%. Argon was added to balance the flux. During the parameter study experiments of H_2O partial pressure in fuel gas, the air flow rate was kept constant of 16Nl/min and all EIS measurements were performed at 700 °C.

Table 4.3: Operation parameters for the parameter study of H_2O.

	T (°C)	H_2 (Nl/min)		Ar (Nl/min)		H_2O (Nl/min)		Air (Nl/min)	λ (7A)
	700	4.5	25.00%	13.5	75.00%	0	0.00%	16	34.44
	700	4.5	25.00%	9	50.00%	4.5	25.00%	16	34.44
H_2O	700	4.5	25.00%	4.5	25.00%	9	50.00%	16	34.44
	700	4.5	25.00%	0	0.00%	13.5	75.00%	16	34.44

Figure 4.21 shows the Nyquist and Bode plot of the EIS data obtained with different H_2O partial pressure.
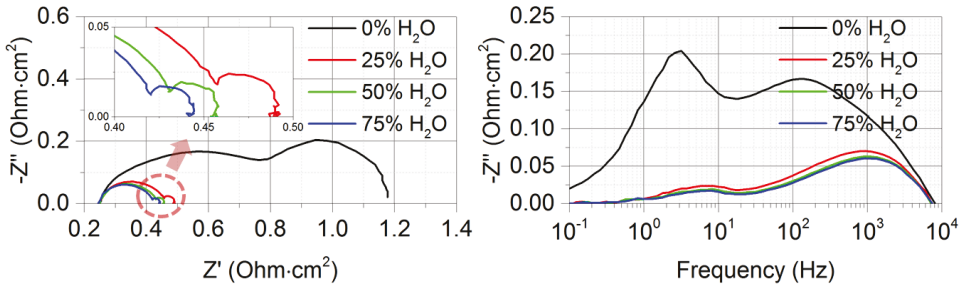
Figure 4.21: Nyquist and Bode plots obtained with different water contents.

Two arcs can be identified in the Nyquist curves with different H_2O partial pressure. For the fuel gas with no H_2O, both the high frequency arc and the low frequency arc become significantly larger than that in the Nyquist curves obtained with humidified hydrogen. With increased H_2O partial pressure, both the high frequency arc (~1 kHz from Bode plot) and the low frequency arc (~5 Hz from Bode plot) shrink, indicating that the resistance for the hydrogen diffusion process and for the charge transfer resistance related to hydrogen all decrease with higher water partial pressure.

Figure 4.22 shows the DRT results calculated from the EIS data in **Figure 4.21**, indicating the H_2O partial pressure dependence of DRT.
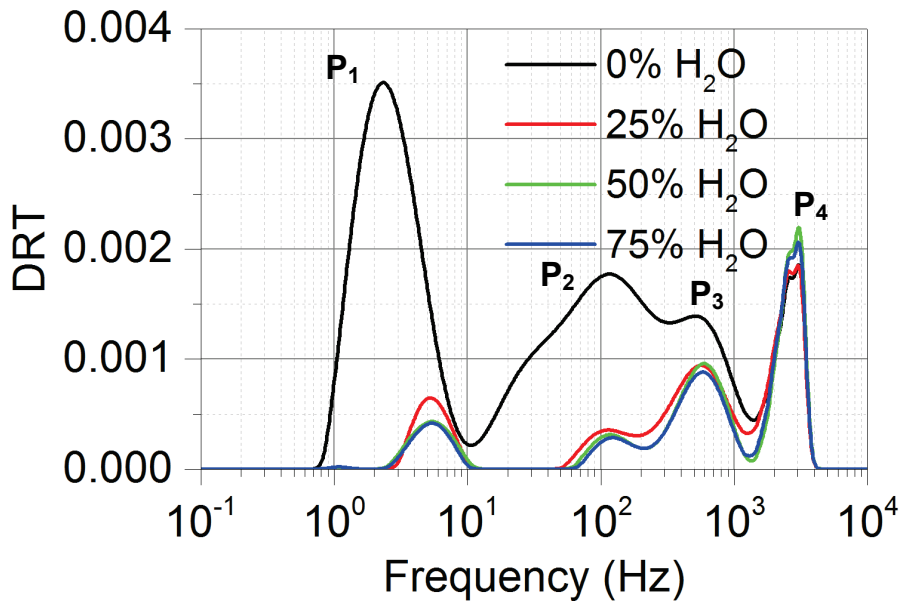
Figure 4.22: DRT plots obtained with different water contents.

Four peaks can be identified from the DRT plots with different water partial pressure in the fuel gas. Among them, P_1, P_2 and P_3 show significant dependency on the water partial pressure in the fuel gas, whereas P_4 is nearly not influenced.

As discussed in the parameter study of hydrogen partial pressure, P_1 is related to the hydrogen dissociative adsorption/diffusion process at fuel electrode. For the humidified hydrogen with constant hydrogen partial pressure, although the increased water partial pressure will lead to reduced $(0 - S_M)$ active metal surface site density, the overall reaction rate is increased due to the much faster surface diffusion via the spillover mechanism which can lead to the fast free up the $(0 - S_M)$ active sites for the dissociative adsorption of hydrogen [194]. Therefore, increasing the water partial pressure will facilitate the hydrogen diffusion at the fuel electrode thus decreasing the diffusion resistance.

The significantly larger diffusion resistance observed with dry hydrogen is due to the different mechanism for the hydrogen dissociative adsorption/diffusion process at the fuel electrode:

$$H_2(gas) + 2S_M \rightleftharpoons 2(H_{ads} - S_M)$$
$$(H_{ads} - S_M) \rightarrow (H_{ads} - S_M)(TPB)$$
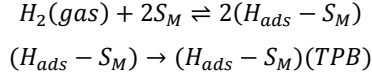
where S_M is the active metal surface site for hydrogen adsorption.

The first step is the hydrogen dissociation process which is very fast at the SOC operation temperatures. However, the coverage of H_{ads} species is very low, resulting in limited surface diffusion rate of hydrogen at the Ni/8YSZ fuel electrode [194]. Therefore, the height of the DRT peak P_1 related to the hydrogen diffusion resistance with dry hydrogen can be significantly larger than that with humidified hydrogen.

P_2 and P_3 are related to the charge transfer processes at the air electrode and fuel electrode, which exhibit significantly larger peak height with dry hydrogen and keep nearly constant with increasing water partial pressure in humidified hydrogen. The charge transfer process at the fuel electrode side can be described with the following equations:

$$(H_{ads} - S_M) \; or \; (H_{ads} - O - S_M) \rightarrow H_{ads}(TPB)$$
$$O^{2-}_{8YSZ} + 2H_{ads}(TPB) \rightarrow H_2O + 2e^-_{8YSZ}(near \; TPB) + V_{\ddot{O}_{8YSZ}}$$
$$2e^-_{8YSZ} \rightarrow 2e^-_M$$
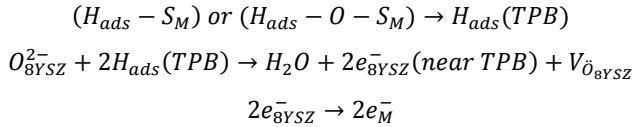
Since the hydrogen dissociative adsorption/diffusion process at the fuel electrode is hindered with dry hydrogen, the rate of the charge transfer reaction and the overall rate of the hydrogen oxidation process are thus limited, leading to the significantly high P_3 with dry hydrogen in **Figure 4.22**. The DRT peak P_2, which is related to the oxygen surface exchange process at the air electrode is also influenced by the rate limited hydrogen oxidation process at the fuel electrode.

For the humidified hydrogen, sufficient active sites are available at the fuel electrode for the hydrogen dissociative adsorption/diffusion process due to the different mechanism

than that with dry hydrogen. Therefore, the charge transfer processes at both electrodes are nearly not influenced by the increased water partial pressure when humidified hydrogen is supplied.

The high frequency DRT peak P_4 has been proved to be related to the ionic transport process in AFL by the parameter study with single cells [20]. Therefore, it didn't change with the humidification on the fuel side.

4.3.4 Temperature

The temperature dependency of the DRT results was investigated through the experiments at four different stack temperatures with the constant gas supply shown in **Table 4.4**.

Table 4.4: Operation parameters for the parameter study of temperature.

	T (°C)	H_2 (Nl/min)		Ar (Nl/min)		H_2O (Nl/min)		Air (Nl/min)	λ (7A)
	650	4.5	50.00%	0	0.00%	4.5	50.00%	16	34.44
	700	4.5	50.00%	0	0.00%	4.5	50.00%	16	34.44
Temp	750	4.5	50.00%	0	0.00%	4.5	50.00%	16	34.44
	800	4.5	50.00%	0	0.00%	4.5	50.00%	16	34.44

Figure 4.23 shows the Nyquist and Bode plot of the EIS data obtained at different stack temperatures.
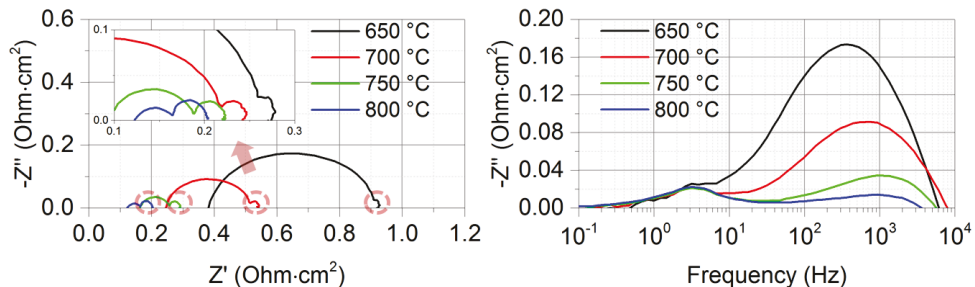
Figure 4.23: Nyquist and Bode plots obtained at different stack temperature.

With increased stack temperature, the conductivity of the electrode and the electrolyte increases, resulting in lower ohmic resistance. The high frequency polarization resistance decrease with increasing temperature while the low frequency polarization resistance was hardly influenced by changing the stack temperature.

Figure 4.24 shows the DRT results calculated from the EIS data in **Figure 4.23**, indicating the temperature dependency of DRT.
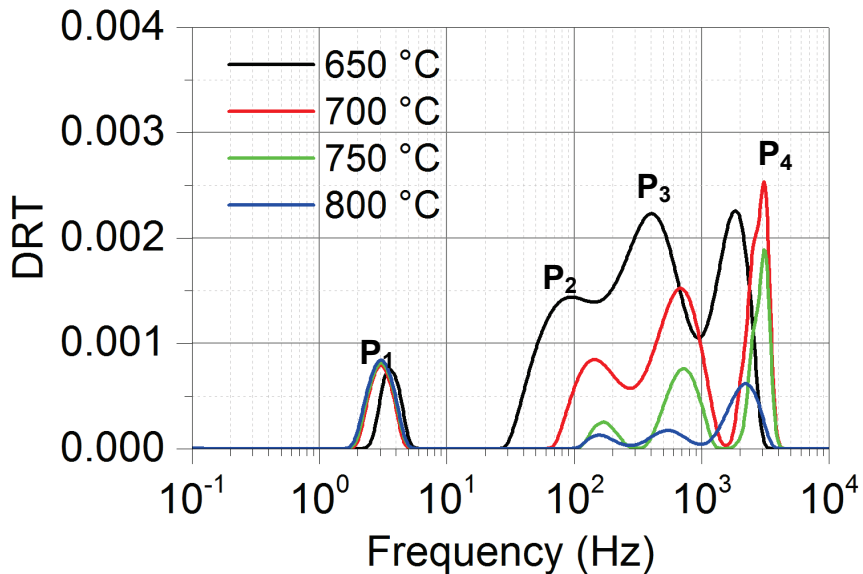
Figure 4.24: DRT plots obtained at different stack temperatures.

It can be seen from the DRT curves that the hydrogen diffusion peak (P_1) keeps nearly constant at varied stack temperatures, indicating that the gas diffusion process at the fuel electrode is independent of temperature which has already been discussed in literature [197]. The electrochemical processes at electrodes such as the charge transfer process are all thermally activated. Therefore, both P_2 and P_3 decrease with increased stack temperature. Since the ionic conductivity of the AFL increases with increased stack temperature, the resistance of the ionic transport process in AFL (P_4) will decrease at higher stack temperature.

In conclusion, the parameter dependency of the DRT peaks observed from a SOC stack fits well with the previous results from single cells by KIT [20], and can be summarized as:

– P_0 (0.1 ~ 1 Hz): Air electrode process (oxygen diffusion in air electrode substrate);
– P_1 (1 ~ 10 Hz): Fuel electrode process (gas diffusion in substrate) overlapped with gas conversion impedance;

- P_2 (10 ~ 200 Hz): Air electrode process (chemical surface exchange of O_2 and O^{2-} bulk diffusion in air electrode);
- P_3&P_4 (200 ~ 2 kHz): Fuel electrode process (gas diffusion coupled with the charge transfer reaction and ionic transport in the fuel electrode functional layer).

4.4 Degradation study of stack using different cell components

As discussed in the Introduction chapter, DRT has been proved as a powerful tool in the study on SOFCs. However, few studies have been carried out with SOEC stacks using EIS&DRT. In this chapter, a four-cell stack (F1004-48) with different components (i.e. air electrode, GDC) was assembled and tested under constant current mode for investigation of the influence on the degradation behavior. EIS measurements and DRT analysis were applied to study the stack performance and degradation mechanisms. With the support of post mortem analysis, the reliability of using DRT technique for in-situ stack degradation analysis could be proved.

4.4.1 Initial electrochemical characterization

The major components of stack F1004-48 are listed in **Table 4.5**.

Table 4.5: Major components of stack F1004-48.

F1004-48	
No. of cells	4
Active area	80 cm^2
Interconnector	Crofer 22 APU
Air electrode	LSC (Cell 2&4 from external supplier) and LSCF (Cell 1&3 from JÜLICH)
GDC Barrier layer	Cell 1&3: PVD; Cell 2&4: Screen printing
Electrolyte	8YSZ (thickness: Cell 1&3: ~10μm; Cell 2&4: ~2μm)
Fuel electrode	Ni/8YSZ
Substrate	Ni/8YSZ
Sealing	Glass ceramic

The joining process was conducted at a furnace temperature of 850 °C with 1 kN external clamping load. Cells were reduced at 800 °C with hydrogen.

After reduction, the open circuit voltages (OCV) of cells with dry hydrogen (4.5 Nl/min) at the fuel side at 800 °C were between 1.089 V to 1.235 V. Apart from cell 4, all other cells showed OCVs higher than 1.2 V, indicating good sealing conditions in cells 1, 2 and 3. The relatively lower OCV of cell 4 indicated a possible leakage through the cell or sealant.

The initial electrochemical performance of the stack was characterized by conducting standard current/voltage (IV-curve) measurements in SOFC mode with 20% humidified H_2 (H_2: 4.5 Nl/min, H_2:H_2O = 4:1) at stack temperatures of 800 °C, 750 °C, 700 °C and 650 °C. The IV curves of the cells at different temperatures are shown in **Figure 4.25**.
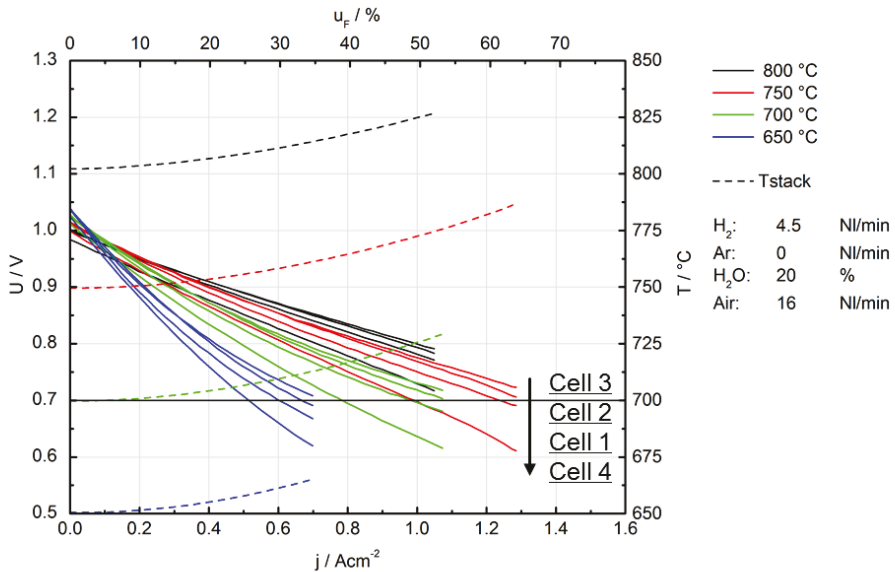
Figure 4.25: IV curves of the stack in SOFC mode with 20% humidified H_2 (H_2: 4.5 Nl/min, H_2:H_2O = 4:1) at a stack temperature of 800 °C, 750 °C, 700 °C and 650 °C.

The scan rate for the current during IV-curve measurements was set as 4 A/min. The stack temperature (measured at the interconnector connecting cell 2 and cell 3) rose with increasing current density, as shown in **Figure 4.25**. A high temperature limit of 825 °C and low voltage limit of 0.6 V were set during the measurements.

The stack showed good performance at the beginning of the operation: At ~775 °C stack temperature, three cells reached ~1.3 Acm^{-2} at a working voltage of 0.7 V. Even at 650 °C, an average power density of around 420 mWcm^{-2} could be reached at the cell voltage of 0.7 V. At each temperature, cell 3 (with LSCF electrode) showed the best performance, while the performance of cell 4 was relatively poorer than others.

Figure 4.26 shows the Nyquist plots of the four cells at 800 °C with 20% humidified H_2. The ohmic resistance of cell 4 is higher than that of the other three cells, while cells 2 and 3 showed the lowest ohmic resistance. Considering that the cell temperature of cell 1 was about 15 °C lower than that of the other cells, it showed higher ohmic resistance than cells 2 and 3. As is noted in Table 1, the thickness of the 8YSZ electrolyte in cells 2 and 4 is much thinner than that in cells 1 and 3. Therefore, the ohmic resistance of cells 2 and 4 should be lower than that of cells 1 and 3, assuming all other issues in all layers are identical. Possible explanations for the highest ohmic resistance in cell 4 could be: 1) local oxidation of Ni due to gas leakage; 2) poor conductive layer formation within cell 4; and 3) the bad contact of cell components.
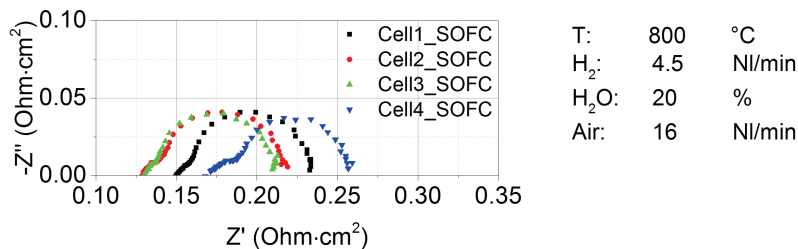
Figure 4.26: Impedance spectra of the four cells at 800 °C (H_2: 4.5 Nl/min, H_2:H_2O = 4:1).

4.4.2 Durability test (stationary SOEC operation)

The stationary electrolysis operation was initiated following the performance characterization. As shown in **Figure 4.27**, the stack temperature was kept at 800 °C. In order to obtain comparable results to the SOEC stack tested in Jülich [5], the gas flow rates were kept constant during the electrolysis operation as 4.5 Nl/min H_2 and 4.5 Nl/min H_2O at fuel side (H_2:H_2O = 1:1) and 16 Nl/min air at air electrode side. The current density was kept at -0.5 Acm^{-2} during electrolysis operation, which corresponds to a steam conversion rate of 50%. The electrolysis process was stopped after about 1000 hours of operation.
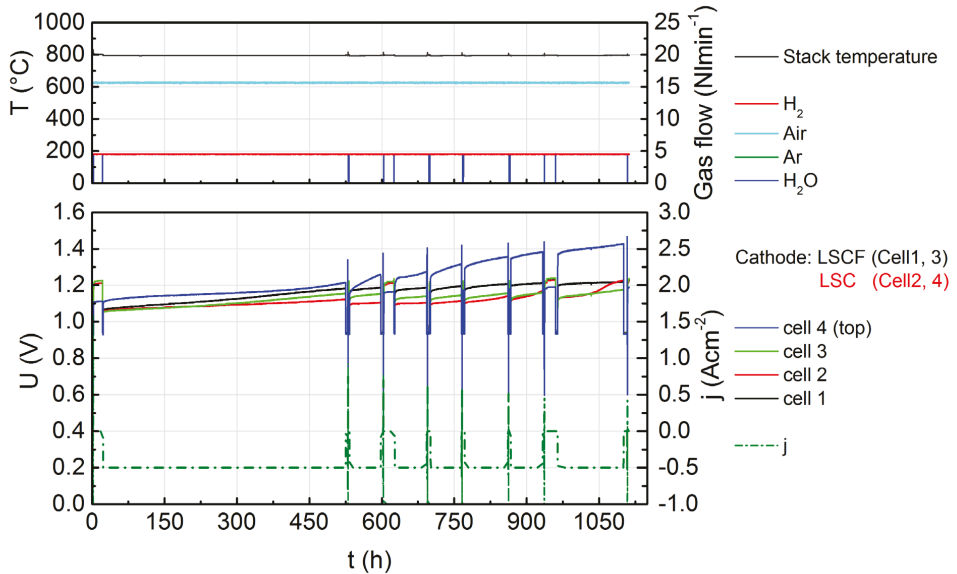
Figure 4.27: Time plot of the stack in stationary electrolysis condition: T_{stack}=800 °C, H_2:H_2O = 1:1, j= -0.5 Acm^{-2} (50% steam conversion rate).

All cells showed rapid degradation and the voltage degradation rates were: cell 1 (12.5%/kh), cell 2 (14.4%/kh), cell 3 (10.2%/kh) and cell 4 (26.2%/kh). For cell 1 and cell 3, the degradation rates were nearly constant during the entire operation, while for cell 2

and cell 4, the degradation rates kept increasing over time, significantly after ~700 hours of operation. Considering the differences in the material compositions, as well as the preparation methods, the degradation mechanisms of these cells may be different and may not only be due to the difference in the air electrode.

The IV-curve measurements shown in **Figure 4.28** were conducted in both SOFC and SOEC modes at different time periods during the stationary operation. All cells showed fast degradation during the first 500 hours. As was already shown in the time plot, the degradation rates of cell 2 and cell 4 with the LSC air electrode increased after 500 hours of operation, while the degradation rates of cell 1 and cell 3 were kept nearly constant.
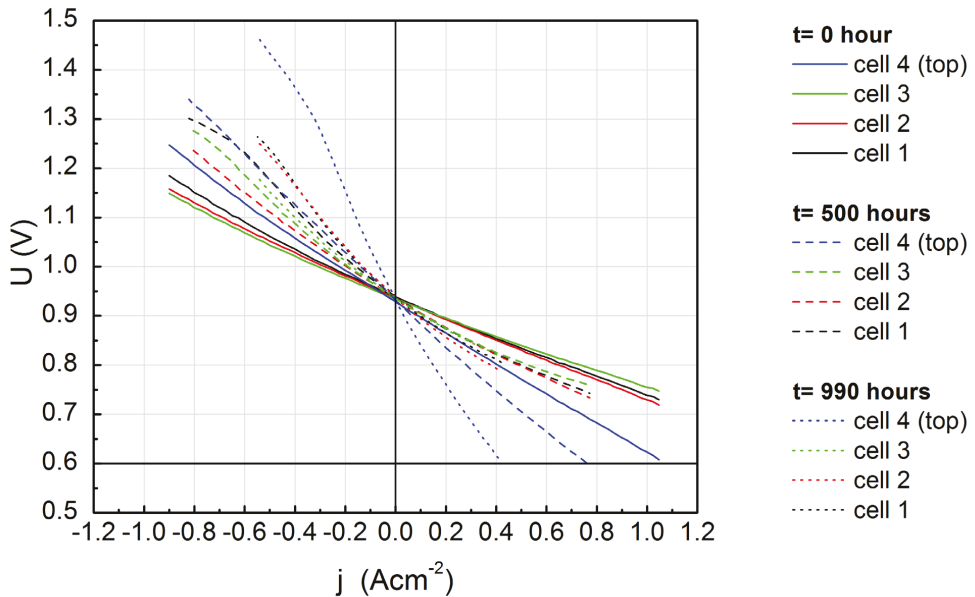
Figure 4.28: Stack performance under SOFC and SOEC mode with 50% humidified H_2 at the beginning of long-term stationary operation (t = 0 hour), after 500 hours of operation (t = 500 hours) and 990 hours of operation (t = 990 hours).

4.4.3 EIS results

Electrochemical Impedance Spectroscopy (EIS) was utilized in the study of the electrochemical performance of the stack, as well as of the degradation behavior during the stationary operation. **Figure 4.29** shows the impedance spectra of all cells obtained at different operation times.
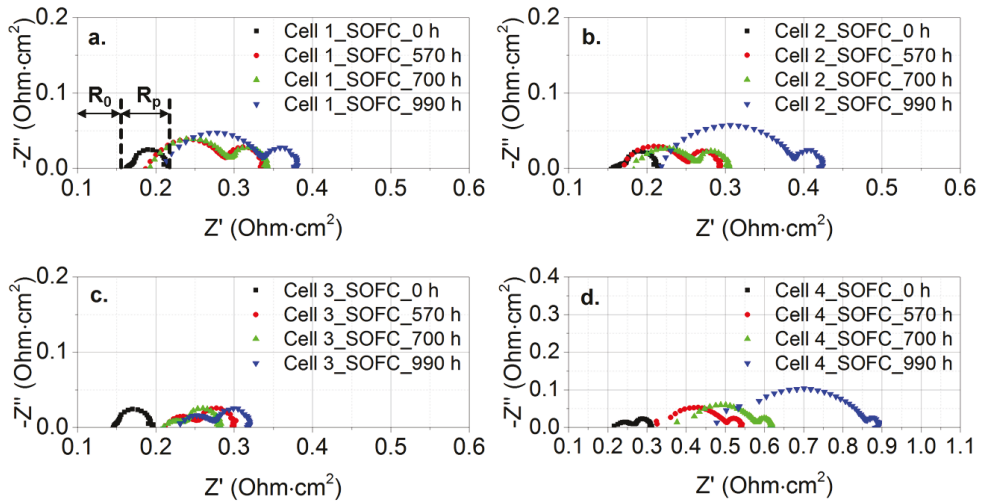
Figure 4.29: Impedance spectra of Cell 1(a.), Cell 2(b.), Cell 3(c.) and Cell 4(d.) measured at 800 °C (H_2: 4.5 Nl/min, H_2:H_2O = 1:1).

In general, the Nyquist curve for each cell clearly showed two arcs. It must be noted that the scales in the Nyquist plots for cell 4 are different from the other three cells due to its relatively larger impedance. At the beginning of operation, cell 4 showed the highest ohmic resistance, as well as an obviously greater high frequency polarization resistance. The ohmic and high frequency polarization resistance of the other three cells kept increasing with operation time, while cell 4 showed a significantly higher degradation rate.

In order to quantitatively analyze the impedance evolution of each cell, as indicated in **Figure 4.29a**, two impedance values were taken from each spectrum, which are R_0 – ohmic resistance and R_p – polarization resistance. In **Figure 4.30** these two impedance values are plotted for each cell against the operation time.
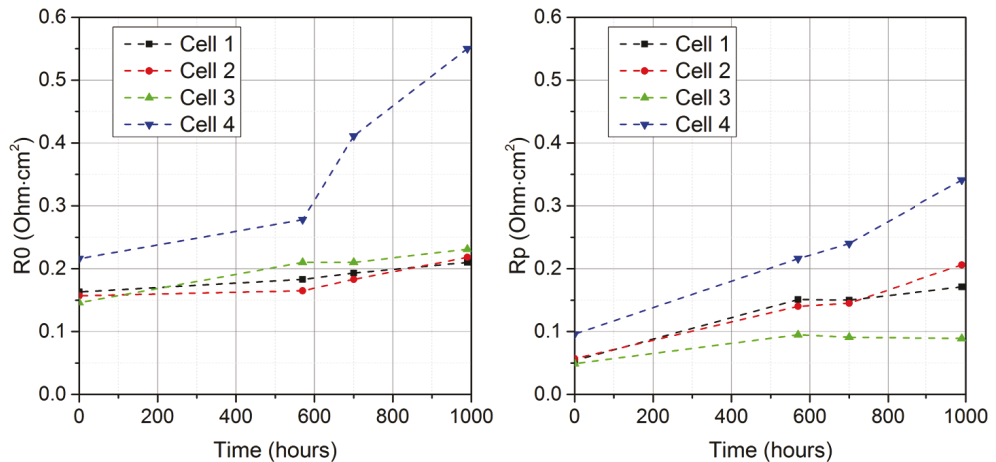
Figure 4.30: Evolution of R_0 – ohmic resistance and R_p – polarization resistance for each cell as a function of operation time.

R_0: The ohmic resistance of each cell kept increasing over the operation time. Amongst them, cell 4 showed a larger ohmic resistance at the beginning of the operation. Especially after ~500 hours of operation, the ohmic resistance of cell 4 increased drastically and kept increasing more rapidly than that of the other three cells until the end of operation. According to related literatures [12, 163, 198], reasons for the increasing ohmic resistance can be: 1) scale growth on the interconnector; 2) conductivity degradation of the electrolyte; 3) nickel depletion in the anode functional layer, etc.

R_p: The polarization resistance kept increasing for each cell during the operation. Cell 2 and cell 4 showed a larger increasing rate than the other two. Especially after ~700 hours of operation, the increasing rate of R_p for cell 1 and cell 3 became smaller, while cell 2 retained the same increasing rate and that of cell 4 increased even faster. As R_p

includes the polarizations of electrochemical processes occurring at both electrodes, further analysis is needed to resolve the different contributions to the total polarization, which are generally overlapped in the Nyquist plots.

4.4.4 DRT analysis

In the Nyquist plots, individual electrochemical processes generally merge with others, which makes them difficult to separate. DRT offers a better opportunity to isolate the electrochemical processes with different time constants. In **Figure 4.31**, the results of the DRT calculations of the four cells are plotted for different operation times.
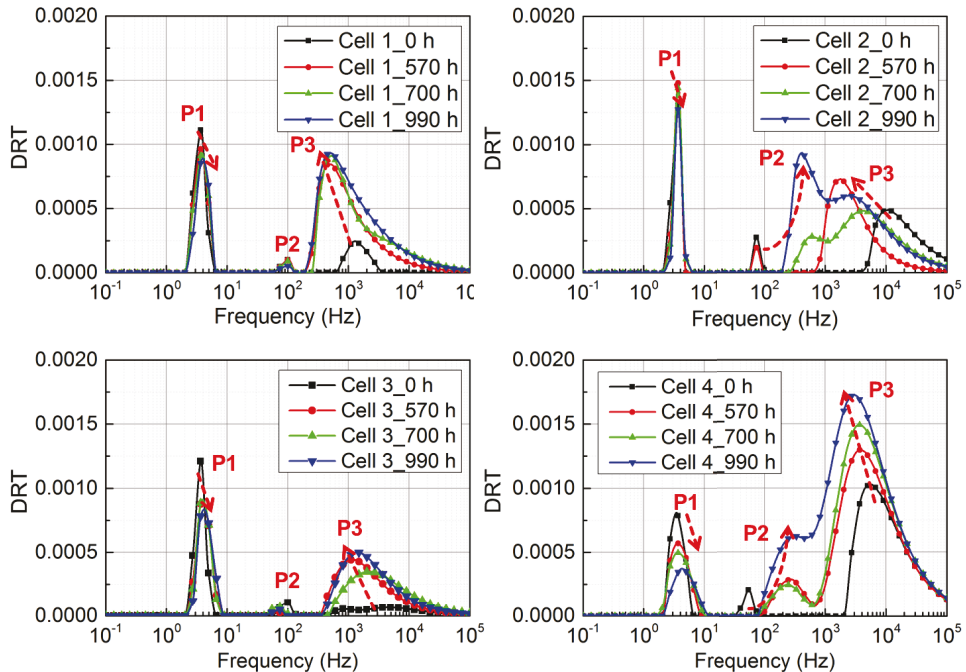
Figure 4.31: DRT results of the cells for different operation times.

Unlike what was observed in the Nyquist plots, three peaks could be identified from the DRT plots for both cells. It can been seen from the DRT curves of cell 3 before operation (0 hour) that P_3 and P_4 could be distinguished in the beginning but overlapped during stack operation. This phenomenon indicates that the characteristic frequencies of these two processes (P_3 and P_4) became similar due to the electrode degradation which made it difficult to separate these two DRT peaks. According to Leonide [18] and previous stack tests using similar types of cells [5], the observed peaks in the DRT plot are:

– P_1 (1 ~ 10 Hz): Fuel electrode process (gas diffusion in substrate) overlapped with gas conversion impedance;

– P_2 (10 ~ 200 Hz): Air electrode process (chemical surface exchange of O_2 and O^{2-} bulk diffusion in air electrode);

– P_3&P_4 (200 ~ 2 kHz): Fuel electrode process (gas diffusion coupled with the charge transfer reaction and ionic transport in the fuel electrode functional layer).

P_1 decreases for all cells, which means the gas diffusion resistance at the fuel electrode (Ni-8YSZ) decreases with increasing operation time. The most plausible reason for this could relate to the agglomeration or even loss of nickel at the fuel electrode, which increases the porosity of the fuel electrode and facilitates gas diffusion.

P_3 is a fuel electrode process coupled with P_1. This peak increases in the first hundreds hours and then keeps nearly constant for cell 1, 2 and 3. As discussed in literature, the Nickel particles in the inner reactive layer of Ni/YSZ electrode will migrate outwards from the electrolyte, which leads to nickel depletion in the AFL during the SOEC operation. Meanwhile, the migration of nickel is along with 1) the contact loss between nickel and YSZ and 2) possible nickel overgrowth/ agglomeration in the fuel electrode substrate [199, 200]. The contact loss between Ni and YSZ will lead to the reduction of chemically-active sites (TPBs) and results in the increase of polarization resistance (P3 increases). The Ni-depleted AFL is like a porous YSZ layer with much poorer conductivity than the dense electrolyte. In the outer layer from Ni-depleted AFL, the migrated Ni could possibly 1) deposit and re-contact with YSZ which forms new TPBs or 2) deposit on nickel particles and results in nickel overgrowth/agglomeration. The possible dynamic

balance of reduction and formation of TPBs will result in only the increase of ohmic resistance (R_0 increases) but not electrode polarization, which could explain why P_3 keeps nearly constant after the first hundreds hours for cell 1, 2 and 3. However, P_3 keeps increasing for cell 4 during the operation, which indicates that the reduction of TPBs in cell 4 couldn't be compensated. Therefore, the electrochemical processes like charge transfer at the fuel electrode of cell 4 was hindered during the operation.

The development of P_2 during operation is very different between cells 1/3 and cells 2/4. It increases significantly with the operation time for cells 2/4, while the same peak with cells 1/3 shows nearly no change. Since this peak is related to an air electrode process, it indicates that the air electrode's degradation should be much more significant in cells 2/4. The different chemical or thermal stability of the two air electrode materials during high temperature electrolysis operation could potentially result in the different degradation behaviors.

Besides the difference in air electrode material, as mentioned in **Table 4.5**, the preparation methods for the GDC layer are different between cells 1/3 and cells 2/4. The GDC layer prepared by the PVD is generally dense and thin, while the screen-printed GDC layer is more thick and porous. Therefore, the different preparation method of the GDC layer could possibly also influence the degradation behavior of the air electrodes.

In conclusion, the motivation of conducting EIS tests and DRT calculation is to investigate an in-situ diagnostic approach to stacks during operation. The EIS&DRT results indicate that degradation may occur on the air electrode side of cell 2 and cell 4. All cells showed degradation at the fuel electrode side. Possible delamination was expected in cell 4 given the drastic increase in ohmic resistance in cell 4 at about 600 hours. The following post-mortem analysis (SEM and EDX) was performed in order to figure out the degradation mechanisms for each cell, which could possibly in turn prove the diagnostic results or predictions obtained from the EIS&DRT analysis.

4.4.5 Post-mortem analysis

Figure 4.32 shows the SEM pictures of fracture samples from cells 2, 3 and 4 prepared through laser cutting. In addition, the SEM picture of one cell from another stack (F1002-106) is also shown for comparison. In this stack, LSCF was used as air electrode material and a GDC layer with the thickness of about 6.5 μm was prepared by screen printing. This stack showed almost no degradation after 2000 hours of steam electrolysis (800 °C, H_2:H_2O = 1:1, 0.3 Acm^{-2}, FU = 15%).
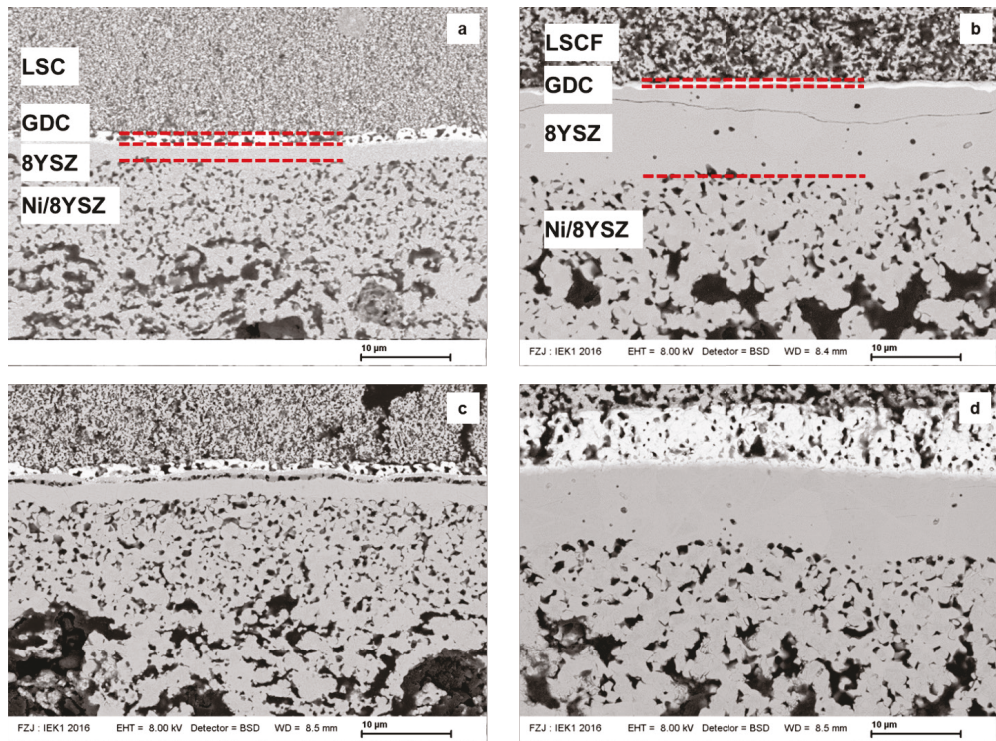
Figure 4.32: Backscattered Electron Detector (BSD) image of polished fracture surface of (a.) cell 2; (b.) cell 3; (c.) cell 4 from stack F1004-48; and (d.) cell 1 from stack F1002-106 after the electrolysis test.

The structure and main components of each cell can be identified in **Figure 4.32**. For cell 3 of stack F1004-48 (**Figure 4.32b**), slim lateral cracks were observed within the electrolyte that were very likely to be formed during the SEM sample preparation. No obvious structural damage was observed for the thin, dense GDC layer coating on the electrolyte. Furthermore, no obvious delamination was observed between LSCF/GDC/8YSZ.

Unlike the cell from F1002-106, partial decomposition of the thin porous GDC layer could be observed in cell 2 (**Figure 4.32a**) and cell 4 (**Figure 4.32c**). Delamination between the GDC layer and electrolyte could be observed in cell 4. An additional layer formation beneath the GDC layer was observed that could possibly be a $SrZrO_3$ interlayer. Moreover, a discontinuous phase with a different material contrast could be observed between the delamination gap in cell 4. The chemical composition of this phase and the interlayer will be measured at higher magnification.

In the functional layer of the fuel electrode, the pore distribution is different between cell 3 and cells 2 and 4. With the help of graphic analysis using Matlab, the calculated pore density for cells 2 and 4 is about 5% higher than that of cell 3. As already discussed above, the higher porosity can possibly lead to lower gas diffusion resistance (smaller P1) at the fuel electrode. Looking back to the DRT plots in **Figure 4.31**, cell 4 showed a significantly smaller P_1 than cell 3, which matches the information obtained from their SEM pictures in **Figure 4.32**. Compared to cell 4, cell 2 showed smaller P1 in its DRT plot. However, no obvious difference could be observed on the fuel electrode side from the SEM pictures of cell 2 and cell 4 at this magnification in **Figure 4.32**.

In **Figure 4.33d**, the formation of $SrZrO_3$ below the porous GDC layer can be confirmed. With an even thinner and porous GDC layer in cells 2 and 4 of stack F1004-48, such an $SrZrO_3$ formation can also be observed using higher magnification, as shown in **Figure 4.33a** and **Figure 4.33c**. Micro cracks are found at the fuel electrode of cell 4 in **Figure 4.33c**. Along with the formation of micro cracks, isolated Ni/YSZ particles are also observed in cell 4. This may result in the deduction of TPBs and influence the charge transfer or ionic transport processes at fuel electrode, which could help explain the continuous fuel electrode degradation (P3 increases) in cell 4.
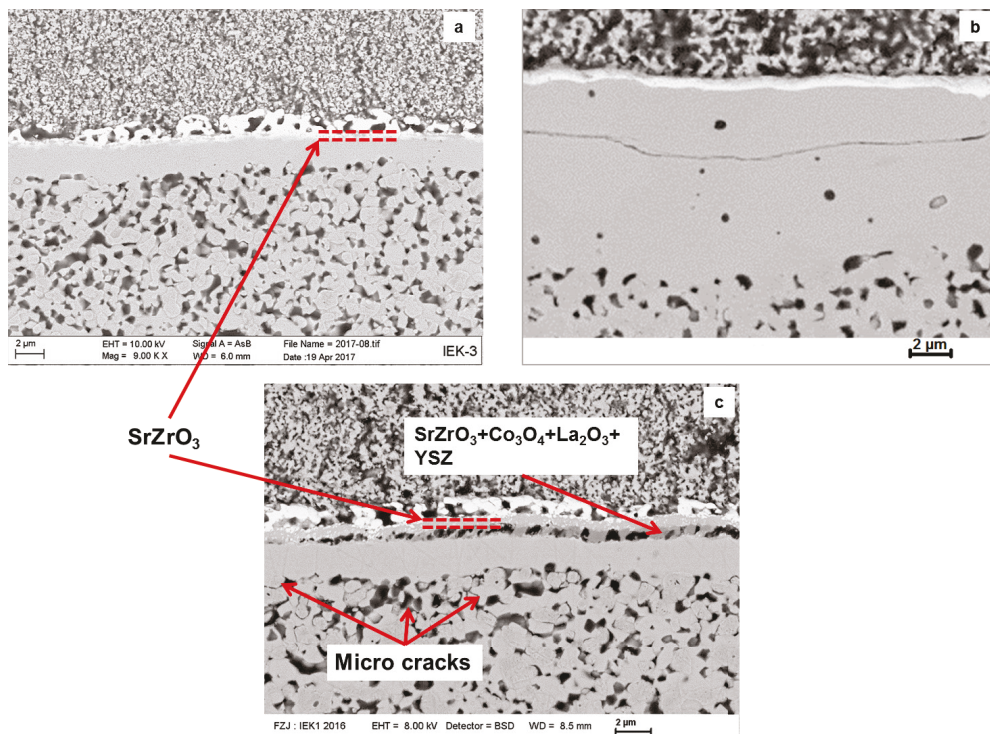
Figure 4.33: Backscattered Electron Detector (BSD) image of fracture surface of (a.) cell 2; (b.) cell 3 and (c.) cell 4.

The GDC layer prepared by PVD in cell 3 showed no dissolution or structural damage. Moreover, no $SrZrO_3$ interlayer formation could be observed between the GDC layer and electrolyte. As shown in **Figure 4.30**, the ohmic resistances of cell 2 and cell 4 were identical or higher than those of cell 1 and cell 3, which was not expected before starting the test, since cell 2 and cell 4 had much thinner electrolytes (**Figure 4.32**). The formation of a $SrZrO_3$ insulating layer should be one of the reasons for the higher resistance in those cells.

The discontinuous phase that formed between the delamination gap in cell 4 was analyzed by EDX, and the results indicate that this phase was a solid solution consisting of $SrZrO_3$, Co_3O_4, La_2O_3 and YSZ. Co_3O_4 and La_2O_3 were determined to be the decomposition products of LSC at high temperature [7]. Although the mechanism for the

formation of this solid solution is still unknown, it is quite clear that the LSC air electrode of cell 4 partially decomposed during the operation. Due to the loss of active material in the air electrode, the height of the air electrode-related DRT peak – P$_2$ of cell 4 in **Figure 4.31** – shows an obvious increase during operation. Moreover, the delamination gap between the GDC layer and electrolyte in cell 4 could also explain the drastic increase in its ohmic resistance after about 600 hours of operation in **Figure 4.30**.

A four-cell stack was built conforming to JÜLICH's F10 design with two different air electrode materials. Nearly 1000 hours of steam electrolysis was performed with this stack at 800 °C under a constant current density of -0.5 Acm^{-2}. The average voltage degradation rate was 15.8%. The results from EIS measurements and the further DRT analysis ascribed the degradation to the individual components of each cell. During the post-mortem analysis, several degradation phenomena were observed:

a) Increasing porosity at the fuel electrode (all cells)
b) The formation of micro cracks between Ni/YSZ particles at the fuel electrode (Cell 4)
c) Nickel gradient in AFL (Cell 3, 4)
d) SrZrO$_3$ layer formation at the 8YSZ and porous GDC interface (Cell 2, 4)
e) Loss of the GDC layer (Cell 2, 4)
f) Air electrode delamination and GDC delamination (Cell 4)
g) Formation of a solid solution within the YSZ/GDC delamination gap (Cell 4)

Clearly, compared to former stacks, the very thin porous GDC layers prepared by screen printing in cells 2 and 4 (with LSC electrode) is the major reason for the degradation phenomena on the air side observed. Therefore, the difference of LSCF and LSC air electrodes in SOEC mode cannot be compared directly. To which extent the behavior of cell 4 was affected by the observed leak in layer 4 cannot be identified, but there might be a correlation that merits further investigation.

As concluded before in the post-mortem analysis, EIS and DRT were expected to function as an in-situ diagnostic approach of stacks during operation. The feasibility and reliability of this approach was proven by the post-mortem analysis. The post-mortem

analysis of this stack has helped to explain the rapid degradation of this stack, especially of cell 4. Degradation mechanisms were proposed that could feasibly support the diagnostic results and predictions from the previous EIS&DRT analysis.

4.5 Summary of Discussions

The aim of this thesis is the investigation of SOC stack characterization in large test rigs using EIS and DRT. Both EIS and DRT are very sensitive to the electrical noises during the impedance measurement. For the low impedance system like SOC stacks, this influence becomes even more significant. By adding an inductive element into a purely simulated equivalent circuit with five series connected RC elements, the influence of inductance on EIS and DRT were studied. With higher inductance value, the Nyquist plot shows longer high frequency tails and the high frequency arc is more depressed. As a result, larger ohmic resistance will be estimated from the Nyquist plot, which is also reported in literature [181, 182]. With increasing inductance, the DRT peaks at high frequency will shift to lower frequency and the peak height is also affected. Therefore, without optimization of cabling for EIS measurements, the test rig inductance has been proved to affect the EIS data and calculated DRT especially at high frequencies.

The influence of test rig inductance on EIS was studied during the EIS measurement with one short stack (F1004-87). Cell 4 in this stack shows no degradation in the IV-curve measurement after changing the test rig, while the larger ohmic resistance in the Nyquist plot indicated that cell 4 degraded after changing test rig. The DRT peak P4 located at ~2 kHz shifted to ~600 Hz and the small peak P3 located at ~200 Hz disappeared. This phenomenon is similar as what was observed in the previous simulation with equivalent circuit. The inductance correction was then carried out by subtracting the inductive part from the stack impedance as reported in literature [181]. The inductive part was obtained via the short circuit test in which the EIS measurement was performed on a piece of metallic interconnector with the test rig. After the inductive part at high frequencies has been corrected, identical Nyquist plot with that before changing test rig was obtained. The DRT peaks which were hidden or shifted in characteristic frequency were also corrected.

It has been proved in literature that DRT is much more sensitive to the change in inductance values than ADIS [180], which corresponds to the observation from the EIS measurements in different test rigs. By comparing the corrected EIS and DRT results with that obtained before changing test rigs, the inductance correction process via short

circuit test functioned well. It is thus highly recommended to carry out inductance correction if the stack test is performed in different test rigs, so that the EIS data measured in different test rigs can be comparable.

The influence of the electrical noises from the built-in electric load and power supply on the EIS data quality was first studied during a short-circuit EIS test. A high frequency loop (> 30 kHz) in the Nyquist plot was observed when the power supply and electric load was connected to the circuit for EIS measurement. This noisy signal disappeared after the built-in power supply and electric load was physically disconnected. For safety reasons, a switch was installed in the test rig, which could enable the switch between the circuit for DC operation and for EIS measurement. The function of this switch was proved by comparing the EIS data of the stack F1005-06 measured with and without the switch, in which the high frequency noise was effectively removed via the switch.

Low frequency noises in the EIS data are frequently observed when the steam supply to the fuel electrode is unstable due to condensation along the pipes. Voltage fluctuation can be observed since the cell voltage is sensitive to the partial pressure of steam in fuel gas, and this fluctuation in voltage will result in noisy signals in the measured EIS data especially at low frequencies. The influence of this type of noisy signal on DRT was first studied by simulated equivalent circuit. Noisy signals at low frequencies were manually added into the simulated perfect EIS data from an artificial equivalent circuit containing three RC elements. The DRT plot of the perfect 3RC circuit showed three DRT peaks located at the correct frequencies, while the DRT plot with noisy signals showed additional peaks with smaller peak height in the low frequency range (< 10 Hz). This result indicates that the noisy signal in the EIS data can affect the data continuity, which will lead to the appearance of an additional fake process observed in the DRT plot.

The steam supply will be relatively stable when the mass flow controller for water does not work near its lower or upper limits. However, for the Jülich F10 short stacks with less than four cells, the normal water supply is always near the lower limit of the mass flow controller. In this case, the HIT (Hilbert Transformation) is applied to the EIS data post-processing. By processing one set of EIS data from the stack F1004-82 measured with low water flow rate, the noisy signals at low frequency were removed in the Nyquist and Bode plots. In the DRT plot of the original data without the HIT correction, one

additional peak was observed at ~0.6 Hz with low peak height and narrow frequency range, which should not appear under normal operation condition. After the HIT correction, this low frequency peak was removed.

The DRT peaks identification was performed with the stack F1004-72 through the systematic parameter study during which the gas composition (Air, H_2 and H_2O) and stack temperature were varied. Up to five DRT peaks with the number from P0 to P4 were identified during the parameter study. P0 (0.1 ~ 1 Hz) and P2 (10 ~ 200 Hz) were related to air electrode processes since P0 only appeared when the air supply was insufficient while P2 was not affected by changing hydrogen flow rate at fuel electrode. P1 was affected by changing hydrogen and steam flow rate but not thermally activated, thus P1 was ascribed to the hydrogen diffusion process at fuel electrode substrate. The significantly high P1 with dry hydrogen was due to the limited surface diffusion rate of hydrogen at the Ni/8YSZ fuel electrode when dry hydrogen was supplied [194]. The charge transfer processes P2 and P3 were thus hindered due to the reduced hydrogen dissociative adsorption/diffusion process at the fuel electrode. P4 was proved to be related to the ionic transport process in AFL by the parameter study with single cells [20], so that this peak was dependent on the stack temperature which can affect the material conductivity.

In conclusion, the parameter dependency of the DRT peaks was first conducted with a SOC stack and the results fit well with the previous results from single cells by KIT [20], which can be summarized as:

– P_0 (0.1 ~ 1 Hz): Air electrode process (oxygen diffusion in air electrode substrate);
– P_1 (1 ~ 10 Hz): Fuel electrode process (gas diffusion in substrate) overlapped with gas conversion impedance;
– P_2 (10 ~ 200 Hz): Air electrode process (chemical surface exchange of O_2 and O^{2-} bulk diffusion in air electrode);
– P_3&P_4 (200 ~ 2 kHz): Fuel electrode process (gas diffusion coupled with the charge transfer reaction and ionic transport in the fuel electrode functional layer).

A four-cell stack was built conforming to JÜLICH's F10 design with two different air electrode materials (LSC and LSCF). During the 1000 hours stationary electrolysis operation with the stack F1004-48, the EIS measurements were performed regularly.

Together with the evolution of individual DRT peaks, the degradation mechanisms of each cell can be predicted. The EIS&DRT results indicated that degradation may occur on the air electrode side of cell 2 and cell 4 (LSC with porous GDC). All cells showed degradation at the fuel electrode side. Possible delamination was expected in cell 4 given the drastic increase in ohmic resistance in cell 4 at about 600 hours. In the post-mortem analysis, the formation of $SrZrO_3$ was observed at the air electrode/electrolyte interfaces in cell 2 and cell 4, which was widely reported as the most common degradation mechanism for this kind of air electrode materials [147, 148]. Since the formation of poor-conductive $SrZrO_3$ consumed Sr from air electrode, this should correspond to 1) the increasing ohmic resistance observed in the Nyquist plot and 2) increasing of P2 (charge transfer process at air electrode) in the DRT plot. A solid solution layer containing $SrZrO_3$, Co_3O_4, La_2O_3, and YSZ formed between the GDC layer and electrolyte in cell 4, which can contribute to the delamination of the air electrode and GDC layer from electrolyte. This degradation mechanism was reported to be the decomposition products of LSC at high temperature [7]. Together with the air electrode delamination during electrolysis operation [161, 162], a drastic increasing of ohmic resistance was thus observed in the Nyquist plot. Nickel gradient was observed in AFL (Cell 3, 4), which was reported as Nickel depletion at fuel electrode during SOEC operation [12]. This phenomenon would result in the formation of porous YSZ layer with much poorer conductivity instead of the dense AFL, which can lead to significant increasing of the ohmic resistance.

The EIS and DRT gave prediction to the stack degradation mechanisms during the electrolysis operation, which offered direction for performing the post-mortem analysis. The degradation phenomenon observed in the post-mortem analysis has successfully proved the feasibility and reliability of using the combination of EIS and DRT as an in-situ diagnostic tool for the degradation study of SOC stacks.

5. Summary

This thesis dealt with the electrochemical characterization and the degradation study of the SOC (Solid Oxide Cell) stacks using EIS and DRT techniques. The SOCs are of great interests due to the advantages in many aspects such as fuel flexibility, high efficiency and good reversibility. The high operation temperatures (600 °C ~ 900 °C) have proposed strict requirements on the thermal and chemical stability of the stack materials to avoid fast degradation. The degradation mechanisms for the SOFC stacks have been widely studied, while for the SOEC stacks are still very few. Due to the differences in the gas composition and polarization current under the two operation modes for SOCs, the mechanisms for the performance degradation can be different.

Electrochemical impedance spectroscopy (EIS) has been proved as a powerful AC technique to characterize the performance and to study the degradation mechanisms of SOCs. Together with the analysis of the distribution function of relaxation times (DRT) of the impedance response, more reliable information can be obtained from the EIS results. The combination of EIS and DRT has been used mostly for the single cell analysis. One of the main objectives of this thesis was to extend the application of EIS/DRT technique to SOC stacks.

The high sensitivity of EIS makes it difficult to obtain data with good quality, especially with the low impedance like the SOC stack. When performing EIS measurements with SOC stacks in test rigs, the EIS data quality is mainly influenced by 1) high background inductance; 2) noise from the external electric devices and 3) unstable signal at low frequencies.

The influence from the high background inductance on the EIS data becomes significant at high frequencies, which can mislead the determination of the ohmic resistance from the Nyquist plot. Additionally, by analyzing the EIS data from the simulated circuit and the real stack tests, the high inductance has been proved to affect the calculated DRT results by changing the characteristic frequencies of the DRT peaks and causing the loss of DRT peaks. This problem can be solved by optimizing the cabling for EIS measurements such as using short and twisted cables, which may be difficult for

the measurements with large-scale test rigs. Another method dealing with the high inductance is the inductance correction with the raw EIS data during the data post-processing. The background inductance signal of the test rig can be obtained through the EIS measurement with a prominent electrical conductor (i.e. Pt) in the test rig, and the inductance correction is realized by subtracting the background inductance from the raw EIS data. By analyzing the raw and corrected EIS data from the stacks, the inductance data correction has been proved effective in improving the data quality.

Apart from the high inductive signal from the test rig, the unstable signals at low frequencies mainly due to the unstable steam supply in the test rig can also impact the EIS data quality and the DRT results. This problem can be effectively solved by applying the Hilbert transform (HIT) to the data post-processing, which can remove the low frequency noises in the EIS data as well as the artificial peaks in the DRT plot.

It has been proved that the noise from the external electric devices such as the electric load and power supply can result in noisy signals in the EIS data mainly at high frequencies. This type of noisy signals can be avoided through the installation of a switch in the test rig which can separate the electric load and power supply from the circuit for EIS measurements.

Before applying the DRT to the study of SOC stacks, it is necessary to distinguish the DRT peaks with overlapped electrochemical processes in the SOC stack. Such analysis has been performed with single cells by the researchers in KIT. During this work, the DRT peaks in SOC stacks were identified through the parameter study. The parameter dependency of the DRT peaks has been discussed and fits well with the result from KIT.

During the stationary electrolysis operation with the stack F1004-48, EIS measurements were performed regularly to record the impedance evolution of the stack. By analyzing the EIS data with DRT, the degradation mechanisms for individual cells were predicted. During the post-mortem analysis with SEM and EDS, the degradation of induvial cells were observed, which is in consistent with the DRT result. The reliability and feasibility of EIS&DRT as a diagnosis technology with SOC stacks is thus proved.

6. References

1. Talawar, M.B., et al., *Environmentally compatible next generation green energetic materials (GEMs).* Journal of Hazardous Materials, 2009. **161**(2-3): p. 589-607.

2. Ursua, A., L.M. Gandia, and P. Sanchis, *Hydrogen production from water electrolysis: current status and future trends.* Proceedings of the IEEE, 2012. **100**(2): p. 410-426.

3. Ibrahim, H., A. Ilinca, and J. Perron, *Energy storage systems - Characteristics and comparisons.* Renewable & Sustainable Energy Reviews, 2008. **12**(5): p. 1221-1250.

4. Carmo, M., et al., *A comprehensive review on PEM water electrolysis.* International journal of hydrogen energy, 2013. **38**(12): p. 4901-4934.

5. Fang, Q., L. Blum, and N.H. Menzler, *Performance and Degradation of Solid Oxide Electrolysis Cells in Stack.* Journal of the Electrochemical Society, 2015. **162**(8): p. F907-F912.

6. Sun, X., et al., *Life Time Performance Characterization of Solid Oxide Electrolysis Cells for Hydrogen Production.* ECS Transactions, 2015. **68**(1): p. 3359-3368.

7. Sharma, V.I. and B. Yildiz, *Degradation Mechanism in La0.8Sr0.2CoO3 as Contact Layer on the Solid Oxide Electrolysis Cell Anode.* Journal of the Electrochemical Society, 2010. **157**(3): p. B441-B448.

8. Kim, J., et al., *Degradation mechanism of electrolyte and air electrode in solid oxide electrolysis cells operating at high polarization.* International Journal of Hydrogen Energy, 2013. **38**(3): p. 1225-1235.

9. Tao, Y.K., S.D. Ebbesen, and M.B. Mogensen, *Degradation of solid oxide cells during co-electrolysis of steam and carbon dioxide at high current densities.* Journal of Power Sources, 2016. **328**: p. 452-462.

10. Lay-Grindler, E., et al., *Degradation study of the La0. 6Sr0. 4Co0. 2Fe0. 8O3 solid oxide electrolysis cell (SOEC) anode after high temperature electrolysis operation.* ECS Transactions, 2013. **57**(1): p. 3177-3187.

11. Virkar, A.V., *Mechanism of oxygen electrode delamination in solid oxide electrolyzer cells.* International Journal of Hydrogen Energy, 2010. **35**(18): p. 9527-9543.

12. The, D., et al., *Microstructural comparison of solid oxide electrolyser cells operated for 6100 h and 9000 h.* Journal of Power Sources, 2015. **275**: p. 901-911.

13. Mocoteguy, P. and A. Brisse, *A review and comprehensive analysis of degradation mechanisms of solid oxide electrolysis cells.* International Journal of Hydrogen Energy, 2013. **38**(36): p. 15887-15902.

14. Knibbe, R., et al., *Solid Oxide Electrolysis Cells: Degradation at High Current Densities.* Journal of the Electrochemical Society, 2010. **157**(8): p. B1209-B1217.

15. Keane, M., et al., *LSM-YSZ interactions and anode delamination in solid oxide electrolysis cells.* International Journal of Hydrogen Energy, 2012. **37**(22): p. 16776-16785.

16. Orazem, M.E. and B. Tribollet, *Electrochemical impedance spectroscopy*. Vol. 48. 2011: John Wiley & Sons.

17. Schichlein, H., et al., *Deconvolution of electrochemical impedance spectra for the identification of electrode reaction mechanisms in solid oxide fuel cells.* Journal of Applied Electrochemistry, 2002. **32**(8): p. 875-882.

18. Leonide, A., et al., *Evaluation and modeling of the cell resistance in anode-supported solid oxide fuel cells.* Journal of the Electrochemical Society, 2008. **155**(1): p. B36-B41.

19. Endler-Schuck, C., et al., *Performance analysis of mixed ionic–electronic conducting cathodes in anode supported cells.* Journal of Power Sources, 2011. **196**(17): p. 7257-7262.

20. Ivers-Tiffee, E. and A. Weber, *Evaluation of electrochemical impedance spectra by the distribution of relaxation times.* Journal of the Ceramic Society of Japan, 2017. **125**(4): p. 193-201.

21. Fergus, J., et al., *Solid oxide fuel cells: materials properties and performance.* 2016: CRC press.

22. Kharton, V.V., F.M.B. Marques, and A. Atkinson, *Transport properties of solid oxide electrolyte ceramics: a brief review.* Solid State Ionics, 2004. **174**(1): p. 135-149.

23. Etsell, T. and S.N. Flengas, *Electrical properties of solid oxide electrolytes.* Chemical Reviews, 1970. **70**(3): p. 339-376.

24. Badwal, S. and F. Ciacchi, *Oxygen-ion conducting electrolyte materials for solid oxide fuel cells.* Ionics, 2000. **6**(1-2): p. 1-21.

25. Omar, S., W.B. Najib, and N. Bonanos, *Conductivity ageing studies on 1M10ScSZ (M4+= Ce, Hf).* Solid State Ionics, 2011. **189**(1): p. 100-106.

26. Subramanian, M., G. Aravamudan, and G.S. Rao, *Oxide pyrochlores—a review.* Progress in Solid State Chemistry, 1983. **15**(2): p. 55-143.

27. Kramer, S. and H. Tuller, *A novel titanate-based oxygen ion conductor: Gd2Ti2O7.* Solid State Ionics, 1995. **82**(1-2): p. 15-23.

28. Nomura, K. and S. Tanase, *Electrical conduction behavior in (La0. 9Sr0. 1) MIIIO3− δ (MIII= Al, Ga, Sc, In, and Lu) perovskites.* Solid State Ionics, 1997. **98**(3-4): p. 229-236.

29. Kao, W.-X., et al., *Fabrication and evaluation of the electrochemical performance of the anode-supported solid oxide fuel cell with the composite cathode of La0. 8Sr0. 2MnO3− δ–Gadolinia-doped ceria oxide/La0. 8Sr0. 2MnO3− δ.* Journal of Power Sources, 2010. **195**(19): p. 6468-6472.

30. Li, S., et al., *A study of (Ba0. 5Sr0. 5) 1− xSmxCo0. 8Fe0. 2O3− δ as a cathode material for IT-SOFCs.* Journal of alloys and compounds, 2006. **426**(1-2): p. 408-414.

31. van Veen, A.C., et al., *Studies on the performance stability of mixed conducting BSCFO membranes in medium temperature oxygen permeation.* Chemical Communications, 2003(1): p. 32-33.

32. Jiang, S.P. and W. Wang, *Novel structured mixed ionic and electronic conducting cathodes of solid oxide fuel cells.* Solid State Ionics, 2005. **176**(15-16): p. 1351-1357.

33. Petric, A., P. Huang, and F. Tietz, *Evaluation of La–Sr–Co–Fe–O perovskites for solid oxide fuel cells and gas separation membranes.* Solid State Ionics, 2000. **135**(1-4): p. 719-725.

34. Wincewicz, K.C. and J.S. Cooper, *Taxonomies of SOFC material and manufacturing alternatives.* Journal of Power Sources, 2005. **140**(2): p. 280-296.

35. Spacil, H.S., *Electrical device including nickel-containing stabilized zirconia electrode*. 1970, Google Patents.

36. Singhal, S.C. and K. Kendall, *High-temperature solid oxide fuel cells: fundamentals, design and applications*. 2003: Elsevier.

37. Hagen, A., et al., *Degradation of anode supported SOFCs as a function of temperature and current load.* Journal of the Electrochemical Society, 2006. **153**(6): p. A1165-A1171.

38. Holzer, L., et al., *Microstructure degradation of cermet anodes for solid oxide fuel cells: Quantification of nickel grain growth in dry and in humid atmospheres.* Journal of Power Sources, 2011. **196**(3): p. 1279-1294.

39. Nelson, G.J., et al., *Three-dimensional microstructural changes in the Ni–YSZ solid oxide fuel cell anode during operation.* Acta Materialia, 2012. **60**(8): p. 3491-3500.

40. Blum, L., et al., *SOC Development at Forschungszentrum Jülich.* ECS Transactions, 2017. **78**(1): p. 1791-1804.

41. Cassidy, M., G. Lindsay, and K. Kendall, *The reduction of nickel zirconia cermet anodes and the effects on supported thin electrolytes.* Journal of Power Sources, 1996. **61**(1-2): p. 189-192.

42. Larrain, D. and D. Favrat, *Simulation of SOFC stack and repeat elements including interconnect degradation and anode reoxidation risk.* Journal of Power Sources, 2006. **161**(1): p. 392-403.

43. Sarantaridis, D. and A. Atkinson, *Redox Cycling of Ni‐Based Solid Oxide Fuel Cell Anodes: A Review.* Fuel cells, 2007. **7**(3): p. 246-258.

44. Iwata, T., *Characterization of ni‐ysz anode degradation for substrate‐type solid oxide fuel cells.* Journal of the Electrochemical Society, 1996. **143**(5): p. 1521-1525.

45. Nikooyeh, K., et al., *Effect of hydrogen on carbon formation on Ni/YSZ composites exposed to methane.* Applied Catalysis A: General, 2008. **347**(1): p. 106-111.

46. Rasmussen, J.F. and A. Hagen, *The effect of H2S on the performance of Ni–YSZ anodes in solid oxide fuel cells.* Journal of Power Sources, 2009. **191**(2): p. 534-541.

47. Blum, L., et al., *Anode‐Supported Solid Oxide Fuel Cell Achieves 70 000 Hours of Continuous Operation.* Energy Technology, 2016. **4**(8): p. 939-942.

48. Menzler, N.H., D. Sebold, and O. Guillon, *Post-test characterization of a solid oxide fuel cell stack operated for more than 30,000 hours: The cell.* Journal of Power Sources, 2018. **374**: p. 69-76.

49. Fang, Q., et al., *Solid Oxide Electrolyzer Stack with 20,000 h of Operation.* ECS Transactions, 2017. **78**(1): p. 2885-2893.

50. Fang, Q., et al., *Electrochemical Performance and Preliminary Post-Mortem Analysis of a Solid Oxide Cell Stack with 20,000 h of Operation.* Journal of The Electrochemical Society, 2018. **165**(2): p. F38-F45.

51. Costa-Nunes, O., R.J. Gorte, and J.M. Vohs, *Comparison of the performance of Cu–CeO2–YSZ and Ni–YSZ composite SOFC anodes with H2, CO, and syngas.* Journal of power sources, 2005. **141**(2): p. 241-249.

52. Gorte, R.J., et al., *Anodes for direct oxidation of dry hydrocarbons in a solid‐oxide fuel cell.* Advanced materials, 2000. **12**(19): p. 1465-1469.

53. Hui, S. and A. Petric, *Evaluation of yttrium-doped SrTiO3 as an anode for solid oxide fuel cells.* Journal of the European Ceramic Society, 2002. **22**(9-10): p. 1673-1681.

54. Fagg, D., et al., *The stability and mixed conductivity in La and Fe doped SrTiO3 in the search for potential SOFC anode materials.* Journal of the European ceramic Society, 2001. **21**(10-11): p. 1831-1835.

55. Marina, O.A., N.L. Canfield, and J.W. Stevenson, *Thermal, electrical, and electrocatalytical properties of lanthanum-doped strontium titanate.* Solid State Ionics, 2002. **149**(1-2): p. 21-28.

56. Ruiz-Morales, J.C., et al., *Disruption of extended defects in solid oxide fuel cell anodes for methane oxidation.* Nature, 2006. **439**(7076): p. 568.

57. Tao, S. and J.T. Irvine, *Discovery and characterization of novel oxide anodes for solid oxide fuel cells.* The Chemical Record, 2004. **4**(2): p. 83-95.

58. ZHANG, X. and Q. ZHONG, *Preparation and characterization of La_ (0.7) Sr_ (0.3) Cr_ (1-x) Fe_xO_ (3-δ) anode catalyst with sulfur tolerance for SOFC.* Chemical Industry and Engineering Progress, 2009. **5**: p. 020.

59. Yokokawa, H., et al., *Thermodynamic and kinetic considerations on degradations in solid oxide fuel cell cathodes.* Journal of Alloys and Compounds, 2008. **452**(1): p. 41-47.

60. Song, J.-H., et al., *The Effect of Fabrication Conditions for GDC Buffer Layer on Electrochemical Performance of Solid Oxide Fuel Cells.* Nano-Micro Letters, 2013. **5**(3): p. 151-158.

61. Mai, A., et al., *Ferrite-based perovskites as cathode materials for anode-supported solid oxide fuel cells: Part II. Influence of the CGO interlayer.* Solid state ionics, 2006. **177**(19-25): p. 2103-2107.

62. Kleinlogel, C. and L. Gauckler, *Sintering and properties of nanosized ceria solid solutions.* Solid State Ionics, 2000. **135**(1-4): p. 567-573.

63. Wang, F., et al., *Sr and Zr diffusion in LSCF/10GDC/8YSZ triplets for solid oxide fuel cells (SOFCs).* Journal of Power Sources, 2014. **258**: p. 281-289.

64. Szász, J., et al., *High-performance cathode/electrolyte interfaces for SOFC.* ECS transactions, 2015. **68**(1): p. 763-771.

65. Szász, J., et al., *Nature and functionality of oxygen/cathode/electrolyte-interfaces in SOFCs.* ECS Transactions, 2015. **66**(2): p. 79-87.

66. Yokokawa, H., *Overview of intermediate-temperature solid oxide fuel cells*, in *Perovskite Oxide for Solid Oxide Fuel Cells*. 2009, Springer. p. 17-43.

67. Zhu, W.Z. and S. Deevi, *Development of interconnect materials for solid oxide fuel cells.* Materials Science and Engineering: A, 2003. **348**(1-2): p. 227-243.

68. Hilpert, K., et al., *Defect formation and mechanical stability of perovskites based on LaCrO3 for solid oxide fuel cells (SOFC).* Journal of the European Ceramic Society, 2003. **23**(16): p. 3009-3020.

69. Yasuda, I. and M. Hishinuma, *Electrical conductivity and chemical diffusion coefficient of Sr-doped lanthanum chromites.* Solid State Ionics, 1995. **80**(1-2): p. 141-150.

70. Tietz, F., *Thermal expansion of SOFC materials.* Ionics, 1999. **5**(1-2): p. 129-139.

71. Yang, Z., *Recent advances in metallic interconnects for solid oxide fuel cells.* International Materials Reviews, 2008. **53**(1): p. 39-54.

72. Yang, Z., et al., *Selection and evaluation of heat-resistant alloys for SOFC interconnect applications.* Journal of the Electrochemical Society, 2003. **150**(9): p. A1188-A1201.

73.   Piccardo, P., et al., *ASR evaluation of different kinds of coatings on a ferritic stainless steel as SOFC interconnects.* Surface and Coatings Technology, 2007. **202**(4): p. 1221-1225.

74.   Quadakkers, W., et al., *Metallic interconnectors for solid oxide fuel cells–a review.* Materials at high temperatures, 2003. **20**(2): p. 115-127.

75.   Gannon, P.E., et al., *High-temperature oxidation resistance and surface electrical conductivity of stainless steels with filtered arc Cr–Al–N multilayer and/or superlattice coatings.* Surface and Coatings Technology, 2004. **188**: p. 55-61.

76.   Orlovskaya, N., et al., *Structural Characterization of Lanthanum Chromite Perovskite Coating Deposited by Magnetron Sputtering on an Iron‐Based Chromium‐Containing Alloy as a Promising Interconnect Material for SOFCs.* Journal of the American Ceramic Society, 2004. **87**(10): p. 1981-1987.

77.   Larring, Y. and T. Norby, *Spinel and Perovskite Functional Layers Between Plansee Metallic Interconnect (Cr‐5 wt% Fe‐1 wt% Y 2 O 3) and Ceramic (La0. 85Sr0. 15) 0.91 MnO3 Cathode Materials for Solid Oxide Fuel Cells.* Journal of the Electrochemical Society, 2000. **147**(9): p. 3251-3256.

78.   Yang, Z., et al., *Conductive protection layers on oxidation resistant alloys for SOFC interconnect applications.* Surface and Coatings Technology, 2006. **201**(7): p. 4476-4483.

79.   Blum, L., et al., *Recent results in Jülich solid oxide fuel cell technology development.* Journal of Power Sources, 2013. **241**: p. 477-485.

80.   Blum, L., et al., *SOFC stack and system development at Forschungszentrum Jülich.* Journal of The Electrochemical Society, 2015. **162**(10): p. F1199-F1205.

81.   Malzbender, J., et al., *Component interactions after long-term operation of an SOFC stack with LSM cathode.* Journal of power sources, 2012. **201**: p. 196-203.

82.   Nielsen, K., et al., *Glass composite seals for SOFC application.* Journal of the European Ceramic Society, 2007. **27**(2-3): p. 1817-1822.

83.   Smeacetto, F., et al., *Glass–ceramic seal to join Crofer 22 APU alloy to YSZ ceramic in planar SOFCs.* Journal of the European Ceramic Society, 2008. **28**(1): p. 61-68.

84.   Laosiripojana, N., et al., *Reviews on solid oxide fuel cell technology.* Engineering Journal (Eng. J.), 2009. **13**(1): p. 65-84.

85.   Weil, K.S., et al., *Alternative planar SOFC sealing concepts.* Fuel Cells Bulletin, 2004. **2004**(5): p. 11-16.

86.   Fergus, J.W., *Sealants for solid oxide fuel cells.* Journal of Power Sources, 2005. **147**(1-2): p. 46-57.

87.   Duquette, J. and A. Petric, *Silver wire seal design for planar solid oxide fuel cell stack.* Journal of power sources, 2004. **137**(1): p. 71-75.

88.   Chou, Y.-S. and J.W. Stevenson, *Phlogopite mica-based compressive seals for solid oxide fuel cells: effect of mica thickness.* Journal of Power Sources, 2003. **124**(2): p. 473-478.

89.   Chou, Y.-S. and J.W. Stevenson, *Mid-term stability of novel mica-based compressive seals for solid oxide fuel cells.* Journal of power Sources, 2003. **115**(2): p. 274-278.

90.   Meinhardt, K.D., et al., *Glass-ceramic joint and method of joining.* 2003, Google Patents.

91.   Zheng, R., et al., *SiO2–CaO–B2O3–Al2O3 ceramic glaze as sealant for planar ITSOFC.* Journal of Power Sources, 2004. **128**(2): p. 165-172.

92.   Lara, C., et al., *Sintering of glasses in the system RO–Al2O3–BaO–SiO2 (R= Ca, Mg, Zn) studied by hot-stage microscopy.* Solid State Ionics, 2004. **170**(3-4): p. 201-208.

93.   Larsen, P. and P. James, *Chemical stability of MgO/CaO/Cr2O3–Al2O3–B2O3– phosphate glasses in solid oxide fuel cell environment.* Journal of materials science, 1998. **33**(10): p. 2499-2507.

94.   Sohn, S.B., et al., *Suitable Glass‐Ceramic Sealant for Planar Solid‐Oxide Fuel Cells.* Journal of the American Ceramic Society, 2004. **87**(2): p. 254-260.

95.   Lessing, P.A., *A review of sealing technologies applicable to solid oxide electrolysis cells.* Journal of Materials Science, 2007. **42**(10): p. 3465-3476.

96.   Singhal, S.C. and M. Dokiya. *Solid Oxide Fuel Cells (SOFC VI): Proceedings of the Sixth International Symposium.* 1999. The Electrochemical Society.

97.   Larsen, P., et al. *Stacking of planar SOFCs.* in *Proceedings of the Fourth International Symposium on Solid Oxide Fuel Cells (SOFC-IV).* 1995. The Electrochemical Society.

98.   Gross, S.M., et al., *Joining properties of a composite glass-ceramic sealant.* Fuel Cells Bulletin, 2006. **2006**(9): p. 12-15.

99.   Mahapatra, M.K. and K. Lu, *Glass-based seals for solid oxide fuel and electrolyzer cells – A review.* Materials Science and Engineering: R: Reports, 2010. **67**(5): p. 65-85.

100.   Brendt, J., et al., *The influence of ZnO and V2O5 on the crystallization behavior of BaO-CaO-SiO2 glass-ceramic sealants.* Journal of Non-Crystalline Solids, 2018.

101.   Wu, W., et al., *Effect of contact method between interconnects and electrodes on area specific resistance in planar solid oxide fuel cells.* Fuel Cells, 2013. **13**(5): p. 743-750.

102.   Ilea, C.S., R. Ihringer, and I. Warnhus, *Short-stack testing of novel anode-supported SOFC–2R-Cell.*

103.   Seabaugh, M.M., et al., *Materials Development for SOFC Applications.* ECS Transactions, 2009. **25**(2): p. 619-628.

104.   Wood, A., Z. Tang, and T. Joia, *Electrically conductive fuel cell contact materials.* 2007, Google Patents.

105.   Sarikaya, A., V. Petrovsky, and F. Dogan, *Silver composites as highly stable cathode current collectors for solid oxide fuel cells.* Journal of Materials Research, 2012. **27**(15): p. 2024-2029.

106.   Guo, Y., et al., *Significant impact of the current collection material and method on the performance of Ba0. 5Sr0. 5Co0. 8Fe0. 2O3− δ electrodes in solid oxide fuel cells.* Journal of Power Sources, 2011. **196**(13): p. 5511-5519.

107.   Mahato, N., et al., *Progress in material selection for solid oxide fuel cell technology: A review.* Progress in Materials Science, 2015. **72**: p. 141-337.

108.   Tietz, F., et al., *Survey of the quasi-ternary system La0. 8Sr0. 2MnO3–La0. 8Sr0. 2CoO3–La0. 8Sr0. 2FeO3.* Progress in solid state chemistry, 2007. **35**(2-4): p. 539-543.

109.   Tietz, F., et al., *Electrical conductivity and thermal expansion of La0. 8Sr0. 2 (Mn, Fe, Co) O3-δ perovskites.* Solid State Ionics, 2006. **177**(19-25): p. 1753-1756.

110.   Chiba, R., F. Yoshimura, and Y. Sakurai, *An investigation of LaNi1− xFexO3 as a cathode material for solid oxide fuel cells.* Solid State Ionics, 1999. **124**(3-4): p. 281-288.

111.   Wang, F., et al., *LaCo0. 6Ni0. 4O3− δ as cathode contact material for intermediate temperature solid oxide fuel cells.* International Journal of Hydrogen Energy, 2013. **38**(1): p. 646-651.

112.   Morán-Ruiz, A., et al., *Effects of using (La0. 8Sr0. 2) 0.95 Fe0. 6Mn0. 3Co0. 1O3 (LSFMC), LaNi0. 6Fe0. 4O3− δ (LNF) and LaNi0. 6Co0. 4O3− δ (LNC) as contact materials on solid oxide fuel cells.* Journal of Power Sources, 2014. **248**: p. 1067-1076.

113.   Dekker, N., et al. *Evaluation of interconnect alloys and cathode contact coatings for SOFC stacks*. in *Procs. 6th European SOFC Forum*. 2004.

114.   Tietz, F., A. Schmidt, and M. Zahid, *Investigation of the quasi-ternary system LaMnO3–LaCoO3–"LaCuO3"—I: the series La (Mn0. 5Co0. 5) 1− xCuxO3− δ.* Journal of Solid State Chemistry, 2004. **177**(3): p. 745-751.

115.   Gindorf, C., L. Singheiser, and K. Hilpert, *Chromium vaporisation from Fe, Cr base alloys used as interconnect in fuel cells.* steel research international, 2001. **72**(11-12): p. 528-533.

116. Yang, Z., G. Xia, and J.W. Stevenson, *Mn1. 5Co1. 5 O 4 Spinel Protection Layers on Ferritic Stainless Steels for SOFC Interconnect Applications.* Electrochemical and Solid-State Letters, 2005. **8**(3): p. A168-A170.

117. Stanislowski, M., et al., *Reduction of chromium vaporization from SOFC interconnectors by highly effective coatings.* Journal of Power Sources, 2007. **164**(2): p. 578-589.

118. Wang, K., Y. Liu, and J.W. Fergus, *Interactions between SOFC interconnect coating materials and chromia.* Journal of the American Ceramic Society, 2011. **94**(12): p. 4490-4495.

119. Yang, Z., et al., *Ce-modified (Mn, Co) 3O4 spinel coatings on ferritic stainless steels for SOFC interconnect applications.* Electrochemical and Solid-State Letters, 2008. **11**(8): p. B140-B143.

120. Tanasini, P., et al., *Experimental and theoretical investigation of degradation mechanisms by particle coarsening in SOFC electrodes.* Fuel Cells, 2009. **9**(5): p. 740-752.

121. Faes, A., et al., *Nickel–zirconia anode degradation and triple phase boundary quantification from microstructural analysis.* Fuel cells, 2009. **9**(6): p. 841-851.

122. Simwonis, D., F. Tietz, and D. Stöver, *Nickel coarsening in annealed Ni/8YSZ anode substrates for solid oxide fuel cells.* Solid State Ionics, 2000. **132**(3): p. 241-251.

123. Vassen, R., D. Simwonis, and D. Stöver, *Modelling of the agglomeration of Ni-particles in anodes of solid oxide fuel cells.* Journal of materials science, 2001. **36**(1): p. 147-151.

124. Pecho, O.M., et al., *3D microstructure effects in Ni-YSZ Anodes: Prediction of effective transport properties and optimization of redox stability.* Materials, 2015. **8**(9): p. 5554-5585.

125. Holzer, L., et al., *Quantitative relationships between composition, particle size, triple phase boundary length and surface area in nickel-cermet anodes for Solid Oxide Fuel Cells.* Journal of Power Sources, 2011. **196**(17): p. 7076-7089.

126. Matsui, T., et al., *Performance deterioration of Ni–YSZ anode induced by electrochemically generated steam in solid oxide fuel cells.* Journal of The Electrochemical Society, 2010. **157**(5): p. B776-B781.

127. Hauch, A., et al., *Solid oxide electrolysis cells: microstructure and degradation of the Ni/yttria-stabilized zirconia electrode.* Journal of the Electrochemical Society, 2008. **155**(11): p. B1184-B1193.

128. Hauch, A., et al., *Performance and durability of solid oxide electrolysis cells.* Journal of the Electrochemical Society, 2006. **153**(9): p. A1741-A1747.

129. Ramos, T., K. Thydén, and M. Mogensen, *Electrochemical characterization of Ni/(Sc) YSZ electrodes.* ECS transactions, 2010. **28**(11): p. 123-139.

130. Koh, J.-H., et al., *Carbon deposition and cell performance of Ni-YSZ anode support SOFC with methane fuel.* Solid State Ionics, 2002. **149**(3): p. 157-166.

131. Ebbesen, S.D. and M. Mogensen, *Electrolysis of carbon dioxide in solid oxide electrolysis cells.* Journal of Power Sources, 2009. **193**(1): p. 349-358.

132. Ebbesen, S.D., C. Graves, and M. Mogensen, *Production of synthetic fuels by co-electrolysis of steam and carbon dioxide.* International Journal of Green Energy, 2009. **6**(6): p. 646-660.

133. Ebbesen, S.D., et al., *Poisoning of solid oxide electrolysis cells by impurities.* Journal of The Electrochemical Society, 2010. **157**(10): p. B1419-B1429.

134. Rasmussen, J.F. and A. Hagen, *The effect of H 2 S on the performance of Ni–YSZ anodes in solid oxide fuel cells.* Journal of Power Sources, 2009. **191**(2): p. 534-541.

135. Matsuzaki, Y. and I. Yasuda, *The poisoning effect of sulfur-containing impurity gas on a SOFC anode: Part I. Dependence on temperature, time, and impurity concentration.* Solid State Ionics, 2000. **132**(3): p. 261-269.

136.   Hagen, A., J.F. Rasmussen, and K. Thydén, *Durability of solid oxide fuel cells using sulfur containing fuels.* Journal of Power Sources, 2011. **196**(17): p. 7271-7276.

137.   Jiang, S.P., *Development of lanthanum strontium manganite perovskite cathode materials of solid oxide fuel cells: a review.* Journal of Materials Science, 2008. **43**(21): p. 6799-6833.

138.   Liu, Y.-L., et al., *Microstructural studies on degradation of interface between LSM–YSZ cathode and YSZ electrolyte in SOFCs.* Solid State Ionics, 2009. **180**(23): p. 1298-1304.

139.   Chen, M., B. Hallstedt, and L.J. Gauckler, *Thermodynamic modeling of phase equilibria in the Mn–Y–Zr–O system.* Solid State Ionics, 2005. **176**(15): p. 1457-1464.

140.   Chen, M., et al., *LSM–YSZ reactions in different atmospheres.* Fuel Cells, 2009. **9**(6): p. 833-840.

141.   Hilpert, K., et al., *Chromium vapor species over solid oxide fuel cell interconnect materials and their potential for degradation processes.* Journal of the Electrochemical Society, 1996. **143**(11): p. 3642-3647.

142.   Badwal, S., et al., *Interaction between chromia forming alloy interconnects and air electrode of solid oxide fuel cells.* Solid State Ionics, 1997. **99**(3-4): p. 297-310.

143.   Baumann, F., et al., *Ba 0.5 Sr 0.5 Co 0.8 Fe 0.2 O 3− δ thin film microelectrodes investigated by impedance spectroscopy.* Solid State Ionics, 2006. **177**(35): p. 3187-3191.

144.   Sase, M., et al., *Interfacial reaction and electrochemical properties of dense (La, Sr) CoO 3− δ cathode on YSZ (1 0 0).* Journal of Physics and Chemistry of Solids, 2005. **66**(2): p. 343-348.

145.   Dieterle, L., et al., *Structural and chemical properties of nanocrystalline La0. 5Sr0. 5CoO3− δ layers on yttria-stabilized zirconia analyzed by transmission electron microscopy.* Journal of materials science, 2008. **43**(9): p. 3135-3143.

146. Fagg, D., S. Fray, and J. Irvine, *Reduced magnesium titanate electrodes for solid oxide fuel cells.* Solid State Ionics, 1994. **72**: p. 235-239.

147. Tsoga, A., et al., *Gadolinia-doped ceria and yttria stabilized zirconia interfaces: regarding their application for SOFC technology.* Acta Materialia, 2000. **48**(18-19): p. 4709-4714.

148. Tsoga, A., A. Naoumidis, and D. Stöver, *Total electrical conductivity and defect structure of ZrO2–CeO2–Y2O3–Gd2O3 solid solutions.* Solid state ionics, 2000. **135**(1-4): p. 403-409.

149. Knibbe, R., et al., *Cathode–electrolyte interfaces with CGO barrier layers in SOFC.* Journal of the American Ceramic Society, 2010. **93**(9): p. 2877-2883.

150. Scott, H., *Phase relationships in the zirconia-yttria system.* Journal of Materials Science, 1975. **10**(9): p. 1527-1535.

151. Badwal, S., *Zirconia-based solid electrolytes: microstructure, stability and ionic conductivity.* Solid State Ionics, 1992. **52**(1-3): p. 23-32.

152. Tsoga, A., et al., *Performance of a double-layer CGO/YSZ electrolyte for solid oxide fuel cells.* Ionics, 1998. **4**(3-4): p. 234-240.

153. Sammes, N., G. Tompsett, and Z. Cai, *The chemical reaction between ceria and fully stabilised zirconia.* Solid State Ionics, 1999. **121**(1-4): p. 121-125.

154. Wu, J. and X. Liu, *Recent development of SOFC metallic interconnect.* Journal of materials science & technology, 2010. **26**(4): p. 293-305.

155. Garcia-Fresnillo, L., et al., *Influence of Alloying Elements on the Behavior of Different Ferritic Steels as Candidate Materials for SOFC Interconnect.* Oxidation of Metals, 2018. **89**(1-2): p. 61-80.

156. Sun, X., et al., *Durability of solid oxide electrolysis cells for syngas production.* Journal of The Electrochemical Society, 2013. **160**(9): p. F1074-F1080.

157. Kim, S.-D., et al., *The effect of gas compositions on the performance and durability of solid oxide electrolysis cells.* international journal of hydrogen energy, 2013. **38**(16): p. 6569-6576.

158. Hauch, A., et al., *Silica segregation in the Ni ∕ YSZ electrode.* Journal of the Electrochemical Society, 2007. **154**(7): p. A619-A626.

159. Shi, Y., et al., *Experimental characterization and modeling of the electrochemical reduction of CO2 in solid oxide electrolysis cells.* Electrochimica acta, 2013. **88**: p. 644-653.

160. Wang, W., et al., *GDC-impregnated Ni anodes for direct utilization of methane in solid oxide fuel cells.* Journal of Power Sources, 2006. **159**(1): p. 68-72.

161. MOMMA, A., et al., *Polarization behavior of high temperature solid oxide electrolysis cells (SOEC).* Journal of the Ceramic Society of Japan, 1997. **105**(1221): p. 369-373.

162. Brichzin, V., et al., *The geometry dependence of the polarization resistance of Sr-doped LaMnO3 microelectrodes on yttria-stabilized zirconia.* Solid State Ionics, 2002. **152**: p. 499-507.

163. Schefold, J., A. Brisse, and F. Tietz, *Nine thousand hours of operation of a solid oxide cell in steam electrolysis mode.* Journal of The Electrochemical Society, 2011. **159**(2): p. A137-A144.

164. Elangovan, S., et al., *Materials for solid oxide electrolysis cells.* ECS Transactions, 2011. **35**(1): p. 2875-2882.

165. Kim, S.J. and G.M. Choi, *Stability of LSCF electrode with GDC interlayer in YSZ-based solid oxide electrolysis cell.* Solid State Ionics, 2014. **262**: p. 303-306.

166. Hjalmarsson, P., et al., *Durability of high performance Ni–yttria stabilized zirconia supported solid oxide electrolysis cells at high current density.* Journal of Power Sources, 2014. **262**: p. 316-322.

167. Chen, K., et al., *Chromium deposition and poisoning of La0. 8Sr0. 2MnO3 oxygen electrodes of solid oxide electrolysis cells.* Faraday discussions, 2015. **182**: p. 457-476.

168. Huber, A.-K., et al., *In situ study of activation and de-activation of LSM fuel cell cathodes–Electrochemistry and surface analysis of thin-film electrodes.* Journal of catalysis, 2012. **294**: p. 79-88.

169. Wang, W. and S.P. Jiang, *A mechanistic study on the activation process of (La, Sr) MnO3 electrodes of solid oxide fuel cells.* Solid State Ionics, 2006. **177**(15-16): p. 1361-1369.

170. Wei, B., et al., *Chromium deposition and poisoning at La 0.6 Sr 0.4 Co 0.2 Fe 0.8 O 3− δ oxygen electrodes of solid oxide electrolysis cells.* Physical Chemistry Chemical Physics, 2015. **17**(3): p. 1601-1609.

171. Laguna-Bercero, M., et al., *Electrolyte degradation in anode supported microtubular yttria stabilized zirconia-based solid oxide steam electrolysis cells at high voltages of operation.* Journal of Power Sources, 2011. **196**(21): p. 8942-8947.

172. Jensen, S.H., et al., *A method to separate process contributions in impedance spectra by variation of test conditions.* Journal of the Electrochemical Society, 2007. **154**(12): p. B1325-B1330.

173. Schoenleber, M. and E. Ivers-Tiffée, *Approximability of impedance spectra by RC elements and implications for impedance analysis.* Electrochemistry Communications, 2015. **58**: p. 15-19.

174. Schichlein, H., et al., *System identification: a new modelling approach for SOFC single cells.* ECS Proceedings Volumes, 1999. **1999**: p. 1069-1077.

175. Schäfer, H., et al., *Novel approach to the analysis of broadband dielectric spectra.* Physical review letters, 1996. **76**(12): p. 2177.

176. Weber, A., et al., *Sulfur Poisoning of Anode‐Supported SOFCs under Reformate Operation.* Fuel Cells, 2013. **13**(4): p. 487-493.

177. Kornely, M., et al., *Degradation of a High Performance SOFC Cathode by Cr‐Poisoning at OCV‐Conditions.* Fuel Cells, 2013. **13**(4): p. 506-510.

178. Hoerlein, M.P., et al., *Systematic Parameter Study on the Influence of Humidification and Current Density on SOEC Degradation.* ECS Transactions, 2015. **68**(1): p. 3553-3561.

179. Frey, C.E., et al., *A Detailed Post Mortem Analysis of Solid Oxide Electrolyzer Cells after Long-Term Stack Operation.* Journal of The Electrochemical Society, 2018. **165**(5): p. F357-F364.

180. Thompson, A.R., et al., *Electrochemical Impedance Spectroscopy Data from Solid Oxide Cells Undergoing Co-Electrolysis: The Influence of Rig Inductance.* ECS Transactions, 2015. **68**(1): p. 3417-3427.

181. Raikova, G., et al., *Inductance correction in impedance studies of solid oxide fuel cells.* Bulg Chem Comm, 2009. **41**(2): p. 199-206.

182. Boigues Muñoz, C., et al., *More accurate macro-models of solid oxide fuel cells through electrochemical and microstructural parameter estimation – Part I: Experimentation.* Journal of Power Sources, 2015. **294**: p. 658-668.

183. Mosbæk, R.R., et al., *Electrochemical characterization and degradation analysis of large SOFC stacks by impedance spectroscopy.* Fuel Cells, 2013. **13**(4): p. 605-611.

184. Weber, A., et al. *Impedance spectroscopy as a diagnosis tool for SOFC stacks and systems*. in *International symposium on diagnostics tools fuel cell technologies*. 2009.

185. Menzler, N.H., et al., *Materials and manufacturing technologies for solid oxide fuel cells.* Journal of Materials Science, 2010. **45**(12): p. 3109-3135.

186. Blum, L., et al., *Investigation of solid oxide fuel cell sealing behavior under stack relevant conditions at Forschungszentrum Julich.* Journal of Power Sources, 2011. **196**(17): p. 7175-7181.

187. Fang, Q.P., et al., *SOFC stack performance under high fuel utilization.* International Journal of Hydrogen Energy, 2015. **40**(2): p. 1128-1136.

188. Menzler, N.H., et al., *Sol-Gel Thin-Film Electrolyte Anode-Supported SOFC - From Layer Development to Stack Testing.* Solid Oxide Fuel Cells 13 (Sofc-Xiii), 2013. **57**(1): p. 959-967.

189. Saccoccio, M., et al., *Optimal regularization in distribution of relaxation times applied to electrochemical impedance spectroscopy: Ridge and lasso regression methods-a theoretical and experimental study.* Electrochimica Acta, 2014. **147**: p. 470-482.

190. Ciucci, F. and C. Chen, *Analysis of electrochemical impedance spectroscopy data using the distribution of relaxation times: a Bayesian and hierarchical Bayesian approach.* Electrochimica Acta, 2015. **167**: p. 439-454.

191. Wan, T.H., et al., *Influence of the discretization methods on the distribution of relaxation times deconvolution: implementing radial basis functions with DRTtools.* Electrochimica Acta, 2015. **184**: p. 483-499.

192. Ehm, W., et al., *The evaluation of electrochemical impedance spectra using a modified logarithmic Hilbert transform.* ACH MODELS IN CHEMISTRY, 2000. **137**(2/3): p. 145-158.

193. Kim, J.W., et al., *Polarization effects in intermediate temperature, anode‐supported solid oxide fuel cells.* Journal of the Electrochemical Society, 1999. **146**(1): p. 69-78.

194. Jiang, S. and S. Badwal, *Hydrogen Oxidation at the Nickel and Platinum Electrodes on Yttria‐Tetragonal Zirconia Electrolyte.* Journal of the Electrochemical Society, 1997. **144**(11): p. 3777-3784.

195. Benndorf, C., et al., *H2O interaction with Ni (110): auto-catalytic decomposition in the temperature range from 400 to 550 K.* Applications of Surface Science, 1982. **11**: p. 803-811.

196. Mizusaki, J., et al., *Kinetic studies of the reaction at the nickel pattern electrode on YSZ in H2   H2O atmospheres.* Solid State Ionics, 1994. **70**: p. 52-58.

197. Hayd, J. and E. Ivers-Tiffée, *Detailed Electrochemical Study on Nanoscaled La0. 6Sr0. 4CoO3-δ SOFC Thin-Film Cathodes in Dry, Humid and CO2-Containing Atmospheres.* Journal of The Electrochemical Society, 2013. **160**(11): p. F1197-F1206.

198. Tietz, F., et al., *Degradation phenomena in a solid oxide electrolysis cell after 9000 h of operation.* Journal of Power Sources, 2013. **223**: p. 129-135.

199. Ivers-Tiffée, E., A. Weber, and D. Herbstritt, *Materials and technologies for SOFC-components.* Journal of the European Ceramic Society, 2001. **21**(10): p. 1805-1811.

200. Mogensen, M.B., et al. *Relation Between Ni Particle Shape Change and Ni Migration in Ni?YSZ Electrodes ? a Hypothesis Fuel Cells Volume 17, Issue 4.* Fuel Cells, 2017. **17**, 434-441.

Band / Volume 429
**Characterization of spatial-temporal varying riverbed hydraulic
conductivity and its role on the estimation of river-aquifer
exchange fluxes with data assimilation**
Q. Tang (2018), xv, 117 pp
ISBN: 978-3-95806-339-6

Band / Volume 430
**Der Einfluss von Wasserdampf auf den Sauerstofftransport
in keramischen Hochtemperaturmembranen**
F. Thaler (2018), ii, 93, XXXI pp
ISBN: 978-3-95806-340-2

Band / Volume 431
**Analysis & modeling of metastable photovoltaic technologies:
towards dynamic photovoltaic performance models**
M. Görig (2018), 246 pp
ISBN: 978-3-95806-342-6

Band / Volume 432
Laser Treatment of Silicon Thin-Films for Photovoltaic Applications
C. Maurer (2018), vii, 165 pp
ISBN: 978-3-95806-347-1

Band / Volume 433
Mentalitäten und Verhaltensmuster im Kontext der Energiewende in NRW
K. Schürmann & D. Schumann (Hrsg.) (2018), 236 pp
ISBN: 978-3-95806-349-5

Band / Volume 434
**Adhäsionsverhalten von wässrigen Nafion-Lösungen an
dispersen Phasengrenzen**
A. Schulz (2018), xii, 129 pp
ISBN: 978-3-95806-354-9

Band / Volume 435
**Alterungs- und fehlertolerante optimale Betriebsführung
eines Direktmethanol-Brennstoffzellensystems**
R. Keller (2018), XX, 175 pp
ISBN: 978-3-95806-355-6

Band / Volume 436
**Chamber study of biogenic volatile organic compounds:
plant emission, oxidation products and their OH reactivity**
Y. Zhujun (2018), ix, 139 pp
ISBN: 978-3-95806-356-3

Schriften des Forschungszentrums Jülich
Reihe Energie & Umwelt / Energy & Environment

Weitere *Schriften des Verlags im Forschungszentrum Jülich* unter
http://wwwzb1.fz-juelich.de/verlagextern1/index.asp

JÜLICH
Forschungszentrum